

**SPIN ORBIT COUPLING INDUCED PHENOMENA
IN SPINTRONIC DEVICES**

by

Tao Wang

A dissertation submitted to the Faculty of the University of Delaware in partial fulfillment of the requirements for the degree of Doctor of Philosophy in Physics

Fall 2017

© 2017 Tao Wang
All Rights Reserved

**SPIN ORBIT COUPLING INDUCED PHENOMENA
IN SPINTRONIC DEVICES**

by

Tao Wang

Approved: _____
Edmund R. Nowak, Ph.D.
Chair of the Department of Physics and Astronomy

Approved: _____
George H. Watson, Ph.D.
Dean of the College of Arts and Sciences

Approved: _____
Ann L. Ardis, Ph.D.
Senior Vice Provost for Graduate and Professional Education

I certify that I have read this dissertation and that in my opinion it meets the academic and professional standard required by the University as a dissertation for the degree of Doctor of Philosophy.

Signed:

John Q. Xiao, Ph.D.
Professor in charge of dissertation

I certify that I have read this dissertation and that in my opinion it meets the academic and professional standard required by the University as a dissertation for the degree of Doctor of Philosophy.

Signed:

Yi Ji, Ph.D.
Member of dissertation committee

I certify that I have read this dissertation and that in my opinion it meets the academic and professional standard required by the University as a dissertation for the degree of Doctor of Philosophy.

Signed:

Matthew DeCamp, Ph.D.
Member of dissertation committee

I certify that I have read this dissertation and that in my opinion it meets the academic and professional standard required by the University as a dissertation for the degree of Doctor of Philosophy.

Signed:

Stephanie Law, Ph.D.
Member of dissertation committee

ACKNOWLEDGMENTS

First and foremost, I would like to thank my advisor, Prof. John Q. Xiao who gave me the opportunity to study in his group. His hands-off styles gives me a great degree of freedom and I really appreciate this free atmosphere he provides for our research. In the meantime, his rich knowledge, wisdom and diligence in the work show me how to be a good scientist.

I would like to specially thank Prof. Xin Fan, for his patient help and selfless effort in guiding me through almost every step in my research since I joined the group in 2012. I would also like to thank Prof. Yi Ji, Prof. Matthew DeCamp and Prof. Stephanie Law for their kind help.

My sincere gratitude also goes to all my colleagues and friends for their help and support in these years: Dr. Qi Lu, Dr. Yang Zhou, Dr. Yunpeng Chen, Dr. Jun Wu, Dr. Shuhan Chen, Dr. Yunsong Xie, Dr. Chuan Qin, Muhammad Asif Warsi, Halise Celik, Harsha Kannan, Rasoul Barri, Yunjiao Cai, Theresa Ginley, Yong Wang, Hang Chen, Dainan Zhang, Yang Wang and Xingyu Shen.

I would like to thank my parents for their encouragement and support throughout all the time.

TABLE OF CONTENTS

LIST OF TABLES	ix
LIST OF FIGURES	x
ABSTRACT	xviii

Chapter

1	INTRODUCTION	1
1.1	Giant Magnetoresistance	1
1.2	Spin Transfer Torque.....	3
1.3	Spin Orbit Torque.....	4
1.3.1	Spin Hall Effect	6
1.3.2	Rashba-Edelstein Effect	7
1.3.3	Topological Surface State.....	7
1.4	Alternative Magnetic Switching Technique	8
1.5	Thesis Layout	11
	REFERENCES	12
2	FABRICATION OF SPINTORNIC DEVICES WITH SHADOW MASK TECHNIQUE	17
2.1	Introduction	17
2.2	Shadow Mask Technique	18
2.2.1	General Procedure	18
2.2.2	Shadow Mask Fabrication	19
2.2.2.1	PMMA-based Shadow Mask.....	19
2.2.2.2	CSAR-based Shadow Mask	21
2.2.3	Electron Beam Evaporation.....	24
2.3	Nano Devices Fabrication	26

2.3.1	Hall Bar Structure.....	27
2.3.1.1	Hall Bar Shadow Mask.....	28
2.3.1.2	Deposition.....	30
2.3.1.3	Characterization of Nanodevices.....	35
2.3.2	Nanofabrication of MTJ Devices	36
2.3.2.1	MTJ Shadow Mask.....	36
2.3.2.2	Deposition Process	39
2.3.2.3	Characterization of MTJ Nanodevices	41
2.3.3	Magnetoelectric Devices	42
2.3.3.1	ME device characterization	42
2.3.3.2	Nanofabrication of ME Devices	44
2.3.3.3	Characterization of ME Devices	46
	REFERENCES	48
3	SPIN HALL EFFECT IN 3D LIGHT TRANSITION METALS	49
3.1	Introduction	49
3.2	Large Spin Hall Angle in Vanadium Film	50
3.2.1	Sample Fabrication and Characterization.....	50
3.2.2	High Frequency Measurements	54
3.2.2.1	FMR Measurement.....	55
3.2.2.2	Determination of Spin Diffusion Length.....	58
3.2.3	Spin Orbit Torques in V/CoFeB system.....	59
3.2.3.1	Spin Orbit Torque Measurement with Polar MOKE....	60
3.2.3.2	Determination of Damping-Like Torque.....	63
3.2.3.3	Spin Mixing Conductance Analysis	68
3.2.4	Conclusions	70
	REFERENCES	71
4	SPIN ORBIT EFFECT IN TOPOLOGICAL INSULATOR- FERROMAGNET HETEROSTRUCTURE	74
4.1	Background and Motivation	74

4.2	Methods of Spin Orbit Torques Measurement	75
4.2.1	Second Harmonic Hall Voltage Measurement	75
4.2.2	All Optical Spin Torque Measurement.....	80
4.2.3	Comparison between MOKE and Electrical Spin Torque Measurements.....	83
4.3	Spin Orbit Torque in TI/FM Bilayer	85
4.3.1	Giant Spin Orbit Torque Efficiency in $\text{Bi}_2\text{Se}_3/\text{Ni}_{80}\text{Fe}_{20}$ Bilayer .	85
4.3.2	Topological Surface State Induced Spin Orbit Torques.....	91
	REFERENCES	100
5	SPIN ORBIT EFFECT WITH SPIN ROTATION IN FERROMAGNETIC MATERIALS	102
5.1	Introduction	102
5.1.1	Motivation	102
5.1.2	Our Hypothesis to Control Spin Polarization Direction.....	104
5.1.3	Magnetization Anti-damping Switching	106
5.1.4	Mirror Symmetry Based Analysis	107
5.2	Experiment	109
5.2.1	Sample Preparation.....	109
5.2.2	Electrical and Magnetic Properties.....	110
5.2.3	Spin Orbit Torque Measurement.....	111
5.2.3.1	Damping-Like Torque Measurement	113
5.2.3.2	Field-Like Torque Measurement.....	117
5.2.4	Spin Galvanic Effect Measurement.....	119
5.3	Discussion.....	121
5.3.1	Current in Plane Spin Transfer Torque	121
5.3.2	Non-local Spin Rotation Process.....	121
5.3.3	Anomalous Hall Effect induced Spin Rotation Symmetry.....	123
5.3.4	Magnetization Tilted by Magnetostatic Coupling.....	124
5.3.5	Other Potential Mechanisms.....	124
5.4	Conclusion.....	124

REFERENCES	126
6 CONCLUSION AND FUTURE DIRECTION	128
Appendix	
A REPRINT PERMISSIONS	132

LIST OF TABLES

Table 2.1	The magnetron sputtering recipe for the PMA [Co/Pd] _n multilayers.....	32
Table 2.2	The recipes to fabricate Pd(0.5nm)/[Co(0.3nm)/Pt(0.9nm)] ₆ /Co(0.3nm)/AlO _x /NiFe(2.0nm)/Ta (2.0nm) and Ta(5.0nm)/CoFeB(0.8nm)/MgO(2.0nm)/CoFeB(1.0nm)/Ta(5.0nm) MTJs via shadow mask technology.....	41
Table 3.1	The magnetron sputtering parameters of the V(30 nm)/CoFeB(2 nm) samples. (RT represents “room temperature”)	53

LIST OF FIGURES

Figure 1.1	The bit-cell architecture of (a) 2-terminal STT-MRAM and (b) 3-terminal SOT-MRAM.	5
Figure 1.2	A typical test sample of magnetoelectric device. $[\text{Co/Pd}]_n$ multilayer PMA Hall bar structure has been prepared through shadow mask on top of the (0001) surface of magnetoelectric Cr_2O_3	9
Figure 1.3	The spin structure of the (0001) surface of a single crystalline Cr_2O_3 , with two 180° antiferromagnetic magnetic order (red and blue arrows). (Reprinted by permission adapted from Ref. [68], copyright (2010)).....	10
Figure 1.4	The details of switching in a perpendicular anisotropic heterostructure Cr_2O_3 (0001)/Pd(0.5 nm)/(Co(0.6 nm)/Pd(1.0 nm)) ₃ . The hysteresis loop of magnetoelectric annealed CoPd thin film with (a) positive and (a') negative exchange bias, respectively. (b) The applied electric field dependent hysteretic behavior. The diagrams illustration of Cr_2O_3 boundary magnetism/spin structure in the (c) positive and (c') negative exchange bias states. (Reprinted with permission adapted from Ref. [69], copyright (2013))	11
Figure 2.1	The prototype of ME device with antiferromagnet Cr_2O_3 and MgO-based MTJ. The surface magnetism at $[\text{Co/Pd}]_n/\text{Cr}_2\text{O}_3$ interface could be switched by voltage-controlled exchange coupling. The CoFeB free layer in MgO-MTJ could also be switched when $[\text{Co/Pd}]_n$ film is changing its magnetization.	17
Figure 2.2	The schematic illusion of the shadow mask evaporation general procedure. (a) Substrate cleaning; (b) Spin coating of bilayer E-beam resists; (c) E-beam writing process; (d) Bridge layer development; (e) Support layer development; (f) E-beam evaporation at angle 1; (g) E-beam evaporation at angle 2; (h) Shadow mask lift-off process.	19
Figure 2.3	The SEM image of PMMA/PMGI shadow mask.	20

Figure 2.4	The RIE test on CSAR positive tone E-beam resist. The CSAR has shown high plasma etching resistance, which makes CSAR a good alternative candidate of PMMA as the bridge layer in bilayer shadow mask.....	22
Figure 2.5	(a) The optical image of CSAR/LOR3A shadow mask with $1\mu\text{m}$ undercut. (b) The relation between development duration and undercut opening size of LOR 3A resist in the developer AR 300-47.....	23
Figure 2.6	The SEM image of the nano MTJ device that was fabricated using shadow mask technique. The rectangle solid box indicates the profile of the shadow mask aperture. After both E-beam evaporation and magnetron sputtering deposition, due to different directionality of the two deposition methods, the film on the substrate through E-beam evaporation is confined in the rectangle solid box. By contrast, the film deposited with magnetron sputtering through the same shadow mask is expanded into the red dash elliptical shape.....	25
Figure 2.7	The flow chart of nanofabrication procedure based on shadow mask technique.	27
Figure 2.8	The microscopy images of typical (a) contact pads ($180\mu\text{m} \times 180\mu\text{m}$) on Si/SiO ₂ wafer and (b) E-beam alignment markers ($10\mu\text{m} \times 10\mu\text{m}$) on Cr ₂ O ₃ sample.	28
Figure 2.9	The Hall bar shadow mask design. (a) The purple area represents the contact pads, and (b) the red area is the shadow mask aperture (opening) defined by E-beam writer.	29
Figure 2.10	The development process of the PMMA/PMGI shadow mask. (a) PMMA layer development in MIBK for 90s and in IPA for 30s. (b) PMGI layer development in XP101A for 5min 30s.....	30
Figure 2.11	The AFM scanning image of the Co ₄₀ Fe ₄₀ B ₂₀ nanowire.	31
Figure 2.12	The schematic illustration of the deposition process of Hall bar structure with shadow mask. (a) Pd(0.5nm)/[Co(0.3nm)/Pd(0.9nm)] ₆ multilayer film with PMA was deposited at 0° incident angle to form Hall bar structure. (b) Au electrode connecting to one of the contact pad was deposited with E-beam evaporation at an incident angle of $\theta = 60^\circ$. (c) Reverse the E-beam incident angle to $\theta = -60^\circ$ connects the other contact pad.	33

Figure 2.13	The SEM images of E-beam angle deposition issue. (a) Two steps of angle deposition will cause the connection issue which is due to the shadow effect in the E-beam evaporation process. (b) The zoom in image of the disconnection happened on one Hall electrode.	34
Figure 2.14	The E-beam evaporation test for Al, Cu, and Ag electrode materials. (a) Al electrode will cause the static charging issue. (b) E-beam evaporated Cu electrode has adhesion issue. (c) Ag electrode needs extra buffer layer such as Cr or Ta, otherwise Ag is unable to form a uniform film.	35
Figure 2.15	(a) The SEM image of [Co/Pd] _n Hall bar structure and (b) the Hall voltage as a function of out-of-plane external field for three individual Hall bar devices with different nanowire width.	36
Figure 2.16	The shadow mask design for MTJ nanodevice fabrication. (a) The purple areas represent the contact pads and the red areas are the nanoscale structure defined by E-beam writer. (b) The HR-SEM image of a typical shadow mask of MTJ devices.....	37
Figure 2.17	The HR-SEM image of a typical AlOx tunnel junction.....	38
Figure 2.18	The comparison between shadow mask (a) PMMA/PMGI and (b) CSAR 09/LOR 5A after MgO sputtering. CSAR E-beam resist is able to survive under UV irradiation and heating environment.....	39
Figure 2.19	The schematic illustration of MTJ device deposition process through shadow mask. (a) E-beam angle evaporation for the bottom electrode; (b) MTJ full stack magnetron sputtering with perpendicular deposition; (c) E-beam angle evaporation of AlOx as the side wall protection; (d) E-beam angle evaporation for top electrodes.	40
Figure 2.20	(a) The I-V curve for AlOx-based MTJs. (b) The magnetoresistance as a function of the perpendicular magnetic field.....	42
Figure 2.21	The electrical characterization of epitaxial Cr ₂ O ₃ film. The resistivity measurement has been performed between Pd bottom electrode and patterned Cr/Au top electrodes with various contact sizes, which is shown in the inset.	43
Figure 2.22	The current-voltage characteristics obtained from electrical measurements. (a) The images of contacts on top of Cr ₂ O ₃ thin film. The current-voltage characteristics on both (b) Ta/Au contacts and (c) HfO ₂ / Ta/Au contacts.	44

Figure 2.23	E-beam alignment marks design. (a) Two sets of markers with different functionalities have been included in the shadow mask design (①: Sample bottom location markers; ②: Corner alignment markers). (b) The location markers. (c) The alignment markers at corners.	45
Figure 2.24	The AHE of [Co/Pd] _n film on top of (a) Cr ₂ O ₃ thin film, (b) Si wafer and (c) isothermal switching test result at a 3000 Oe external magnetic field.....	47
Figure 3.1	Samples characterizations of V(<i>x</i> nm)/CoFeB(2 nm). (a) X-ray diffraction pattern of samples V(30 nm)/CoFeB(2 nm) grown at room temperature (black) and 400°C (red). (b) The total resistivity of test samples (red) and control sample (blue) as a function of V thickness. (c) and (d) HR-TEM images of V(30 nm)/CoFeB(2 nm) test and control samples. The insets are the corresponding electron diffraction patterns.	51
Figure 3.2	Fast Fourier transformation analysis of vanadium’s TEM images. (a) The test sample, which has been prepared at room temperature, shows both <i>bct</i> (red) and <i>bcc</i> (white) phases. (b) The control sample FFT image is dominated by <i>bcc</i> phase.	52
Figure 3.3	The XRD spectrums of V films with different sputtering conditions of samples (a) to (b).....	54
Figure 3.4	The schematic illustration of FMR measurement based on CPW configuration.	55
Figure 3.5	A typical FMR spectrum which is fitted based on Equation 3.5.....	57
Figure 3.6	The FMR fitting results of V/CoFeB samples. (a) the effective demagnetization field $\mu_0 M_{\text{eff}}$, (b) the Gilbert damping factor α , and the inhomogeneous broadening ΔH_0	59
Figure 3.7	Three configurations in MOKE measurements: (a) polar, (b) transverse, (c) longitudinal.	60
Figure 3.8	The schematic illustration of current induced SOTs in NM/FM bilayer with in-plane magnetization.	61
Figure 3.9	The schematic illustration of polar MOKE spin torque magnetometer setup (BS, beamsplitter; HWP, half-wave plate; OBJ, objective; PBS, polarizing beamsplitter).....	62

Figure 3.10	A typical polar MOKE measurement magnetic field scan result of V(5 nm)/CoFeB(2 nm) sample.	63
Figure 3.11	(a) The typical SOT result of V/CoFeB and (b) the effective Oersted field induced by the current.	64
Figure 3.12	Conductivity of the entire V(x nm)/CoFeB(2 nm) stack as the function of V thickness.	66
Figure 3.13	The spin Hall angle of V/CoFeB test samples (prepared at room temperature) and control sample (prepared at 400°C).....	67
Figure 4.1	The schematic illustration of second harmonic Hall voltage measurement of the current induced SOTs.	76
Figure 4.2	Typical second harmonic Hall voltage measurement results of (a) the first order signal V_{ω} and (b) the second order signal $V_{2\omega}$	78
Figure 4.3	The second order PHE field like torque measurement. (a) The experimental setup which includes an external Helmholtz coil generating a calibration field. (b) The Hall voltage measurement results with different calibration fields. (c) The linear regression analysis based on the test result and calibration result. (d) The linear response indicates the measurement is in the linear response regime.(Reprinted by permission adapted from [9], copyright (2014)) ..	79
Figure 4.4	The illustration of (a) MOKE circular dichroism (first order) and (b) linear dichroism (second order) response.....	81
Figure 4.5	The normal incident MOKE measurement results of Pt/Py bilayer. (a) The polar and quadratic component response coefficients as function of the polarization of linear incident light; (b) The Kerr rotation signals with different linear polarization direction.....	82
Figure 4.6	The quadratic MOKE field like torque measurement of Pt/Py bilayer structure. (a) The Kerr rotation response induced by spin orbit torques (black) and external calibration field (red) in FM layer, respectively.....	83
Figure 4.7	The damping-like and field-like torques spin Hall angle θ_{\parallel} and θ_{\perp} based on various spin torque measurement techniques.	84
Figure 4.8	The effective (a) in-plane and (b) out-of-plane spin Hall angle in $\text{Bi}_2\text{Se}_3(8 \text{ nm})/\text{Py}(x \text{ nm})$ ($x = 8, 12, 16 \text{ nm}$) bilayers.	85

Figure 4.9	The temperature dependent sheet resistance of 20 nm Bi_2Se_3 film.....	86
Figure 4.10	The temperature dependence of (a) sheet resistance, (b) carrier density and (c) mobility of 10 nm Bi_2Se_3	87
Figure 4.11	(a) Typical Hall bar device for the second harmonic Hall voltage measurement. This six terminals device is also used in electrical resistivity measurement. (b) The illustration of second harmonic Hall measurement configuration.	88
Figure 4.12	The second order Hall voltage $V_{2\omega}$ as a function of in-plane magnetic field at different temperatures for $\text{Bi}_2\text{Se}_3(10 \text{ nm})/\text{Py}(4 \text{ nm})$ bilayers.....	89
Figure 4.13	The second order Hall voltage $V_{2\omega}$ as a function of nearly out-of-plane magnetic field ($\theta_H \approx 5^\circ$) at different temperatures for $\text{Bi}_2\text{Se}_3(10 \text{ nm})/\text{Py}(4 \text{ nm})$ bilayers.....	90
Figure 4.14	(a) The field-like torque efficiency and (b) damping-like torque efficiency as a function the temperature for $\text{Bi}_2\text{Se}_3(10 \text{ nm})/\text{Py}(4 \text{ nm})$ bilayers.	91
Figure 4.15	The second order Hall voltage as a function of in-plane magnetic field at different temperatures for $\text{Bi}_2\text{Se}_3(20 \text{ nm})/\text{Co}(3 \text{ nm})$ bilayer.	92
Figure 4.16	The first order Hall voltage as a function of (a) in-plane and (b) out-of-plane magnetic fields for $\text{Bi}_2\text{Se}_3(20 \text{ nm})/\text{Co}(3 \text{ nm})$ bilayer.....	93
Figure 4.17	The ΔR_{PHE} and ΔR_{AHE} extracted from temperature dependent first order Hall voltage.....	94
Figure 4.18	The second order Hall voltage fitting results under different temperatures. The fitting region is chosen at the range of 0.2 T to 0.5 T, in order to satisfy the small angle approximation in the fitting process that is based on Equation 4.13.....	95
Figure 4.19	The summary of temperature dependent SOTs measurement in 20 nm $\text{Bi}_2\text{Se}_3/3 \text{ nm Co}$ heterostrucutre. (a) The field like torque efficiency and (b) damping like torque efficiency.	96
Figure 4.20	The temperature dependent of the second harmonic measurement of $\text{Bi}_2\text{Se}_3(10 \text{ nm})/\text{Co}(5 \text{ nm})$ samples.	97
Figure 4.21	The current dependent measurements of h_{DL} and h_{FL} at room temperature	98

Figure 4.22	The polar MOKE SOT measurement of Bi ₂ Se ₃ (20 nm)/Co(5 nm) sample at room temperature. (a) The damping like torque spatial line scan and (b) the out-of-plane current induced Oersted field distribution across the sample's transverse direction.	99
Figure 5.1	The schematic illustration of the SOTs assisted magnetization switching in FM/NM bilayer structure.	103
Figure 5.2	The illustration of spin orbit effects with (a) conventional and (b) rotation symmetry. Spin current generated from a charge current near the FM/NM interface. The red and blue arrows represent spins. The vertical blue wide arrows represent the spin current with conventional symmetry and spin rotation symmetry, respectively.	105
Figure 5.3	The schematics of mirror symmetry and SOEs induced spin polarizations. (a) The spin polarization induced by the conventional SHE in bulk NM layer or near the NM surface. The gray arrow indicates the charge current which is along x direction. The light green wide arrow represents the spin current flow direction, here we focus on the spin current flow on the top surface. The out-of-plane spin polarization couldn't exist in the NM, since it is unable to be uniquely determined by the charge current. (b) The spin rotation symmetry induced out-of-plane spin polarization could satisfy the relation described by Equation 5.2.	109
Figure 5.4	Magnetic hysteresis loops measured by VSM. (a) Hysteresis loops measured for the test sample and control sample in the out of plane direction and (b) the in-plane direction.	111
Figure 5.5	The experimental configuration for the SOTs measurement by MOKE magnetometry.....	112
Figure 5.6	The polar MOKE response Ψ_{polar} measured in the test and control samples when current is applied parallel with H_{ex} ($\phi = 0^\circ$). No dependence of \mathbf{m}_{PML} is observed.	114
Figure 5.7	The polar MOKE response measured in the test and control samples when current is applied perpendicular to H_{ex} ($\phi = 90^\circ$). In the test sample, the polar MOKE response is reversed when \mathbf{m}_{PML} is reserved. In the control sample, the polar MOKE response has little dependence on \mathbf{m}_{PML}	116
Figure 5.8	The angle dependence of $\Delta\Psi_{\text{polar}}^{\text{even}}$ and $\Delta\Psi_{\text{polar}}^{\text{odd}}$ of the test sample. .	116

Figure 5.9	The current induced field like torque. Here we use quadratic MOKE magnetometry to measure current induced in-plane effective fields in the same configuration polar MOKE measurement. (a) The quadratic MOKE response measured in the test and control samples when current is applied parallel to H_{ex} . No dependence on \mathbf{m}_{PML} is observed. (b) The quadratic MOKE response measured in the test and control samples when current is applied perpendicular to H_{ex} . In the test sample, the quadratic MOKE response is reversed when \mathbf{m}_{PML} is reversed. In the control sample, the weak quadratic MOKE response is observed, which is likely due to a small misalignment. (c) The angle dependence of Ψ_{quad}^{even} and Ψ_{quad}^{odd} of the test sample.....	118
Figure 5.10	The experimental configuration of spin Seebeck effect driven spin galvanic effect measurement.	120
Figure 5.11	The spin Seebeck driven spin galvanic effect measurements. (a) Voltages measured in the two different configurations for the test sample and control sample. (b) Angle dependence of the voltage signals associated with Py switching.....	121
Figure 5.12	The alternative mechanisms for a spin current with rotated polarization. (a) The yellow arrow with the red color spin polarization represents the spin rotation mechanism in this study. The blue “U-turn” arrow with red spin polarization indicates the alternative mechanism that origins from the Pt/Py interface, which could also leads to the sample spin polarization. (b) The polar MOKE measurement of the damping like torque in the sample of PML/Cu(3 nm)/Py(2 nm)/Ta(3 nm). (c) The Py thickness dependent of the damping like torque measurement. (d) The ratio between h_{DL} and h_{DL}^R as a function of Py thickness.	123

ABSTRACT

Spin-orbit coupling (SOC) is a relativistic interaction between spin and orbital momentum that induces a plenty of novel phenomena including spin Hall effect (SHE), Rashba-Edelstein effect (REE), topological surface states (TSS), spin orbit torques (SOTs), etc. In this thesis work, we have conducted relevant researches in order to develop materials and heterostructures, as well as new phenomena that can lead to high efficiency in generating SOTs or switching the magnetization. We have also investigated fabrication technique that speeds up the fabrication of nanoscale devices.

A nanofabrication procedure has been developed based on shadow mask and angle deposition techniques. It is an efficient bottom-up, as oppose to top-down lithography technique, to fabricate rather complicate devices. A comprehensive study of shadow mask technique has been accomplished to fabricate magnetoelectric (ME) device based on voltage controlled boundary magnetism of antiferromagnet Cr_2O_3 and magnetic tunnel junctions.

The researches on SOTs focus on SHE, REE and TSS in which a charge current is converted into spin current that exerts the SOTs on the magnetization of neighboring ferromagnetic layer. First, we have studied the charge to spin conversion efficiency in $3d$ light transition metal vanadium in V/CoFeB bilayer, which shows a surprisingly large spin Hall angle that is comparable to that of Pt. Second, we have investigated the temperature dependent SOTs in $\text{Bi}_2\text{Se}_3/\text{Co}$ and $\text{Bi}_2\text{Se}_3/\text{Ni}_{80}\text{Fe}_{20}$ bilayers, and confirmed the existence of TSS in $\text{Bi}_2\text{Se}_3/\text{Co}$ systems. Finally, we have discovered a novel spin rotation behaviors in a ferromagnetic metal, where the spin

polarization is rotated around the magnetization. It implies that a perpendicularly polarized spin current can be generated by an in-plane charge current through a ferromagnetic metal, which can be applied to realize the anti-damping switching process in magnetic heterostructures.

Chapter 1

INTRODUCTION

1.1 Giant Magnetoresistance

The development of spintronics has been triggered by the discovery of giant magnetoresistance (GMR) in 1988 [1-2]. Since then the spin degree of freedom is becoming an important tool to manipulate charges with spins, and vice versa. Compared with conventional electronic devices, spintronics devices could have lower power consumption, faster response speed, as well as non-volatility properties. Therefore, the spintronics application in solid state memories becomes one of the most important field of research.

GMR effect happens in electron transport process in a sandwich structure composed of ferromagnetic (FM)/non-magnetic (NM)/ferromagnetic (FM) thin film stacks [3], which is also known as spin valve structure. Due to the presence of “majority band” (or spin-up band) and “minority band” (or spin-down band) in electronic band structures of FM, the spin-up and spin-down electrons have different conduction or scattering rates [4-5]. When conduction electrons have the same spin direction with the magnetization orientation in FMs, they will experience less scattering. Thus, when two FM layers in a spin valve have the parallel magnetization orientation, the spin-up electrons are able to transport through both FM electrodes with lower resistance. For the anti-parallel configuration, either spin-up or spin-down electrons have high scattering rate going through two FM layers, the spin valve

exhibits a higher resistance. The discovery of GMR has significantly impacted on applications, leading to unprecedented storage density in computer hard drives [6-8].

Another important finding in spintronics is the tunneling magnetoresistance (TMR) of magnetic tunnel junctions (MTJs). The metallic NM spacer in spin valve is replaced with amorphous tunnel barrier (AlO_x) [9-10] and later with crystalline barrier (MgO) [11-12]. Similar to spin valves, the resistance of MTJ is different from parallel and anti-parallel magnetic configurations of two FM layers. The value of TMR is usually higher than GMR. Especially, for MgO-based MTJs, TMR can be more than 200% [13]. MTJs with high TMR are promising candidates for making magnetic random access memory (MRAM), which is fast, nonvolatile and potential for high density [8].

MRAM stores information in nanometer magnet. For MTJ-based MRAM, the binary information, 1 and 0, is encoded with parallel and anti-parallel magnetization between two magnetic electrodes, respectively. The information can be read out through the resistance measurement. Comparing with the reading process, it is much more challenging to write the information which requires the magnetization switching in one of the FM electrodes. The early designs of MRAM use current generated Oersted field to switch memory cell bits, which causes several problems. First, it is difficult to switch a bit locally without affecting the neighboring bits since it is difficult to shield the magnetic field. Second, it consumes too much energy to generate a sufficient field to switch a FM layer [14].

To solve these problems, researchers are searching for new magnetization switching technologies for the next generation of MRAM. One potential solution is to use spin transfer torque (STT) phenomena.

1.2 Spin Transfer Torque

In 1996, Slonczewski [15] and Berger [16] independently predicted the existence of STT, which was later named as Slonczewski torque. When a charge current which has equal number of spin-up and spin-down electrons, i.e. $N_{\uparrow} = N_{\downarrow}$, goes through the first FM layer, the difference in scattering rates for spin-up and spin-down electrons polarizes the charge current, resulting in an outgoing spin polarized current ($N_{\uparrow} \neq N_{\downarrow}$). When this spin polarized current with non-zero net spin angular momentum enters the second FM layer, the spins with their direction transverse to the magnetization direction of the second FM layer are absorbed. Because of the conservation of the angular momentum, the magnetization direction of the second FM layer is altered, i.e. the absorption of the transverse spin angular momentum creates a torque on the magnetization or the spin angular momentum of incoming spin polarized current is “transferred” to the magnetization. This current induced torque is called STT, which is predicted to be strong enough to switch the magnetization for a sufficient current.

The first nanoscale magnet switching has been realized in Co/Cu/Co metallic spin valve structure [17-18], and later in 2004, this switching phenomenon was also demonstrated in nanoscale AlO_x-based MTJs [19-20]. From the perspective of practical applications, MgO-based MTJs have much higher spin polarization than MTJs with an amorphous tunnel barrier, which are capable to generate spin current with higher spin-polarization, leading to higher switching efficiency. Meanwhile, the much larger TMR also gives rise to much stronger signal for reading out the information. The STT-assisted switching has then been demonstrated in MgO-based junctions [21-22]. Thereafter, much effort has been devoted to the development of

spin transfer torque magnetic random access memory (STT-MRAM) device based on MgO-MTJs.

STT presents an efficient means to switch the magnetization. The critical current density to switch a perpendicular magnetization is proportional to the energy barrier $E_b = M_s H_K V/2$ [23], where M_s is the saturation magnetization, H_K is the effective anisotropy, and V is the volume of the free FM layer. For samples with in-plane magnetization, the critical switching current density is much higher and is proportional to $M_s H_K V/2 + M_s^2 V/2$ [24]. Therefore, nanoscale magnets with perpendicular magnetic anisotropy (PMA) are preferred in applications [25]. The demonstrations of STT-MRAM devices integrated with CMOS processing have been reported. In 2005, a 4 Kbit STT-MRAM based on CoFeB/MgO/CoFeB junctions was first reported [26]. Subsequently, 2 Mbit [27], 32 Mbit [28] and 64 Mbit [29] STT-MRAM were demonstrated.

The critical current density is as high as of the order of 10^{11} A/m². As shown in Figure 1.1 (a), STT-MRAM is a two-terminal device so the “write” and “read” currents go vertically through the sample stack. The high “write” current density will degrade the structural integrity of MTJs. In addition, STT-MRAM always has heating and resistive losses issues [14, 25]. Attempt to solve these issues led the discovery of spin-orbit torque (SOT) discussed below.

1.3 Spin Orbit Torque

Current-driven SOT arises from the spin-orbit coupling (SOC) [30-33]. If a NM has strong SOC, an in-plane charge current going through the NM will create a transverse pure spin current in which electrons with opposite spin polarizations move in opposite direction. The spin current enters an adjacent FM layer in NM/FM bilayer

films and exerts the spin torques on the magnetization in FM layer. This phenomenon is called as SOT.

The discovery of SOT leads to a new type of memory device, a three terminal SOT-MRAM [14], which is shown in Figure 1.1 (b). In STT-MRAM devices, the write and read lines share the same path, and a large “write” current goes through the MTJ (Figure 1.1 (a)). In SOT-MRAM devices, the large “write” current flows through the NM film plane, while the much smaller “read” current goes through the MTJ cell.

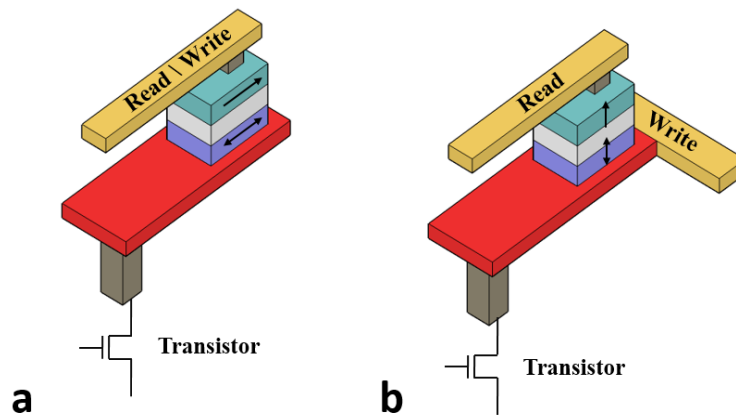


Figure 1.1 The bit-cell architecture of (a) 2-terminal STT-MRAM and (b) 3-terminal SOT-MRAM.

In addition to switch a magnetization, SOT can also be used to efficiently move magnetic domains much faster than those moved by STT [34-36], to drive magnetic auto-oscillations [37] even in devices with an extended size [38]. In this thesis, we will mainly focus on the understanding of SOT in magnetization switching.

1.3.1 Spin Hall Effect

The spin Hall effect (SHE) is deeply related to SOT phenomena. The SHE was firstly discussed by Dyakonov and Perel [39-40] in 1971, and reinvigorated by Hirsh in 1999 [41]. The SHE could be mathematically described as $\mathbf{Q}_\sigma = (\hbar/2e)\theta_{\text{SH}}\mathbf{j}_c \times \boldsymbol{\sigma}$, where \hbar is the reduced Planck's constant, e is the electron charge, \mathbf{Q}_σ is the spin current density, \mathbf{j}_c is the charge current density, and θ_{SH} represents the efficiency of the charge to spin conversion which is also defined as spin Hall angle. In NM/FM structures, the spin current is generated in directions transverse to the in-plane charge current due to the SHE in the bulk of the NM [42-43]. The SOT applies on the magnetization of FM due to this spin current could be expressed by the Landau-Lifshitz-Gilbert-Slonczewski equation

$$\frac{d\mathbf{m}}{dt} = -\mu_0\gamma\mathbf{m} \times \mathbf{H}_{\text{eff}} + \alpha\mathbf{m} \times \frac{d\mathbf{m}}{dt} + \tau_{DL}\mathbf{m} \times (\boldsymbol{\sigma} \times \mathbf{m}) + \tau_{FL}(\boldsymbol{\sigma} \times \mathbf{m}) \quad (1.1)$$

The third term on the right hand side has a similar form as the damping term in the equation, and it's often referred to as the damping-like (DL) torque τ_{DL}

$$\tau_{DL} = \frac{\xi_{DL}|\mathbf{Q}_\sigma|}{\mu_0 M_s d_{FM}} \quad (1.2)$$

where $\mu_0 M_s$ is the saturation magnetization of the FM, d_{FM} is the thickness of the FM, ξ_{DL} is an interface-dependent coefficient that describes the efficiency of the SOT. In addition, the spin current could also result in a field-like (FL) torque τ_{FL}

$$\tau_{FL} = \frac{\xi_{FL}|\mathbf{Q}_\sigma|}{\mu_0 M_s d_{FM}} \quad (1.3)$$

where ξ_{FL} is the efficiency for the FL torque. There is a debate about the existence of the FL torque induced by the bulk SHE, since there is an argument that the FL torque arises from the rotation of spins, which is significantly suppressed by dephasing process. However, in recent SOT measurements, the nonlocal FL torque have been observed in Py/Cu/Pt [44-45], CoFeB/Cu/Pt [46], as well as CoFeB/Hf/W [47].

1.3.2 Rashba-Edelstein Effect

Another source for SOT is from the Rashba-Edelstein effect (REE) that was discussed in two-dimensional electron gas (2DEG) [48-50]. Due to the structural inversion symmetry breaking at the interface, an in-plane charge current at the interface experiences an effective magnetic field parallel to the interface and perpendicular to the charge current. This leads to spin accumulation at the interface. Because of the exchange coupling between the spin accumulation and the magnetization of FM, an effective FL torque could also be generated as

$$\mathbf{T}_{FL} = \eta_{FL}(\boldsymbol{\sigma} \times \mathbf{m}) \quad (1.4)$$

where η_{FL} represents the strength of the REE induced FL torque. The spin accumulation will also process around the magnetization [51-52], which generates an effective DL torque described as

$$\mathbf{T}_{DL} = \eta_{DL}\mathbf{m} \times (\boldsymbol{\sigma} \times \mathbf{m}) \quad (1.5)$$

The REE has been theoretically shown to be proportional to the interface SOC and the Dzyaloshinskii-Moriya interaction (DMI) [53-54]. These two types of torques, arising from the interface, have the same form as the torques from bulk SHE contribution. An important question is how to quantitatively separate the contributions from interface REE and bulk SHE.

1.3.3 Topological Surface State

Besides the understanding of the mechanism for SOT, it is equally important to search for new materials that give rise to the optimum SOT. The key is to find materials with large spin current or spin accumulation. One such class of materials are topological insulators (TIs) [55-57]. TIs belong to a class of newly discovered “Dirac Materials” (DMs) [58], where the low-energy excitations are described by relativistic

Dirac or Weyl equations. These materials are usually narrow (or zero) gap semiconductors where two (or more) bands are strongly coupled near a level-crossing and lead to massless carriers (Dirac fermions). The most celebrated example of a DM is Graphene [59]. Unlike Graphene, where intrinsic SOC is small due to the lightness of carbon atoms [60-61], strong SOC is the key ingredient in TIs [62]. In TIs, SOC opens an energy gap E_G in the bulk and generates conducting edge (in 2D) or surface (in 3D) electronic states [55-56], where these massless Dirac fermions have spin direction locked to their momentum. This spin-momentum locking prevents backscattering of carriers by NM disorders [55-56] that leads to a topologically protected state. The topological surface state (TSS) [63-65] with spin-momentum locking feature promises optimum SOTs.

1.4 Alternative Magnetic Switching Technique

The current induced spin torques accommodate site-specific switching of magnetization of nano cell bits by current alone without magnetic field. However, the critical current density is still high on the level of 10^{11} A/m². In order to further reduce the energy consumption, an alternative magnetic switching technique, which relies on electric-field or voltage bias, opens up a new avenue towards the exploring of ultra-low energy switching spintronics devices. It has been demonstrated the electric-field-assisted reversible switching in CoFeB/MgO/CoFeB MTJs that involves interface anisotropy [66]. Moreover, multiferroics is another materials-based approach to achieving electric-field control of magnetism based on magnetoelectric (ME) effect [67].

In our study, a new prototype of spintronic device has developed based on ME effect of antiferromagnet (AFM) Cr₂O₃. The prototype of a ME device is as shown in

Figure 1.2. According to the original design, the surface charge on single-crystalline Cr_2O_3 couples with the upper layer of FM $[\text{Co}/\text{Pd}]_n$ with PMA. Because the boundary magnetization of Cr_2O_3 can be altered by the voltage-controlled exchange coupling, the FM $[\text{Co}/\text{Pd}]_n$ layer can be switched. Therefore structure of $\text{Pd}/\text{Cr}_2\text{O}_3/[\text{Co}/\text{Pd}]_n/\text{MgO}/\text{CoFeB}/\text{Ta}$, which can be written with voltage, can be used as bit cell in MRAM or other logic devices. To first understand the switching behavior, we can measure AHE in $\text{Pd}/\text{Cr}_2\text{O}_3/[\text{Co}/\text{Pd}]_n$ samples, which are much easy to fabricate.

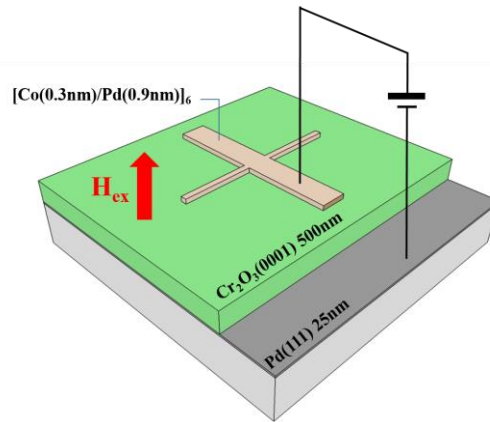


Figure 1.2 A typical test sample of magnetoelectric device. $[\text{Co}/\text{Pd}]_n$ multilayer PMA Hall bar structure has been prepared through shadow mask on top of the (0001) surface of magnetoelectric Cr_2O_3 .

Epitaxy Cr_2O_3 films grown by molecular beam epitaxy (MBE) have hexagonal closest packed (hcp) structure and (0001) orientation [68]. As shown in Figure 1.3, the (0001) surface has uncompensated net moments (red arrows) which stem from Cr^{3+} ions on the surface. Even with surface roughness, the net moments still remain [69].

Cr_2O_3 is an antiferromagnetic material with Neel temperature (T_{Neel}) of about 307K, The spin-up and spin-down sublattices as shown as red and blue arrows in Figure 1.3, respectively, which are aliened along the c -axis. This single domain state can be prepared by heating sample above T_{Neel} and cooling down with a voltage bias and in a magnetic field along the c -axis. This process is called ME annealing or training. After the initial ME annealing process under the combination of electric field \mathbf{E} and magnetic field \mathbf{H} , the net spin-polarization on the surface becomes maximum.

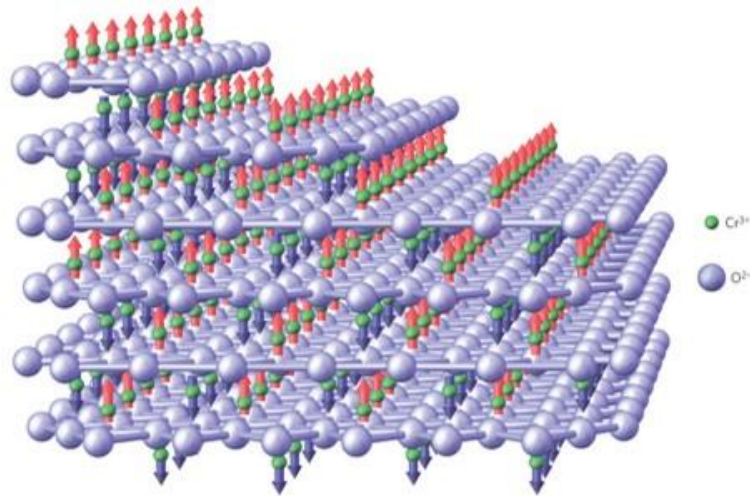


Figure 1.3 The spin structure of the (0001) surface of a single crystalline Cr_2O_3 , with two 180° antiferromagnetic magnetic order (red and blue arrows). (Reprinted by permission adapted from Ref. [68], copyright (2010))

This surface net magnetic moments can be isothermally switched via application of both electric and magnetic fields [69]. A complete hysteretic switching result is shown in Figure 1.4. The surface spins in Cr_2O_3 are exchange coupled with adjacent $[\text{Co}/\text{Pd}]_n$ film, which, in turn, can also be switched.

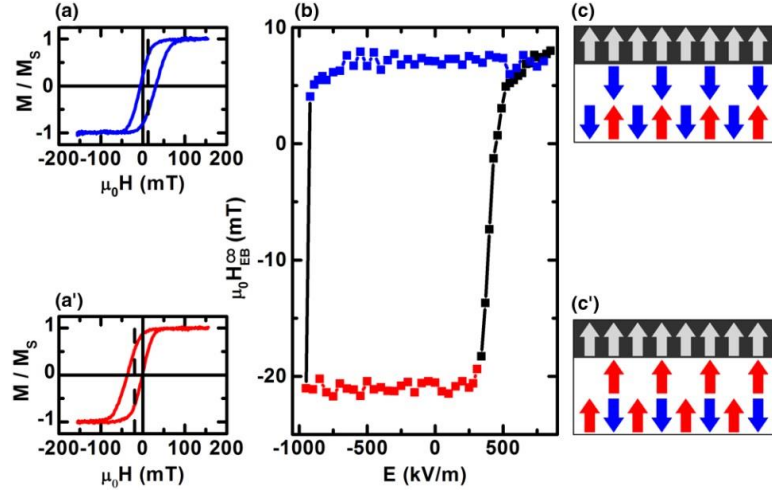


Figure 1.4 The details of switching in a perpendicular anisotropic heterostructure Cr_2O_3 (0001)/Pd(0.5 nm)/(Co(0.6 nm)/Pd(1.0 nm))₃. The hysteresis loop of magnetoelectric annealed CoPd thin film with (a) positive and (a') negative exchange bias, respectively. (b) The applied electric field dependent hysteretic behavior. The diagrams illustration of Cr_2O_3 boundary magnetism/spin structure in the (c) positive and (c') negative exchange bias states. (Reprinted with permission adapted from Ref. [69], copyright (2013))

1.5 Thesis Layout

In this thesis, I first present our research on the development of spintronic devices nanofabrication technique based on shadow mask and E-beam angle deposition in Chapter 2. In Chapter 3, I discuss the spin orbit effect (SOE) of 3d light transition metal vanadium, which has been demonstrated to have a large spin Hall angle and large spin diffusion length. In Chapter 4, the existence of topological surface state (TSS) has been demonstrated in $\text{Bi}_2\text{Se}_3/\text{Co}$ heterostructure. In Chapter 5, our latest work of the SOE in FMs has been discussed. A spin rotation symmetry has been found at FM/NM interface which is related with the symmetry breaking that is introduced by ferromagnetic order in FM layer. Finally, I give my final remark to conclude my thesis in Chapter 6.

REFERENCES

- [1] M. N. Baibich, J. M. Broto, A. Fert, F. N. Van Dau, F. Petroff, P. Eitenne, G. Creuzet, A. Friederich, and J. Chazelas, *Phys. Rev. Lett.* **61**, 2472 (1988).
- [2] G. Binasch, P. Grünberg, F. Saurenbach, and W. Zinn, *Phys. Rev. B* **39**, 4828 (1989).
- [3] B. Dieny, V. S. Speriosu, S. S. P. Parkin, B. A. Gurney, D. R. Wilhoit, and D. Mauri, *Phys. Rev. B* **43**, 1297 (1991).
- [4] N. F. Mott, *Proc. Phys. Sci.* **153**, 699 (1936).
- [5] A. Fert and I. A. Campbell, *Phys. Rev. Lett.* **21**, 1190 (1968).
- [6] R. Coehoorn, J. C. S. Kools, T. G. S. M. Rijks, and K.-M. H. Lenssen, *Philips J. Res.* **51**, 93 (1998).
- [7] S. P. Parkin, in *Spin Depend. Transp. Magn. Nanostructures* (CRC Press, 2002).
- [8] C. Chappert, A. Fert, and F. N. Van Dau, *Nat. Mater.* **6**, 813 (2007).
- [9] J. S. Moodera, L. R. Kinder, T. M. Wong, and R. Meservey, *Phys. Rev. Lett.* **74**, 3273 (1995).
- [10] T. Miyazaki and N. Tezuka, *J. Magn. Magn. Mater.* **139**, (1995).
- [11] S. Yuasa, T. Nagahama, A. Fukushima, Y. Suzuki, and K. Ando, *Nat Mater* **3**, 868 (2004).
- [12] S. S. P. Parkin, C. Kaiser, A. Panchula, P. M. Rice, B. Hughes, M. Samant, and S.-H. Yang, *Nat. Mater.* **3**, 862 (2004).
- [13] Y. M. Lee, J. Hayakawa, S. Ikeda, F. Matsukura, and H. Ohno, *Appl. Phys. Lett.* **90**, 212507 (2007).
- [14] S.-W. Lee and K.-J. Lee, *Proc. IEEE* **104**, 1831 (2016).

- [15] J. C. Slonczewski, *J. Magn. Magn. Mater.* **159**, L1 (1996).
- [16] L. Berger, *Phys. Rev. B* **54**, 9353 (1996).
- [17] E. B. Myers, *Science* **285**, 867 (1999).
- [18] J. Katine, F. Albert, R. Buhrman, E. Myers, and D. Ralph, *Phys. Rev. Lett.* **84**, 3149 (2000).
- [19] Y. Huai, F. Albert, P. Nguyen, M. Pakala, and T. Valet, *Appl. Phys. Lett.* **84**, 3118 (2004).
- [20] G. D. Fuchs, N. C. Emley, I. N. Krivorotov, P. M. Braganca, E. M. Ryan, S. I. Kiselev, J. C. Sankey, D. C. Ralph, R. A. Buhrman, and J. A. Katine, *Appl. Phys. Lett.* **85**, 1205 (2004).
- [21] H. Kubota, A. Fukushima, Y. Ootani, S. Yuasa, K. Ando, H. Maehara, K. Tsunekawa, D. D. Djayaprawira, N. Watanabe, and Y. Suzuki, *IEEE Trans. Magn.* **41**, 2633 (2005).
- [22] Z. Diao, D. Apalkov, M. Pakala, Y. Ding, A. Panchula, and Y. Huai, *Appl. Phys. Lett.* **87**, 232502 (2005).
- [23] S. Ikeda, K. Miura, H. Yamamoto, K. Mizunuma, H. D. Gan, M. Endo, S. Kanai, J. Hayakawa, F. Matsukura, and H. Ohno, *Nat. Mater.* **9**, 721 (2010).
- [24] D. Apalkov, S. Watts, A. Driskill-Smith, E. Chen, Z. Diao, and V. Nikitin, *IEEE Trans. Magn.* **46**, 2240 (2010).
- [25] A. Brataas, A. D. Kent, and H. Ohno, *Nat. Mater.* **11**, 372 (2012).
- [26] M. Hosomi, H. Yamagishi, T. Yamamoto, K. Bessho, Y. Higo, K. Yamane, H. Yamada, M. Shoji, H. Hachino, C. Fukumoto, H. Nagao, and H. Kano, *IEEE Int. Devices Meet. 2005. IEDM Tech. Dig.* **0**, 459 (2005).
- [27] T. Kawahara, R. Takemura, K. Miura, J. Hayakawa, S. Ikeda, Y. M. Lee, R. Sasaki, Y. Goto, K. Ito, T. Meguro, F. Matsukura, H. Takahashi, H. Matsuoka, and H. Ohno, *IEEE J. Solid-State Circuits* **43**, 109 (2008).
- [28] R. Takemura, T. Kawahara, K. Miura, H. Yamamoto, J. Hayakawa, N. Matsuzaki, K. Ono, M. Yamanouchi, K. Ito, H. Takahashi, S. Ikeda, H. Hasegawa, H. Matsuoka, and H. Ohno, *IEEE J. Solid-State Circuits* **45**, 869 (2010).
- [29] K. Tsuchida, T. Inaba, K. Fujita, Y. Ueda, T. Shimizu, Y. Asao, T. Kajiyama,

- M. Iwayama, K. Sugiura, S. Ikegawa, T. Kishi, T. Kai, M. Amano, N. Shimomura, H. Yoda, and Y. Watanabe, in *2010 IEEE Int. Solid-State Circuits Conf.* **53**, 258 (2010).
- [30] P. Gambardella and I. M. Miron, *Philos. Trans. R. Soc. A Math. Phys. Eng. Sci.* **369**, 3175 (2011).
- [31] I. M. Miron, K. Garello, G. Gaudin, P.-J. Zermatten, M. V Costache, S. Auffret, S. Bandiera, B. Rodmacq, A. Schuhl, and P. Gambardella, *Nature* **476**, 189 (2011).
- [32] L. Liu, O. J. Lee, T. J. Gudmundsen, D. C. Ralph, and R. A. Buhrman, *Phys. Rev. Lett.* **109**, 096602 (2012).
- [33] L. Liu, C.-F. Pai, Y. Li, H. W. Tseng, D. C. Ralph, and R. A. Buhrman, *Science* **336**, 555 (2012).
- [34] P. P. J. Haazen, E. Murè, J. H. Franken, R. Lavrijsen, H. J. M. Swagten, and B. Koopmans, *Nat. Mater.* **12**, 299 (2013).
- [35] K.-S. Ryu, L. Thomas, S.-H. Yang, and S. Parkin, *Nat. Nanotechnol.* **8**, 527 (2013).
- [36] S. Emori, U. Bauer, S.-M. Ahn, E. Martinez, and G. S. D. Beach, *Nat. Mater.* **12**, 611 (2013).
- [37] S. Urazhdin, V. Tiberkevich, and A. Slavin, *Phys. Rev. Lett.* **105**, 237204 (2010).
- [38] Z. Duan, A. Smith, L. Yang, B. Youngblood, J. Lindner, V. E. Demidov, S. O. Demokritov, and I. N. Krivorotov, *Nat. Commun.* **5**, 5616 (2014).
- [39] M. I. Dyakonov and V. I. Perel, *Sov. Physics, JETP* **33**, 1053 (1971).
- [40] M. I. Dyakonov and V. I. Perel, *Phys. Lett. A* **35**, 459 (1971).
- [41] J. E. Hirsch, *Phys. Rev. Lett.* **83**, 1834 (1999).
- [42] S. Zhang, *Phys. Rev. Lett.* **85**, 393 (2000).
- [43] L. Liu, T. Moriyama, D. C. Ralph, and R. A. Buhrman, *Phys. Rev. Lett.* **106**, 036601 (2011).
- [44] X. Fan, J. Wu, Y. Chen, M. J. Jerry, H. Zhang, and J. Q. Xiao, *Nat. Commun.* **4**, 1799 (2013).

- [45] T. Nan, S. Emori, C. T. Boone, X. Wang, T. M. Oxholm, J. G. Jones, B. M. Howe, G. J. Brown, and N. X. Sun, *Phys. Rev. B* **91**, 214416 (2015).
- [46] X. Fan, H. Celik, J. Wu, C. Ni, K. Lee, V. O. Lorenz, and J. Q. Xiao, *Nat. Commun.* **5**, 1 (2014).
- [47] Y. Ou, S. Shi, D. C. Ralph, and R. A. Buhrman, *Phys. Rev. B* **93**, 220405 (2016).
- [48] Y. A. Bychkov and E. I. Rashba, *JETP Lett.* **39**, 78 (1984).
- [49] A. Manchon and S. Zhang, *Phys. Rev. B* **78**, 212405 (2008).
- [50] A. Manchon and S. Zhang, *Phys. Rev. B* **79**, 094422 (2009).
- [51] A. Manchon, ArXiv E-Prints 1204.4869 (2012).
- [52] P. M. Haney, H.-W. Lee, K.-J. Lee, A. Manchon, and M. D. Stiles, *Phys. Rev. B* **87**, 174411 (2013).
- [53] K.-W. Kim, H.-W. Lee, K.-J. Lee, and M. D. Stiles, *Phys. Rev. Lett.* **111**, 216601 (2013).
- [54] A. Kundu and S. Zhang, *Phys. Rev. B* **92**, 094434 (2015).
- [55] X. L. Qi and S. C. Zhang, *Rev. Mod. Phys.* **83**, 1057 (2011).
- [56] M. Z. Hasan and C. L. Kane, *Rev. Mod. Phys.* **82**, 3045 (2010).
- [57] J. E. Moore, *Nature* **464**, 194 (2010).
- [58] D. Pesin and A. H. MacDonald, *Nat. Mater.* **11**, 409 (2012).
- [59] A. K. Geim, *Science* **324**, 1530 (2009).
- [60] M. Gmitra, S. Konschuh, C. Ertler, C. Ambrosch-Draxl, and J. Fabian, *Phys. Rev. B* **80**, 235431 (2009).
- [61] W. Han, R. K. Kawakami, M. Gmitra, and J. Fabian, *Nat. Nanotechnol.* **9**, 794 (2014).
- [62] Y. Ando, *J. Phys. Soc. Japan* **82**, 1 (2013).
- [63] D. Hsieh, Y. Xia, D. Qian, L. Wray, J. H. Dil, F. Meier, J. Osterwalder, L. Patthey, J. G. Checkelsky, N. P. Ong, A. V Fedorov, H. Lin, A. Bansil, D.

- Grauer, Y. S. Hor, R. J. Cava, and M. Z. Hasan, *Nature* **460**, 1101 (2009).
- [64] S.-Y. Xu, Y. Xia, L. A. Wray, S. Jia, F. Meier, J. H. Dil, J. Osterwalder, B. Slomski, A. Bansil, H. Lin, R. J. Cava, and M. Z. Hasan, *Science* **332**, 560 (2011).
- [65] O. V. Yazyev, J. E. Moore, and S. G. Louie, *Phys. Rev. Lett.* **105**, 266806 (2010).
- [66] W.-G. Wang, M. Li, S. Hageman, and C. L. Chien, *Nat. Mater.* **11**, 64 (2012).
- [67] F. Matsukura, Y. Tokura, and H. Ohno, *Nat. Nanotechnol.* **10**, 209 (2015).
- [68] X. He, Y. Wang, N. Wu, A. N. Caruso, E. Vescovo, K. D. Belashchenko, P. A. Dowben, and C. Binek, *Nat. Mater.* **9**, 579 (2010).
- [69] W. Echtenkamp and C. Binek, *Phys. Rev. Lett.* **111**, 187204 (2013).

Chapter 2

FABRICATION OF SPINTRONIC DEVICES WITH SHADOW MASK TECHNIQUE

2.1 Introduction

Fabrication of spintronics devices is quite complicated and some time is challenging. For example, to fabricate magnetoelectric (ME) devices as shown in Figure 2.1, we must put electrical contact on the middle FM electrode which is only a few nanometers thick. To circumvent this type of problem and reduce the fabrication steps, we have developed a nanofabrication technique by using shadow masks.

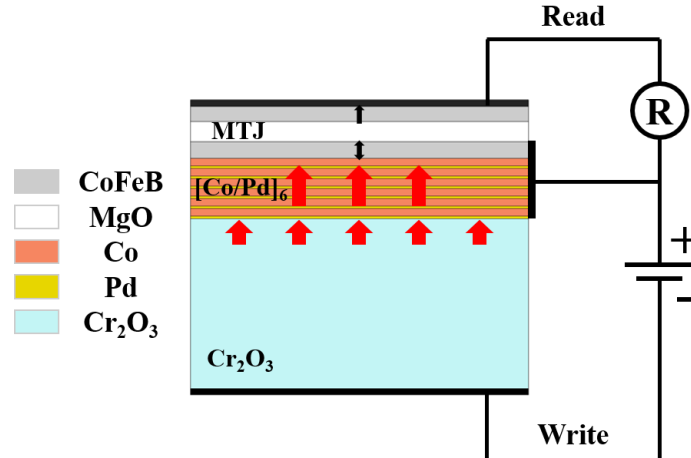


Figure 2.1 The prototype of ME device with antiferromagnet Cr₂O₃ and MgO-based MTJ. The surface magnetism at [Co/Pd]_n/Cr₂O₃ interface could be switched by voltage-controlled exchange coupling. The CoFeB free layer in MgO-MTJ could also be switched when [Co/Pd]_n film is changing its magnetization.

2.2 Shadow Mask Technique

Shadow mask was first developed for fabricating Josephson junctions using E-beam lithography [1]. It is a simple and robust technique of additive fabrication which is normally consisted with two layers of E-beam resists [2-4]. The bottom layer works as “sacrificial layer” and as “support layer” to support the top suspended “bridge layer”.

2.2.1 General Procedure

The general shadow mask fabrication procedure is shown in Figure 2.2 and summarized below:

- (a) The substrate is cleaned following the standard substrate cleaning procedure to completely remove all organic contaminants (organic films, residues, photoresist, oil, etc.) on substrate;
- (b) Two layers of E-beam resist are spin-coated to build bilayer shadow mask with “support layer” and “bridge layer”;
- (c) E-beam lithography process is performed to transfer the designed pattern to the resist bilayer;
- (d) The sample go through the first develop process to partially remove the top bridge layer according to the pattern;
- (e) The bottom resist is partially removed via a second develop process. The undercut extension length is development time controlled, which is a crucial parameter in shadow mask design;
- (f) and (g) Desired materials are deposited at different locations via E-beam evaporation at different angle;
- (h) The shadow mask is removed to expose the device.

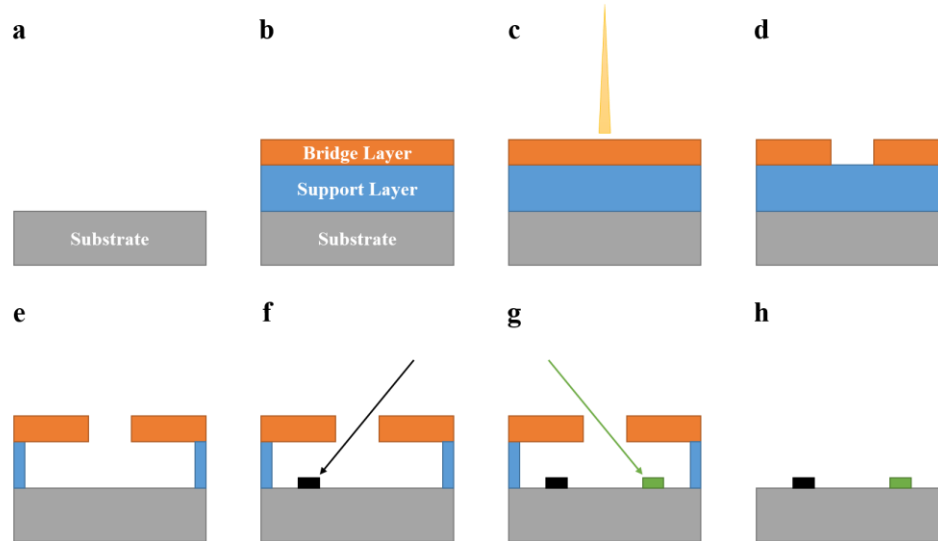


Figure 2.2 The schematic illustration of the shadow mask evaporation general procedure. (a) Substrate cleaning; (b) Spin coating of bilayer E-beam resists; (c) E-beam writing process; (d) Bridge layer development; (e) Support layer development; (f) E-beam evaporation at angle 1; (g) E-beam evaporation at angle 2; (h) Shadow mask lift-off process.

2.2.2 Shadow Mask Fabrication

The formation of suspended shadow mask structure is the most important feature. Various materials have been selected to work as the “bridge layer” which requires high-resolution and good mechanical strength. Commonly used materials include Poly-Methyl Methacrylate (PMMA), ZEP520 series positive E-beam resist, CSAR resist (used in this study), silicon and even metallic layers. For the support layer, PMGI (LOR) series resists are widely used.

2.2.2.1 PMMA-based Shadow Mask

Bilayers of poly methyl methacrylate (PMMA)/poly methyl glutarimide (PMGI) is the most common structure used for bilayer shadow mask, which shows high resolution and processing simplicity. Below is the recipe used in this work:

1. Substrate is cleaned sequentially with acetone, ethanol and D.I water, accompanied with sonic agitation of 15 min in each cleaning solution. The cleaned substrate is blow-dried with nitrogen gas;
2. The substrate is spin-coated with PMGI at 3000 rpm for 60 s, followed by baking at 210°C for 3 min;
3. PMMA is spin-coated at 5000 rpm for 60 s, followed by baking at 190°C for 4 min;
4. Patterns are generated via E-beam writing process in UD Nanofabrication Facility (UDNF);
5. PMMA bridge layer was developed in MIKI developer for 90 s, followed by the second developing in IPA solvent for 30 s. The sample is then blow-dried with nitrogen;
6. PMGI support layer developing process in XP101 developer for 5 mins (Developing time may vary to create different undercut extension. 5mins developing time will achieve approximately 1 μ m undercut), followed by blow-drying with nitrogen.

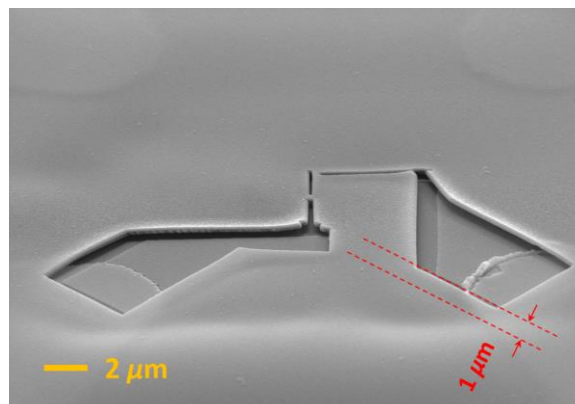


Figure 2.3 The SEM image of PMMA/PMGI shadow mask.

As shown in Figure 2.3, the 1 μ m undercut has been created in this 200 nm PMMA/300 nm PMGI shadow mask. The bridge layer PMMA is suspended on top of

the support layer of PMGI. Due to different sensitivities of two resists under the same E-beam dosage, there will be different dissolution rates of the PMMA and PMGI resists in the subsequent development steps. When the PMMA/PMGI bilayer is being developed in MIKI (1min 30s) and IPA developers (30s), the top PMMA layer development will be finished. The bottom layer PMGI will be dissolved in another developer XP101. For a typical PMMA/PMGI bilayer shadow mask, we found the optimum PMGI development time is 5min 30s, which could create a 1 μ m undercut.

2.2.2.2 CSAR-based Shadow Mask

CSAR 62 (AR-P 6200), whose main component is poly-methylstyrene-co-methyl chloroacrylate, is a positive E-beam resist that has ultrahigh sensitivity, contrast, high processing and plasma etching stability. As the result, CSAR 62 E-beam resist has the highest resolution of about 10nm. It is a good alternative candidate for the shadow mask bridge layer due to its high mechanical strength comparing with the PMMA E-beam resist.

This newly developed CSAR E-beam resist has been tested for shadow mask applications. Specifically, two types of CSARs (AR-P 6200.04 and 09) have been tested. AR-P 6200.04 is the thinnest resist in CSAR series, which could attain 6nm ultra-high resolution and is used as bridge layer. The plasma etching rate of AR-P 6200.09 is comparable with other photoresists and ZEP 520A in CF_4+O_2 plasma. In Figure 2.4, the CSAR positive E-beam lithography resist has shown superior RIE etching resistance than PMMA during the pattern transfer process.

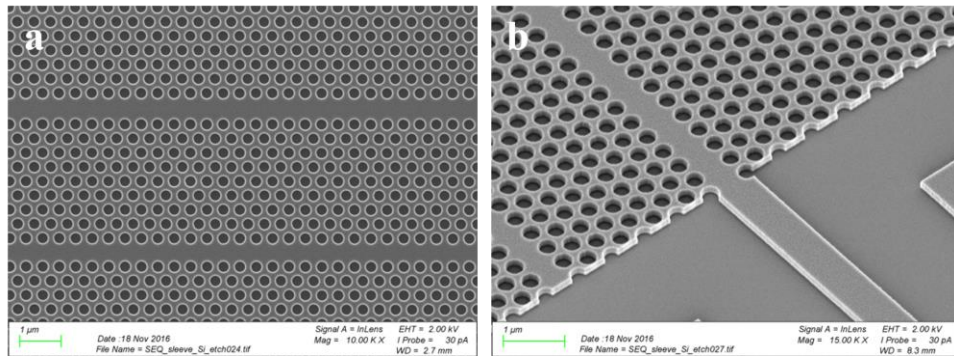


Figure 2.4 The RIE test on CSAR positive tone E-beam resist. The CSAR has shown high plasma etching resistance, which makes CSAR a good alternative candidate of PMMA as the bridge layer in bilayer shadow mask.

The undercut control test has been performed on the CSAR/LOR 3A shadow mask. In Figure 2.5 (a), a CSAR/LOR 3A shadow mask has been developed for five minutes and more than 1 μm undercut has been created in AR 300-47 LOR developer. Figure 2.5 (b) plots out the relation between development duration and the undercut of the LOR 3A support layer.

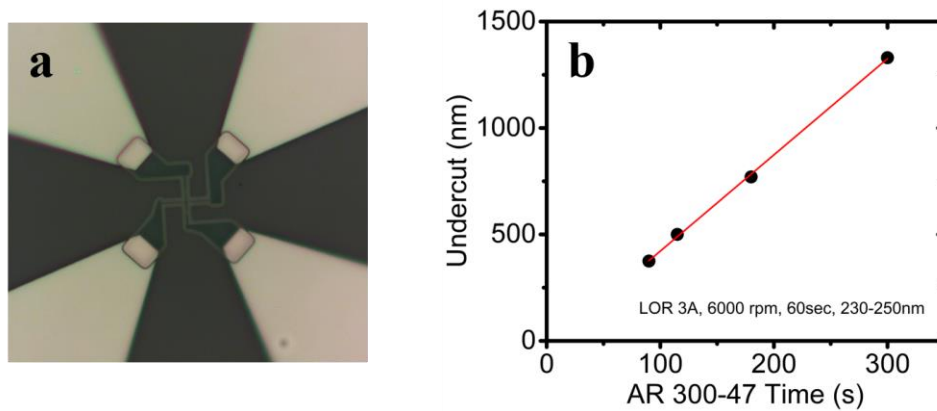


Figure 2.5 (a) The optical image of CSAR/LOR3A shadow mask with $1\mu\text{m}$ undercut. (b) The relation between development duration and undercut opening size of LOR 3A resist in the developer AR 300-47.

Two recipes based on CSAR/LOR bilayer E-beam resists have been tested in the E-beam lithography procedure. Below we list the associated steps for the CSAR 04/LOR 3A bilayer recipe:

1. Substrate cleaning;
2. LOR 3A spin coating at 6000 rpm for 60 s;
3. 5 min baking at 200°C ;
4. CSAR 04 spin coating at 2000 rpm for 60 s;
5. 5min baking at 170°C ;
6. E-beam writing with Vistec E-beam writer for CSAR 04/LOR 3A bilayer resists in UDNF;
7. CSAR 04 development in AR 600-546 for 35 s, IPA rinse, blow-drying with N_2 ;
8. LOR 3A development in AR 300-47 for 60 s, DI water rinse, blow-drying with N_2 .

This is a standard bilayer resists recipe for lift off E-beam lithography process, with a small undercut of 80nm, and the thicknesses of CSAR and LOR are 85 nm and 235 nm, respectively. Another CSAR 09/LOR 5A shadow mask has also been developed as following:

1. Substrate cleaning;
2. LOR 5A spin coating at 6000 rpm for 60 s;
3. 5 min baking at 200°C;
4. CSAR 09 spin coating at 4000 rpm for 60 s;
5. 5min baking at 170°C;
6. E-beam writing with UDNF internal recipe for CSAR 09/LOR 5A bilayer resists;
7. CSAR 09 development in AR 600-546 for 35 s, IPA rinse, blow-drying with N₂;
8. LOR 5A development in AR 300-47 for 105 s, DI water rinse, blow-drying with N₂.

This 100 nm CSAR/300 nm LOR shadow mask will possess around 0.5 μm undercut, which has been chosen as the recipe of nanodevices fabrication used in this thesis study.

2.2.3 Electron Beam Evaporation

The shadow mask based nanofabrication technique uses electron beam evaporation to fabricate materials. Electron beam evaporation is a material deposition technique in which an electron beam is used to heat up target material in ultrahigh vacuum environment of the order of 10^{-8} Torr. The heated target material is vaporized and deposited on a substrate in line-of-sight fashion (the vapor particles have a very

long mean free path in the ultrahigh vacuum chamber). In contrast, the magnetron sputtering technique, which is also used in this research, has poorer directionality than the electron beam evaporation process, because of its much higher working pressure of the order of mTorr. The high directionality of E-beam evaporation process becomes advantageous since the films at different locations can be deposited using different angle of the E-beam with respect to the shadow mask.

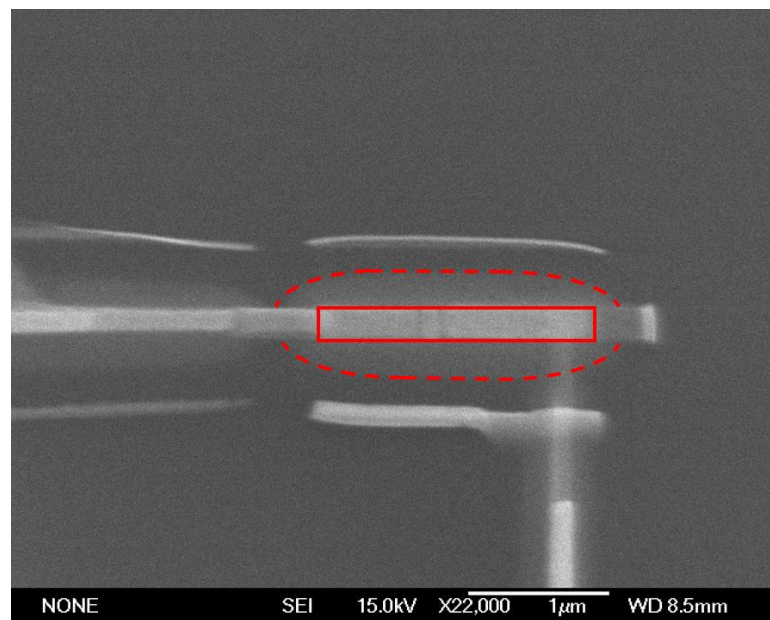


Figure 2.6 The SEM image of the nano MTJ device that was fabricated using shadow mask technique. The rectangle solid box indicates the profile of the shadow mask aperture. After both E-beam evaporation and magnetron sputtering deposition, due to different directionality of the two deposition methods, the film on the substrate through E-beam evaporation is confined in the rectangle solid box. By contrast, the film deposited with magnetron sputtering through the same shadow mask is expanded into the red dash elliptical shape.

A comparison of the deposition directionality between the E-beam evaporation and the magnetron sputtering can be seen in Figure 2.6. Because of line-of-sight deposition of the E-beam evaporation, the E-beam evaporated film is confined in rectangular shape defined by the shadow mask aperture (red solid line). The magnetron sputtered film smeared into elliptical shape that is almost three times wider than the shadow mask aperture (dashed red line).

2.3 Nano Devices Fabrication

Devices in Hall bar structure and MTJs have been fabricated by using the shadow mask technique. The width of shadow mask is in the range of ~ 100 nm. For the purpose of electric measurements, one needs to prepare large μm scale contact pads before the shadow mask evaporation process. The contact pads can be prepared by both E-beam lithography and conventional photo lithography. E-beam lithography has high resolution and high interlayer alignment accuracy. In comparison, the photo lithography process is simple but with limited pattern-transfer accuracy. Therefore, the usual procedure of making nanodevices with shadow mask consists of several steps combining both E-beam lithography and photo lithography as shown in Figure 2.7. The shadow mask or other patterns (contact pads, alignment markers, etc.) is first designed with CAD software such as Autodesk[®] AutoCAD. The UDNF prefers the use of CleWin 5.2 Layout Editor that is more convenient to operate the Vistec EBP5200ES E-beam writer. After the pattern design, the first layer of contact pads are fabricated by E-beam lithography or photo lithography. Meanwhile, the first layer of E-beam writer alignment mark is also made in this level by the same E-beam lithography process. Alternatively, the alignment mark can be prepared separately from photo lithography. The bilayer shadow mask is then prepared. Depending on

material deposition requirements, either 200 nm PMMA/300 nm PMGI or 100 nm CSAR/300 nm LOR bilayers can be used. Next, the magnetron sputtering is used to deposit multilayer structures through the shadow mask (e.g. $[\text{Co}/\text{Pd}]_n$ multilayer with perpendicular magnetic anisotropy (PMA) or AlO_x/MgO -based full stack of MTJs). Finally, the multi-angle E-beam evaporation is used to make electrodes connections between the nanodevices and the contact pads.

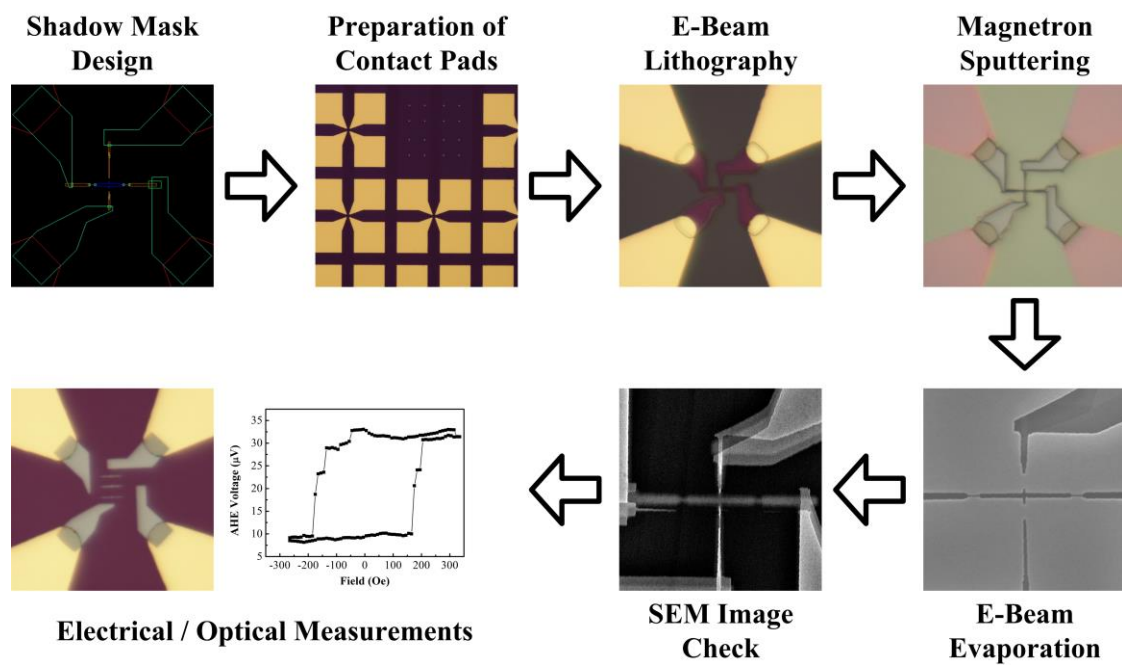


Figure 2.7 The flow chart of nanofabrication procedure based on shadow mask technique.

2.3.1 Hall Bar Structure

The PMMA/PMGI shadow mask has been used to fabricate Hall bar structure. Multilayer of $\text{Pd}(0.5)/[\text{Co}(0.3)/\text{Pd}(0.9)]_6$ (the values in the parentheses represent the thickness in nm) is a typical magnetic heterostructures with PMA, which is the best

grown with magnetron sputtering. The fabrication of Hall bar structure is divided into three major stages: shadow mask fabrication, magnetron sputtering of the PMA multilayer, and E-beam evaporation for contact pads connection. Large $180\ \mu\text{m} \times 180\ \mu\text{m}$ contact pads plus E-beam lithography alignment markers were prepared by conventional photo lithography on Si/SiO₂ wafers or Cr₂O₃ samples. The typical contact pad image and alignment markers are shown in Figure 2.8 (a).and (b), respectively.

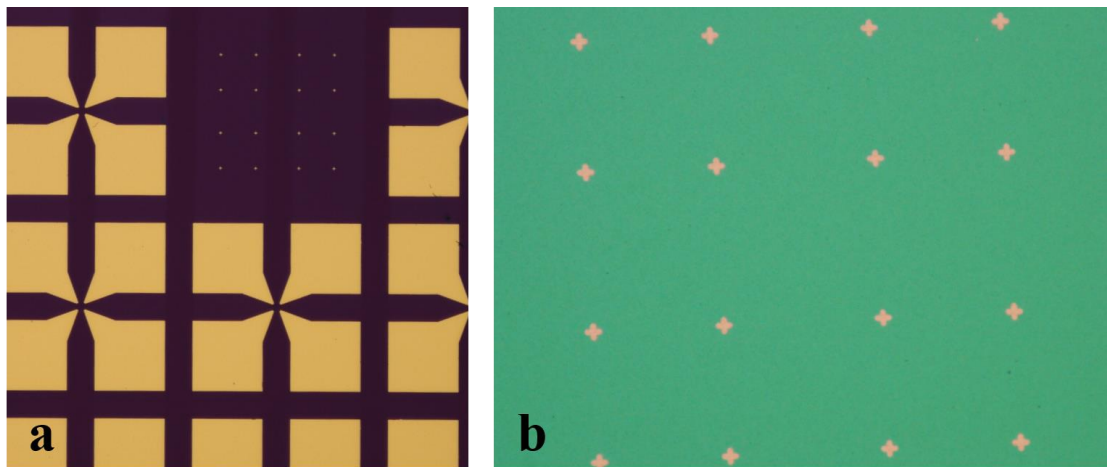


Figure 2.8 The microscopy images of typical (a) contact pads ($180\ \mu\text{m} \times 180\ \mu\text{m}$) on Si/SiO₂ wafer and (b) E-beam alignment markers ($10\ \mu\text{m} \times 10\ \mu\text{m}$) on Cr₂O₃ sample.

2.3.1.1 Hall Bar Shadow Mask

The Hall bar shadow mask design is shown as the red-colored area in Figure 2.9 (a), and the purple-colored represents the pre-fabricated contact pads (Ta(10nm)/Au(80nm)). The overlap area that is marked with “①” in Figure 2.9 (a) is a $3\ \mu\text{m} \times 5\ \mu\text{m}$ region which has been designed as the connection between Hall bar structure and

contact pads. Figure 2.9 (b) shows intentionally open gaps on the Hall voltage arms marked with “②”. The width of the gap is designed as 450 nm. The Hall bar nanowire width is $W = 250$ nm, and the length is $L = 3.6 \mu\text{m}$. At “③” in Figure 2.9 (b), there is a narrow segment on the Hall bar nanowire which is designed to prevent the nanowire from being electrically shorted due to the shadow effect of angle deposition. This is because we use angle deposition of Au to fill the gap “②” to connect to the contact pad. This Au deposition will also go through the horizontal opening of the shadow mask and deposit an Au line parallel to the Hall bar structures. This Au film will connect two contact pads at left and right, shorting the Hall bar device. The narrower segment with a width of ~ 80 nm can block the angle deposited Au, thus preventing the device from electrical shorting.

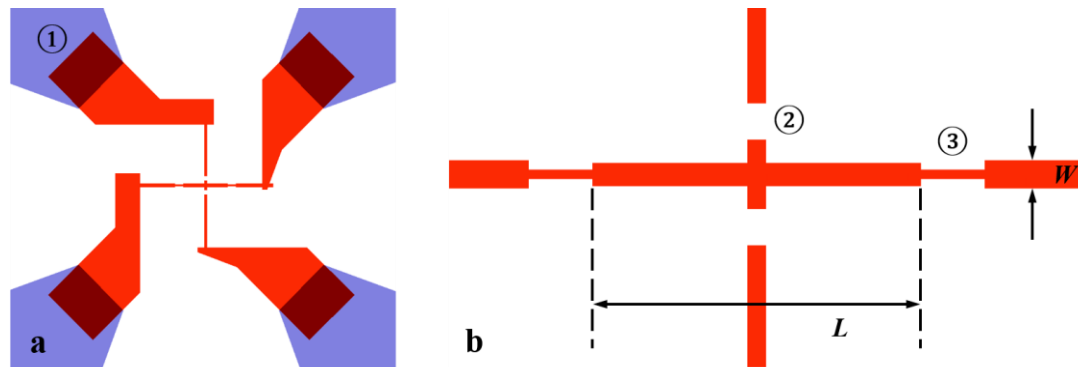


Figure 2.9 The Hall bar shadow mask design. (a) The purple area represents the contact pads, and (b) the red area is the shadow mask aperture (opening) defined by E-beam writer.

The PMMA/PMGI recipe has been discussed in session 2.2.2.1. The PMMA E-beam resist used in this research is the product of Microchem[®] 950 PMMA A4 and

the PMGI E-beam resist is Microchem[®] SF6 which is designed to have high resolution, good deposition line width control, and easy processing *et al.* As shown in Figure 2.10 (a), the PMMA bridge layer development procedure was done in MIBK:IPA of 1:3 ratio developer for 90 s, then rinsed in IPA solution for 30 s which completely stopped the development process and prevent the E-beam resist from over developed. From the microscope image, we can confirm the formation of a clear and well-defined pattern. In Figure 2.10 (b), after the pattern was transferred on the PMMA layer, the sample was left in XP101A developer for 5 min, followed by 30s D.I. water rinsing, and N₂ flow-drying. The undercut can be controlled by the development time. 5 min and 30s development time led to $\sim 1 \mu\text{m}$ undercut.

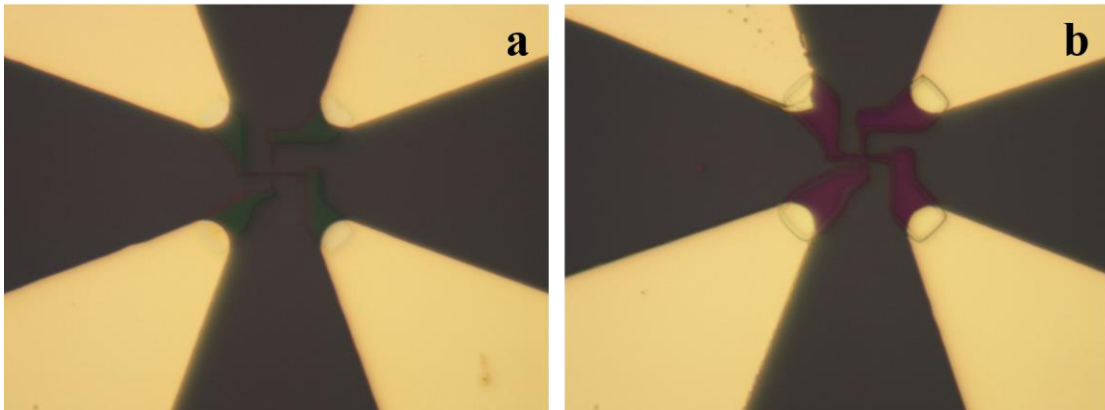


Figure 2.10 The development process of the PMMA/PMGI shadow mask. (a) PMMA layer development in MIBK for 90s and in IPA for 30s. (b) PMGI layer development in XP101A for 5min 30s.

2.3.1.2 Deposition

Due to the less-directional magnetron sputtering, the deposition rate of magnetron sputtering with shadow mask needs calibration. The Co₄₀Fe₄₀B₂₀ sputtering

rate calibration was performed through the Hall bar shadow mask with straight deposition. The deposition parameters are: DC power 18W, 3mTorr working pressure, and 8 min deposition time. As shown in Figure 2.11, the atomic force microscope (AFM) was used to measure the $\text{Co}_{40}\text{Fe}_{40}\text{B}_{20}$ thickness. The sputtering rates of $\text{Co}_{40}\text{Fe}_{40}\text{B}_{20}$ nanowires with different width of 150 nm, 200 nm and 250 nm are 0.63 Å/sec, 0.68 Å/sec and 0.73 Å/sec, respectively. Because of the nanoscale dimensions of shadow masks, AFM is the most efficient method for the rate calibration.

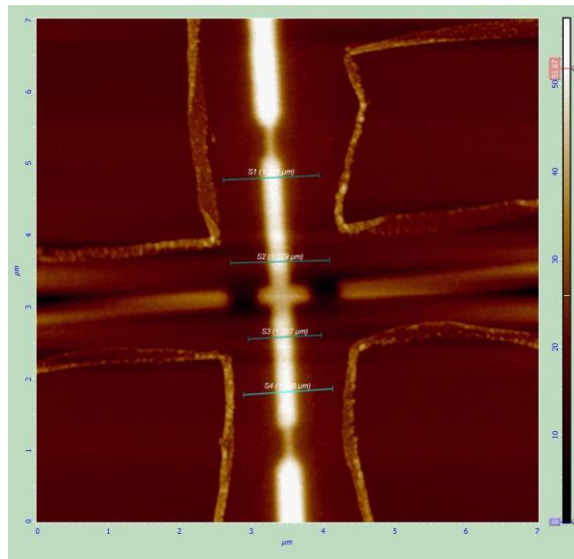


Figure 2.11 The AFM scanning image of the $\text{Co}_{40}\text{Fe}_{40}\text{B}_{20}$ nanowire.

The deposition process of Hall bar structure is shown in Figure 2.12. First, $\text{Pd}(0.5\text{nm})/[\text{Co}(0.3\text{nm})/\text{Pd}(0.9\text{nm})]_6$ multilayer film was deposited by magnetron sputtering with perpendicular (0° incident angle with respect to the normal direction of the sample plane) deposition (Figure 2.12 (a)). The relevant sputtering parameters

are given in Table 2.1. DC power of 7W and 15W were used for depositing Pd and Co layers, respectively.

Table 2.1 The magnetron sputtering recipe for the PMA [Co/Pd]_n multilayers

Type	Layer	Repetitions	Material	Sputtering parameters			
				Pressure (mTorr)	Rate (Å/sec)	Thickness (Å)	
						Layer	Total
Co/Pd	Buffer	× 1	Pd	3	0.83	5	5
	Multi-layer	× 6	Co	3	0.5	3	72
			Pd	3	0.82	9	

The standard contact pads can be either Ta(10nm)/Au(80nm) or Cr(10nm)/Au(80 nm) bilayers. The total thickness of [Co/Pd]_n multilayer is around 10 nm, which leads to almost 80 nm height difference between the contacts and the sample. In order to assure the connection between the contact pads and the Hall bar structure, as illustrated in Figure 2.12 (b) and (c), E-beam evaporation with angle deposition were used to deposit a thick enough Au layer to fill in the 80 nm height difference. In Figure 2.12 (b), the incident angle θ was chosen as 60° . In Figure 2.12 (c), the incident angle was changed to -60° to deposit the other Au electrode in the opposite direction.

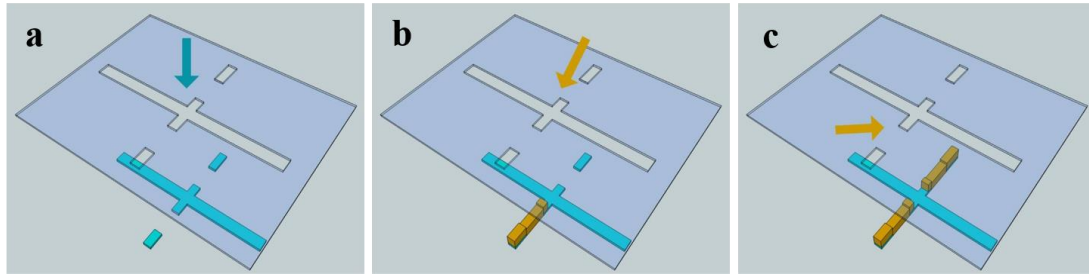


Figure 2.12 The schematic illustration of the deposition process of Hall bar structure with shadow mask. (a) Pd(0.5nm)/[Co(0.3nm)/Pd(0.9nm)]₆ multilayer film with PMA was deposited at 0° incident angle to form Hall bar structure. (b) Au electrode connecting to one of the contact pad was deposited with E-beam evaporation at an incident angle of $\theta = 60^\circ$. (c) Reverse the E-beam incident angle to $\theta = -60^\circ$ connects the other contact pad.

In practice, two steps of angle E-beam evaporation were separated into four steps following the sequence of: 20 nm Au ($\theta = 60^\circ$), 20 nm Au ($\theta = -60^\circ$), 40 nm Au ($\theta = 60^\circ$), and 40 nm Au ($\theta = -60^\circ$). Otherwise, there would be a connection issue which is shown in Figure 2.13. If we just use two steps of E-beam evaporation of 60 nm Au at $\theta = 60^\circ$ and 60 nm Au at $\theta = -60^\circ$, there will still be 60 nm height difference after the first step of E-beam evaporation at $\theta = 60^\circ$. The shadow effect will cause the connection failure of the second Hall electrode deposited at $\theta = -60^\circ$. In Figure 2.13 (a), we can clearly see one Hall electrode that looks normal, but the other one doesn't. As the zoom in SEM image shown in Figure 2.13 (b), the disconnection happens during the second step of 60 nm Au E-beam angle deposition, because of the 60 nm height difference formed during the first step.

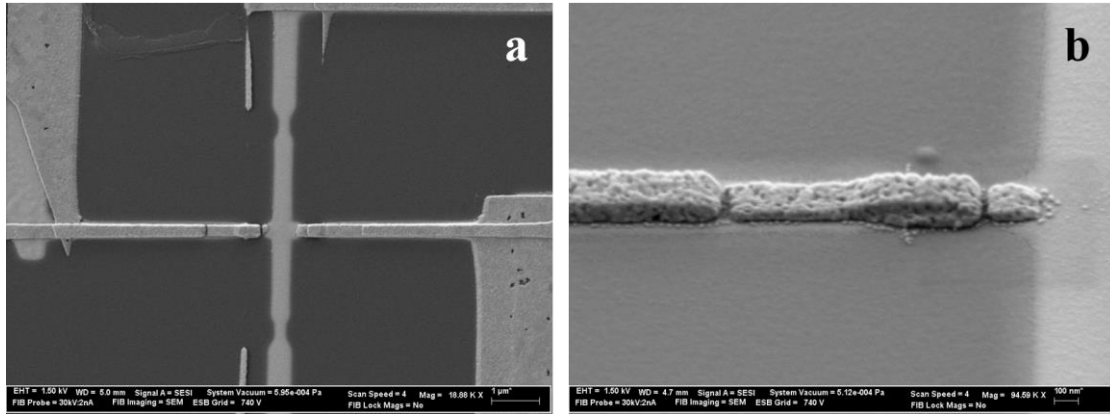


Figure 2.13 The SEM images of E-beam angle deposition issue. (a) Two steps of angle deposition will cause the connection issue which is due to the shadow effect in the E-beam evaporation process. (b) The zoom in image of the disconnection happened on one Hall electrode.

Besides using Au as electrode material, Al, Cu and Ag have also been tested in this shadow mask evaporation procedure. Al electrode is not suitable electrode materials because of its relatively high resistivity. The static charge could easily break the nanodevice as shown in Figure 2.14 (a), the nanowire was burned out at the narrow segment after applying the bias current. In Figure 2.14 (b) and (c), both Cu and Ag electrodes have the adhesion issue, which leads to bad film quality.

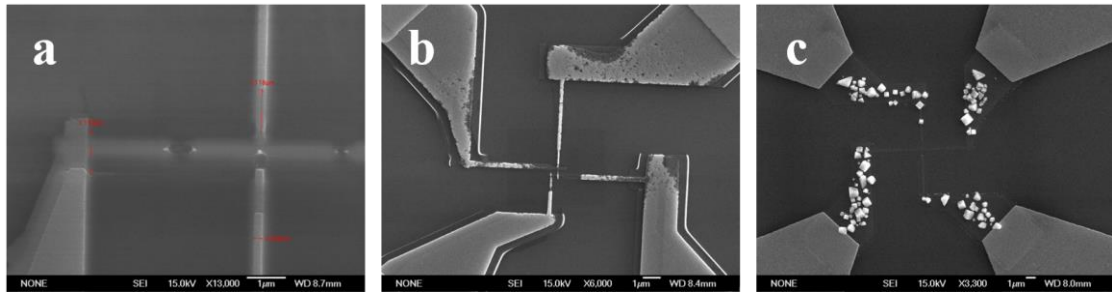


Figure 2.14 The E-beam evaporation test for Al, Cu, and Ag electrode materials. (a) Al electrode will cause the static charging issue. (b) E-beam evaporated Cu electrode has adhesion issue. (c) Ag electrode needs extra buffer layer such as Cr or Ta, otherwise Ag is unable to form a uniform film.

2.3.1.3 Characterization of Nanodevices

As shown in Figure 2.15, the anomalous Hall effect (AHE) electrical measurement has been performed on the $[\text{Co/Pd}]_n$ Hall bar structure. The external magnetic field is applied to the normal of sample plane. This $[\text{Co/Pd}]_n$ PMA sample was post-annealed at 200~210°C for 20 min in an Ar gas environment. Figure 2.15 (b) shows the hysteresis loops of three Hall bars with different wire widths of 200 nm, 250 nm, and 300 nm. The sputtering rates were calibrated based on 250 nm width Hall bar shadow mask. The hysteresis loop also confirms that the nanowire with the width of the 250 nm has the sharpest switching feature.

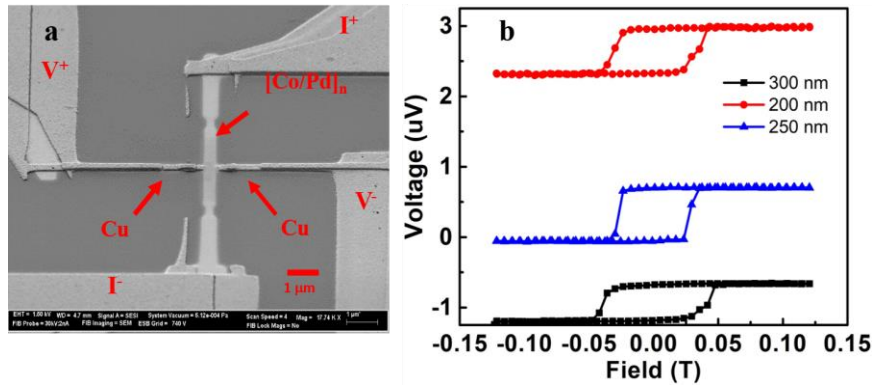


Figure 2.15 (a) The SEM image of $[Co/Pd]_n$ Hall bar structure and (b) the Hall voltage as a function of out-of-plane external field for three individual Hall bar devices with different nanowire width.

2.3.2 Nanofabrication of MTJ Devices

2.3.2.1 MTJ Shadow Mask

A typical MTJ shadow mask is shown in Figure 2.16 (a), the purple areas represent the pre-fabricated $180 \times 180 \mu m^2$ Ta(10nm)/Au(80nm) contact pads, and the red areas indicate the nanostructure written by E-beam writer. In Figure 2.16 (b), the HR-SEM image clearly shows the $1 \mu m$ undercut of the MTJ shadow mask, where the dark area is the shadow mask bottom layer and the bright area indicates the top bridge layer.

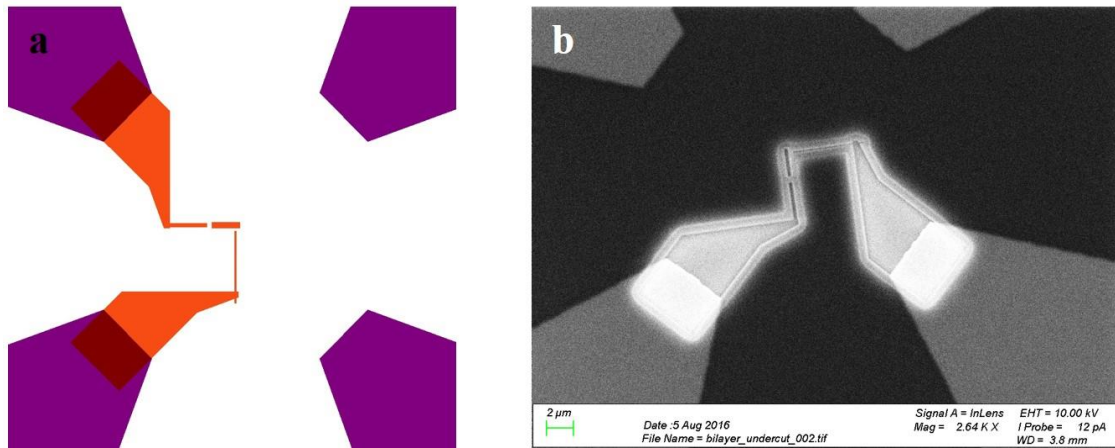


Figure 2.16 The shadow mask design for MTJ nanodevice fabrication. (a) The purple areas represent the contact pads and the red areas are the nanoscale structure defined by E-beam writer. (b) The HR-SEM image of a typical shadow mask of MTJ devices.

A typical MTJ is a two-terminal device which has top and bottom electrodes. Therefore, the MTJ shadow mask design only uses two $180 \times 180 \mu\text{m}^2$ contact pads. The device dimension is $0.4 \mu\text{m} \times 2 \mu\text{m}$, as shown inside the red box in Figure 2.17. E-beam evaporation can be used to fabricate the top and bottom electrodes and make the electrical connections. However, the full stack of MTJ fabrication must be fabricated with magnetron sputtering technique in order to grow AlOx or MgO tunneling barriers with good quality.

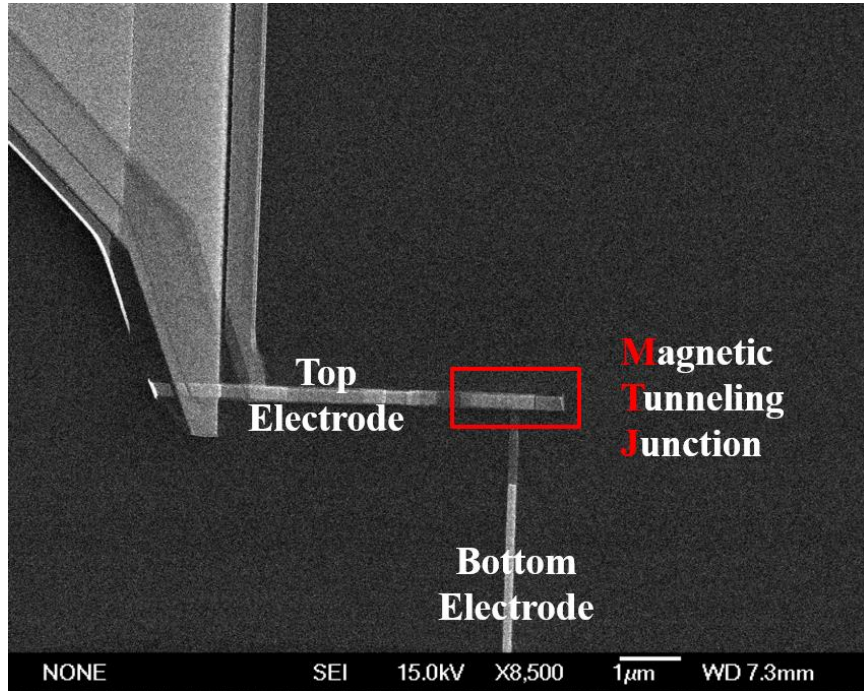


Figure 2.17 The HR-SEM image of a typical AlO_x tunnel junction.

Both the PMMA/PMGI and CSAR/LOR based shadow masks have been tested. As mentioned in Section 2.2.2, the conventional PMMA and PMGI E-beam resists are the most common bilayer shadow mask, because of the processing simplicity and relatively high resolution. However, PMMA shadow mask couldn't sustain the high temperature and UV radiation during the magnetron sputtering, as shown in Figure 2.18 (a). PMMA E-beam resist has a low melting point and PMMA/PMGI shadow mask lose its mechanical strength and chemical stability after 8 min of MgO sputtering.

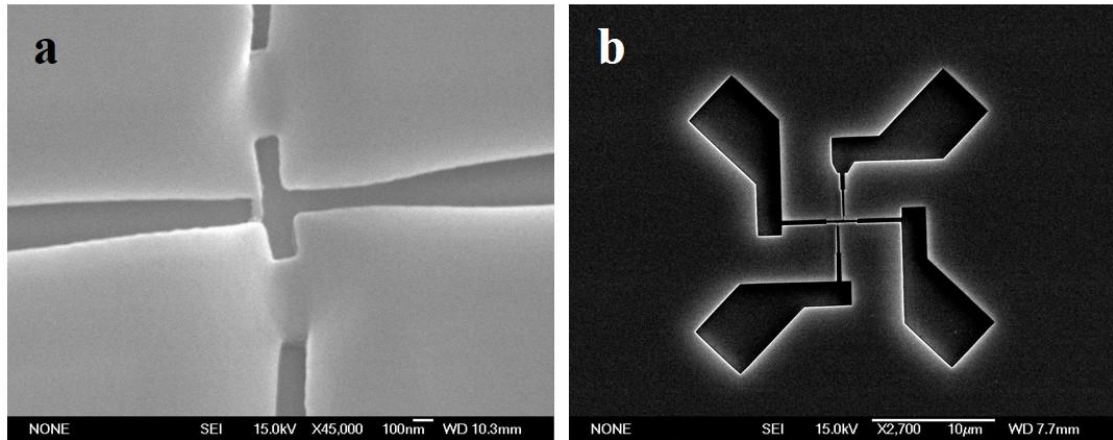


Figure 2.18 The comparison between shadow mask (a) PMMA/PMGI and (b) CSAR 09/LOR 5A after MgO sputtering. CSAR E-beam resist is able to survive under UV irradiation and heating environment.

On the contrary, the CSAR positive tone E-beam resist has been demonstrated to have a superior RIE etching resistance than PMMA. It also has higher resolution with better contrast and sensitivity than PMMA. Therefore, CSAR/LOR bilayer shadow mask is chosen to fabricate devices that require prolonged magnetron sputtering procedure. Although it is a strong UV and electron beam radioactive circumstance, the CSAR/LOR shadow masks survived during the prolonged sputtering process, as shown in Figure 2.18 (b).

2.3.2.2 Deposition Process

The complete deposition process is shown in Figure 2.19. As shown in Figure 2.19 (a), the bottom electrodes was fabricated by E-beam angle evaporation along the direction “①” following the sequence of 10 nm Au deposited at $\theta = 60^\circ$, 110 nm Au deposition at $\theta = -60^\circ$. The sample was then transferred to a magnetron sputtering system. In Figure 2.19 (b), the full stack of MTJs was deposited at $\theta = 0^\circ$ along the

direction of “②”. Both AlOx and MgO based MTJs have been prepared through this shadow mask. After MTJs sputtering process, the sample was transferred into E-beam evaporator. The side wall of the sample with exposed bottom electrode is insulated via a layer of AlOx deposited by E-beam evaporation at $\theta = -57^\circ$ (right) as illustrated in Figure 2.19 (c). AlOx thickness should be chosen properly based on specific MTJ stack. Finally, the top electrode is connected to the contact pad via Au angle deposition. The typical recipe of top electrodes is: 10 nm Au at $\theta = -57^\circ$, 15 nm Au at $\theta = -60^\circ$, 35 nm Au at $\theta = 70^\circ$, and 110 nm Au at $\theta = 0^\circ$.

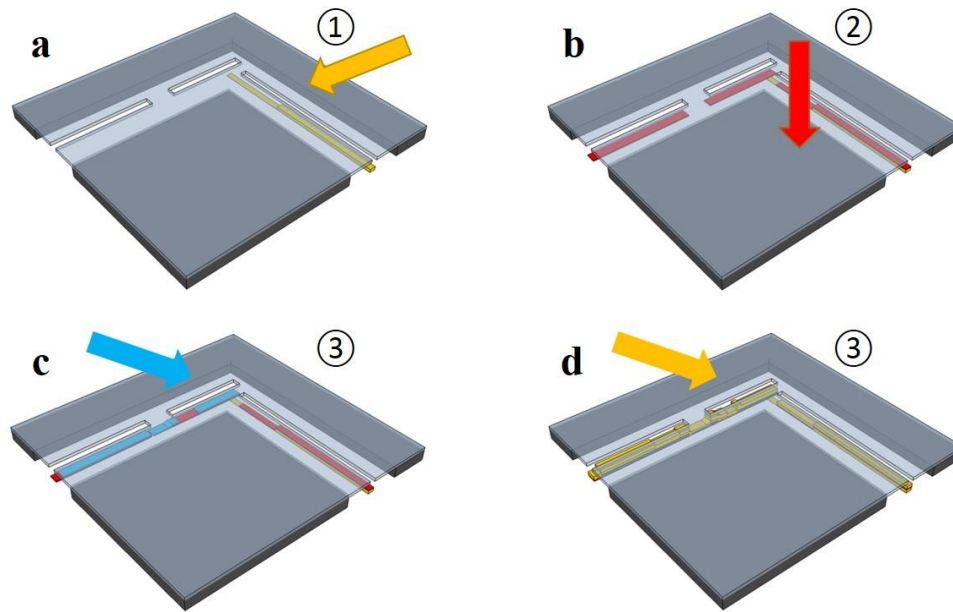


Figure 2.19 The schematic illustration of MTJ device deposition process through shadow mask. (a) E-beam angle evaporation for the bottom electrode; (b) MTJ full stack magnetron sputtering with perpendicular deposition; (c) E-beam angle evaporation of AlOx as the side wall protection; (d) E-beam angle evaporation for top electrodes.

Table 2.2 The recipes to fabricate Pd(0.5nm)/[Co(0.3nm)/Pt(0.9nm)]₆/Co(0.3nm)/AlOx/NiFe(2.0nm)/Ta(2.0nm) and Ta(5.0nm)/CoFeB(0.8nm)/MgO(2.0nm)/CoFeB(1.0nm)/Ta(5.0nm) MTJs via shadow mask technology.

Pd	Pd: 0.5 nm, 7 W, 4.5 mTorr, 6.0 s
[Co/Pd] ₆	Co: 0.3 nm, 15 W, 4.5 mTorr, 6.0 s
	Pd: 0.9 nm, 7 W, 4.5 mTorr, 11.0 s
Co	Co: 0.3 nm, 15 W, 4.5 mTorr, 6.0 s
AlOx	Al: 2.0 nm, 26 W, 4.5 mTorr, 25.0 s
	O ₂ plasma oxidation: RF 120W, 60 mTorr, 150.0 s
Py	Py: 2.0 nm, 25 W, 4.5 mTorr, 22.0 s
Ta	Ta: 2.0 nm, 10 W, 4.5 mTorr, 44.0 s

Ta	Ta: 5.0 nm, 10 W, 3.0 mTorr, 110.0 s
CoFeB	CoFeB: 0.8 nm, 18 W, 2.0 mTorr, 18.0 s
MgO	MgO: 2.0 nm, RF 100 W, 1.2 mTorr, 2+2 min
CoFeB	CoFeB: 1.0 nm, 18 W, 2.0 mTorr, 22.0 s
Ta	Ta: 5.0 nm, 10 W, 3.0 mTorr, 110.0 s

The sputtering rates were calibrated separately. The detailed recipes to fabricate both AlOx and MgO based MTJs via shadow mask technique is summarized in Table 2.2.

2.3.2.3 Characterization of MTJ Nanodevices

Pd(0.5nm)/[Co(0.3nm)/Pt(0.9nm)]₆/Co(0.3nm)/AlOx/NiFe(2.0nm)/Ta(2.0nm) have been successfully prepared through shadow mask, where the bottom Co/Pd electrode has perpendicular anisotropy and the top NiFe electrode has in-plane magnetization. The nonlinear I-V curves and magnetoresistance are shown in Figure 2.20 (a) and (b), respectively.

In Figure 2.20 (a), the I-V curve shows a clear nonlinear response, which is a typical tunneling barrier characteristic and also indicates that AlOx sputtering process

through shadow mask works properly following the designed fabrication strategy. In Figure 2.20 (b), the magnetoresistance as a function of perpendicular magnetic field shows a peak at zero magnetic field, rather a switching between “High” and “Low” resistance states. This is due to the nature of MTJ with one FM electrode with perpendicular magnetization and the other with in-plane magnetization, it is difficult to achieve parallel or anti-parallel configurations, which requires a large external magnetic field.

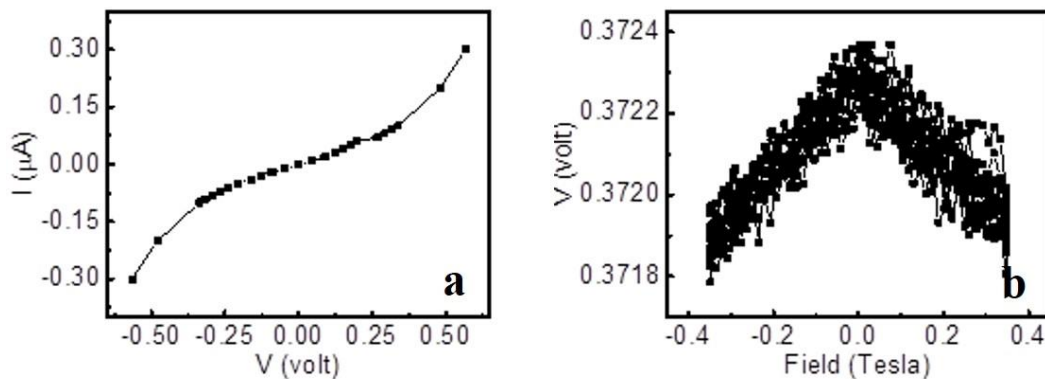


Figure 2.20 (a) The I-V curve for AlOx-based MTJs. (b) The magnetoresistance as a function of the perpendicular magnetic field.

2.3.3 Magnetoelectric Devices

2.3.3.1 ME device characterization

Using the shadow mask technique, we fabricated $[\text{Co}/\text{Pt}]_n$ film in Hall bar structure on top of Cr_2O_3 sample as illustrated in Figure 1.4 While thick Cr_2O_3 crystals ($500 \mu\text{m}$) show excellent insulating property with resistivity in the range of 10-100 $\text{T}\Omega\text{cm}$, the expitaxy Cr_2O_3 films ($300 \text{ nm} \sim 500 \text{ nm}$) are still pretty leaky [5]. The

largest contacts ($500 \times 500 \mu\text{m}^2$) have shown the strong shunting effect, but the smallest contacts ($50 \times 50 \mu\text{m}^2$) have negligible leakage as shown in Figure 2.21. Even for the same contact area, there are strong variation in the resistance through the Cr_2O_3 , suggesting that the quality of Cr_2O_3 remain to be improved.

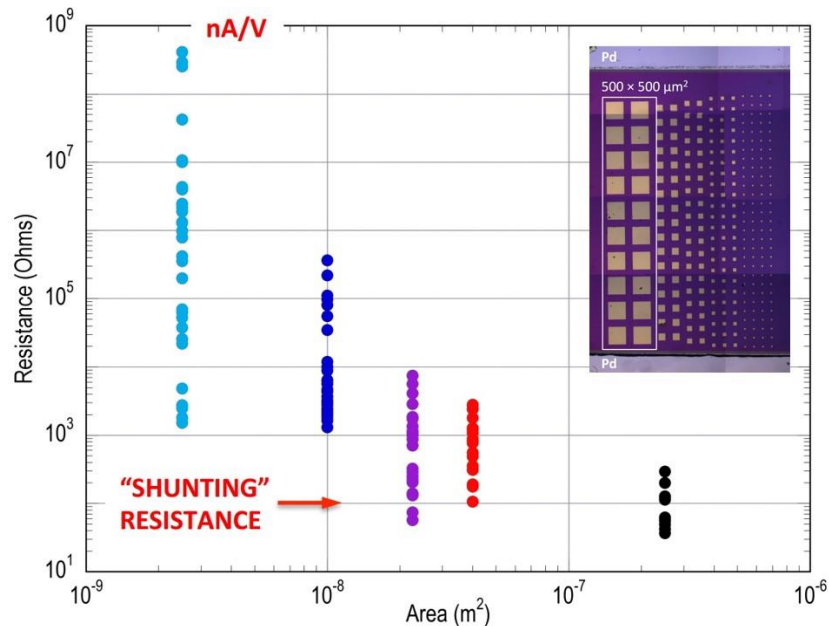


Figure 2.21 The electrical characterization of epitaxial Cr_2O_3 film. The resistivity measurement has been performed between Pd bottom electrode and patterned Cr/Au top electrodes with various contact sizes, which is shown in the inset.

In order to overcome the leakage in Cr_2O_3 thin films, two methods have been developed to eliminate the leaking current: (1) reduction of contact pad size down to $180 \times 180 \mu\text{m}^2$; (2) insertion of another insulating HfO_2 layer between Cr_2O_3 film and top Ta/Au contacts. As shown in Figure 2.22, the use of HfO_2 insertion layer can eliminate the leakage issue of Cr_2O_3 films.

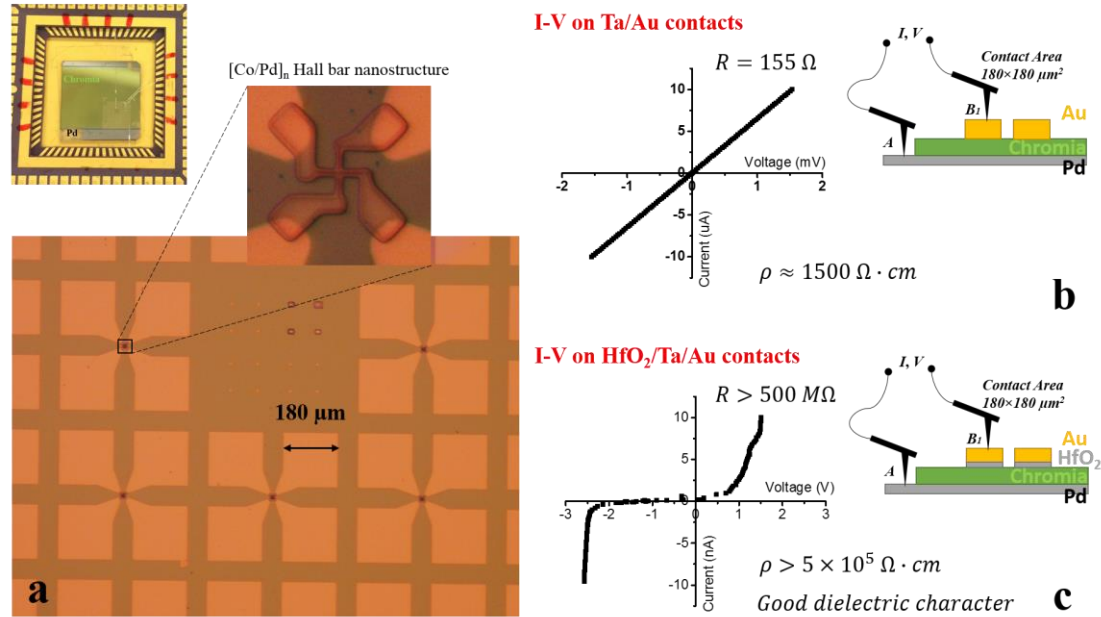


Figure 2.22 The current-voltage characteristics obtained from electrical measurements. (a) The images of contacts on top of Cr_2O_3 thin film. The current-voltage characteristics on both (b) Ta/Au contacts and (c) $\text{HfO}_2/\text{Ta/Au}$ contacts.

Very recently, our collaborators, M. Street *et al.* at Nebraska Lincoln, have successfully developed a pulsed laser deposition (PLD) based method to grow high quality Cr_2O_3 films. Meanwhile, by changing the buffer layer Pt to V_2O_3 , M. Street *et al.* have also demonstrated significant improvement in Cr_2O_3 films.

2.3.3.2 Nanofabrication of ME Devices

All the Cr_2O_3 -based ME devices have been prepared in UD Nanofabrication Facility by using Vistec EBPG5200ES E-beam writer in E-beam lithography process. In order to adapt the Hall bar shadow mask design into this new E-beam facility, a set of newly designed alignment markers has been applied in the following Cr_2O_3 samples

fabrication. The design is illustrated in Figure 2.23 (a). The alignment markers consist of the bottom markers “①”, which include four identical 11×11 square dot arrays (Figure 2.23 (b)) that help locate sample coordinates under the E-beam writer. In Figure 2.23 (c), there are other square dot markers placed at each corner of the sample, which are used in the rotational adjustment as well as vertical and horizontal movements. All the markers are able to be recognized by the E-beam writer software, and the alignment process is automatically controlled.

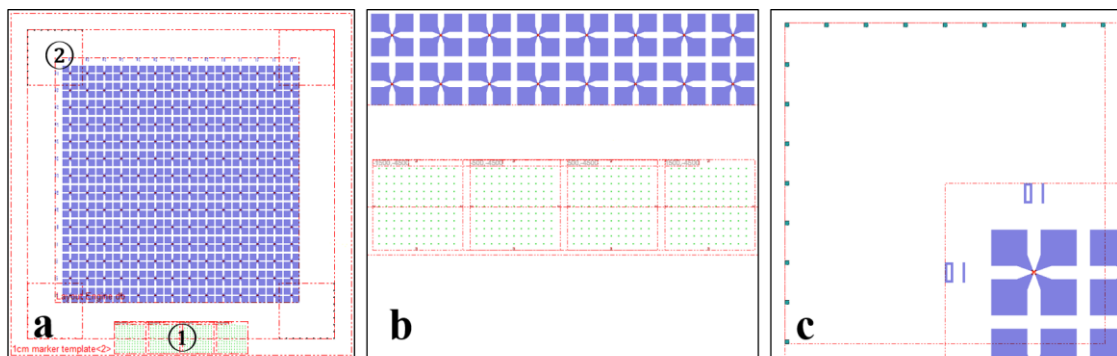


Figure 2.23 E-beam alignment marks design. (a) Two sets of markers with different functionalities have been included in the shadow mask design (①: Sample bottom location markers; ②: Corner alignment markers). (b) The location markers. (c) The alignment markers at corners.

The E-beam writer alignment markers was prepared in the first step of E-beam writing process with the standard recipe of E-beam resists shadow mask 85 nm CSAR.04/235 nm LOR 3A. The metallization procedure used the standard E-beam evaporation recipe. The alignment markers were made of 10 nm Ta/80 nm Au.

The $180 \times 180 \mu\text{m}^2$ contacts were fabricated by magnetron sputtering and lift-off method, right after the second step of E-beam writing procedure. In order to

eliminate the leakage problem in thin Cr_2O_3 film, 80 nm HfO_2 /10 nm Ta/80 nm Au is chosen as the contact recipe. The shadow mask is the standard recipe of 85 nm CSAR.04/235 nm LOR 3A.

The final step of E-beam writing was to create the shadow mask for the last step of $[\text{Co}/\text{Pd}]_n$ multilayer film sputtering deposition. In this step, a 100 nm CSAR 09/300 nm LOR 5A shadow mask with approximately 1 μm undercut. The $[\text{Co}/\text{Pd}]_n$ Hall bar structure fabrication has been discussed in Section 2.3.1.

2.3.3.3 Characterization of ME Devices

The ME devices has been characterized by the AHE measurement, which is shown in Figure 2.24. $\text{Pd}(0.5\text{nm})/(\text{Co}(0.3\text{nm})/\text{Pd}(0.9\text{nm}))_6$ film has been deposited on both Cr_2O_3 thin film and Si wafer, as illustrated in Figure 2.24 (a) and (b), respectively. The split-loop characteristic of $[\text{Co}/\text{Pd}]_n$ film on Cr_2O_3 is indicative of a multi-domain state of Cr_2O_3 , leading to distributed exchange coupling strengths. By contrast, a symmetric and sharp switching hysteresis is shown in sample grown on Si substrate (Figure 2.24 (b)), which is expected from an unpinned $[\text{Co}/\text{Pd}]_n$ film. The test Cr_2O_3 sample and the control Si wafer sample reveal the solid evidence of exchange coupling happens at the boundary between Cr_2O_3 and $[\text{Co}/\text{Pd}]_n$ PMA structure.

As shown in Figure 2.24 (c), in addition to demonstration of exchange coupling, the preliminary isothermal switching test has also been performed on this $[\text{Co}/\text{Pd}]_n/\text{Cr}_2\text{O}_3$ test sample. The positive and negative electrical fields (applied voltages ± 0.1 V) were applied across the 300 nm Cr_2O_3 , and a constant magnetic field of 3000 Oe was simultaneously applied. Although the field product here is not sufficient, limited by our experimental setup, to achieve the complete isothermal

exchange bias switching between two single domain states. It is still apparent that the presence of positive and negative applied voltage could modify the AFM domain structure resulting in two different hysteresis loops.

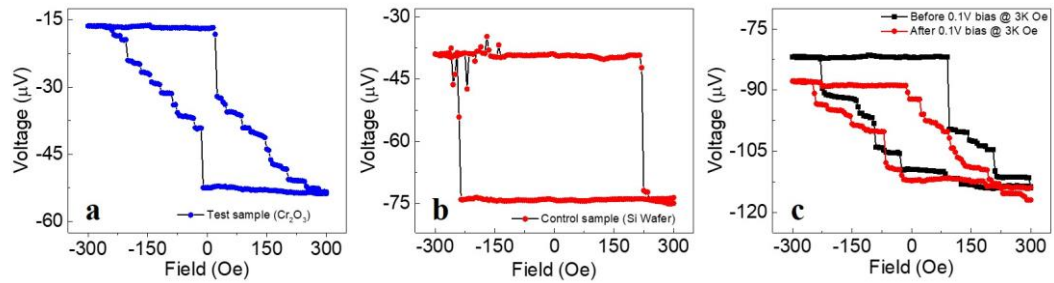


Figure 2.24 The AHE of $[\text{Co}/\text{Pd}]_n$ film on top of (a) Cr_2O_3 thin film, (b) Si wafer and (c) isothermal switching test result at a 3000 Oe external magnetic field.

REFERENCES

- [1] G. J. Dolan, *Appl. Phys. Lett.* **31**, 337 (1977).
- [2] X. J. Wang, H. Zou, L. E. Ocola, R. Divan, and Y. Ji, *J. Appl. Phys.* **105**, 093907 (2009).
- [3] H. Zou, X. J. Wang, and Y. Ji, *J. Vac. Sci. Technol. B.* **28**, 1314 (2010).
- [4] S. Chen, C. Qin, and Y. Ji, *Appl. Phys. Lett.* **105**, 082402 (2014).
- [5] C. P. Kwan, R. Chen, U. Singisetti, and J. P. Bird, *Appl. Phys. Lett.* **106**, 112901 (2015).

Chapter 3

SPIN HALL EFFECT IN 3D LIGHT TRANSITION METALS

3.1 Introduction

To date, most studies have focused on the $4d$ and $5d$ transition metals, since the spin orbit coupling strength of individual atoms scales with atomic number as Z^4 [1-2]. Large spin Hall angles have been observed in heavy metals such as Pt [3-4], β -Ta [5], β -W [6-7], Hf [8-9], etc. Considerable efforts have also been focused on enhancing the charge-to-spin conversion efficiency by introducing external scattering mechanisms in the heavy metals, which has led to the observation of giant spin Hall angles in CuBi alloys [10], AuW [11], CuIr [12], CuPd [13], etc. Due to their relatively low Z , $3d$ light transition metals are often neglected in the search for materials with large spin Hall angle. Very recently, Du et al. observed significant spin pumping-driven inverse SHE (ISHE) voltages in YIG/Cr bilayers, and obtained a spin Hall angle as large as -0.051 ± 0.005 [14]. Qu et al. have also demonstrated sizeable ISHE in Cr by using a thermal spin injection method [15].

In this chapter, I will show the large spin orbit torques (SOTs) in vanadium films which has been characterized by using the optical spin torque magnetometer based on polar MOKE [16-17]. A large spin Hall angle of -0.071 ± 0.003 has been found in V/Co₄₀Fe₄₀B₂₀ bilayers [18]. As comparison, the spin Hall angles found in Ta/Co₄₀Fe₄₀B₂₀ and Pt/Co₄₀Fe₄₀B₂₀ by using the same MOKE setup are -0.139 ± 0.003 and 0.076 ± 0.007 , respectively. The large spin Hall angle has been found to correlate

to the structure of the V layer, which consists of body centered tetragonal (*bct*) and body centered cubic (*bcc*) phases.

3.2 Large Spin Hall Angle in Vanadium Film

3.2.1 Sample Fabrication and Characterization

All films were deposited by magnetron sputtering system on thermally oxidized silicon wafers. All samples of $\parallel\text{V}(x \text{ nm})/\text{CoFeB}(2 \text{ nm})/\text{SiO}_2(5 \text{ nm})$ (“ \parallel ” denotes the substrate end, $x = 2, 5, 10, 30, 50 \text{ nm}$) were grown at room temperature with the base pressure lower than 3×10^{-7} Torr and the working pressure of 4.5×10^{-3} Torr, respectively. The nominal composition of CoFeB is of 40:40:20 atomic ratio. A 5 nm SiO_2 as the capping layer was deposited through radio frequency (RF) magnetron sputtering. The sputtering rates and power were 0.067 nm/s and 18W for CoFeB and 0.070 nm/s and 24W for V. The control group sample V(30 nm)/CoFeB(2 nm) was prepared under 400°C with a lower base pressure of 8×10^{-8} Torr.

The sample structural characterizations are shown in Figure 3.1. The X-ray diffraction (XRD) pattern in Figure 3.1 (a) indicates different lattice parameters and grain sizes of V(30 nm)/CoFeB(2 nm) test sample and control samples, which is denoted as the black and red curves, respectively. The 30 nm V test sample shows a broad and asymmetric diffraction peak with the center located at 40.3° whereas the main diffraction peak of the control sample is at 42.1° . As shown in Figure 3.1 (b), the resistivities of test samples, all grown at room temperature, vary from $290 \mu\Omega\cdot\text{cm}$ to $220 \mu\Omega\cdot\text{cm}$ as the V thickness changes from 2 to 50 nm. On the other hand, the control samples, grown at 400°C , show much reduced resistivity. In Figure 3.1 (c) and (d), the HR-TEM images show the clear structural difference of these two samples which is

consistent with the fitting result from XRD patterns. The average grain size of the 30 nm V test sample is about 5 nm and the interlayer spacing varies from 2.20 Å to 2.31 Å at different locations. The control sample has a larger grain size above 10 nm, and the spacing is dominantly 2.16 Å.

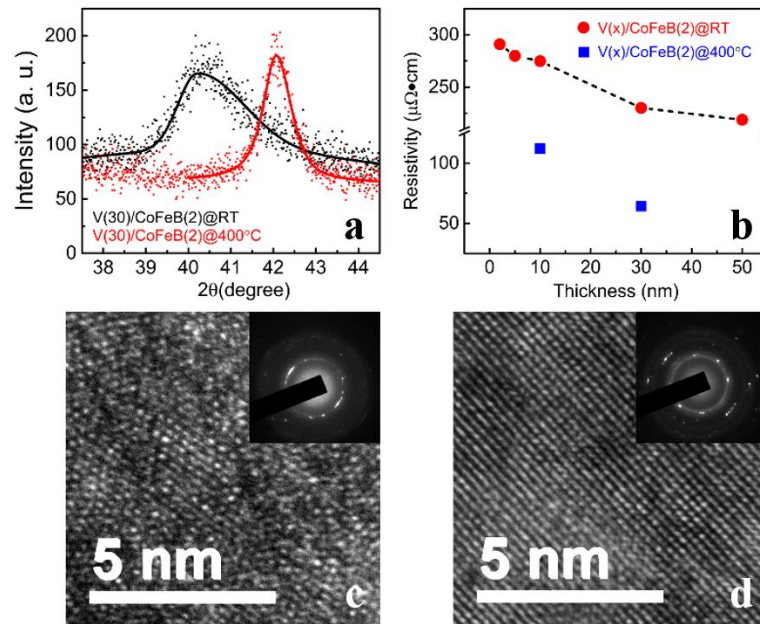


Figure 3.1 Samples characterizations of $V(x \text{ nm})/\text{CoFeB}(2 \text{ nm})$. (a) X-ray diffraction pattern of samples $V(30 \text{ nm})/\text{CoFeB}(2 \text{ nm})$ grown at room temperature (black) and 400°C (red). (b) The total resistivity of test samples (red) and control sample (blue) as a function of V thickness. (c) and (d) HR-TEM images of $V(30 \text{ nm})/\text{CoFeB}(2 \text{ nm})$ test and control samples. The insets are the corresponding electron diffraction patterns.

To better characterize the V structure in our samples, we performed fast Fourier transform (FFT) analysis based on the high resolution transmission electron microscopy (HRTEM) images in Figure 3.2. The structure from the grains surrounded

by red line in Figure 3.2 (a) can be best indexed by a [111] zone axis of a *bct* V, whereas the grains surrounded by white curves can be best described by a *bcc* V. These analyses suggest the sputter-grown V films at room temperature are a mixture of *bct* and *bcc* structures, which may also explain the broad XRD peak in Figure 3.1 (a). This is similar to β -Ta films, which have tetragonal nanocrystalline phase in an amorphous matrix [19], while α -Ta films have *bcc* structure. In sharp contrast, as shown in Figure 3.2 (b), the control sample F grown at 400°C shows dominant *bcc* V structure from the FFT analyses.

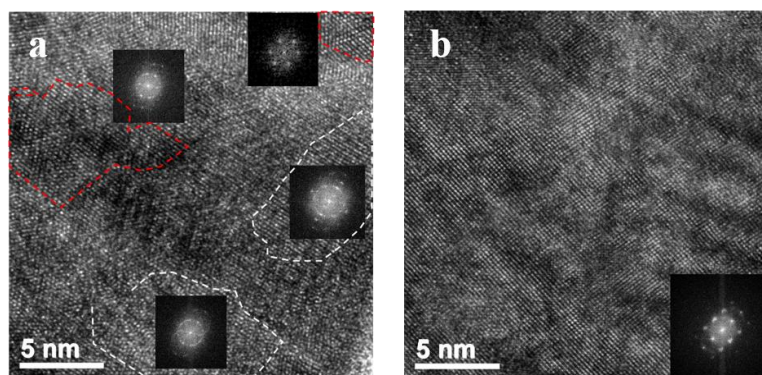


Figure 3.2 Fast Fourier transformation analysis of vanadium's TEM images. (a) The test sample, which has been prepared at room temperature, shows both *bct* (red) and *bcc* (white) phases. (b) The control sample FFT image is dominated by *bcc* phase.

To further understand the microstructures, we have also performed analyses on a series of V(30 nm)/CoFeB(2 nm) samples which were prepared under different sputtering conditions. The fabrication parameters are listed in Table 3.1. The XRD spectrums of V(30 nm)/CoFeB(2 nm) samples are shown in Figure 3.3. The XRD peaks shift from 42.1° (sample (a)) to 38.3° (sample (d)). Sample (a) was grown under

base pressure of 8.0×10^{-8} Torr with the substrate temperature of 400°C s, which has the smallest lattice constant comparing with other three samples. However, if samples are grown without heating the substrate, the film lattice constant expands, and the grain size shrinks, which is indicated by the XRD spectrum of sample (b). Furthermore, with the decreasing magnetron sputtering base pressure down to 5.0×10^{-6} Torr, as shown in Figure 3.1 (c) and (d), the XRD peaks are continuing shift to low angle region and becoming asymmetric, which means the lattice keeps expanding and the structure becomes more distorted.

Table 3.1 The magnetron sputtering parameters of the V(30 nm)/CoFeB(2 nm) samples. (RT represents “room temperature”)

Sample #	Magnetron Sputtering Conditions	
	Base Pressure (Torr)	Substrate Temperature ($^{\circ}\text{C}$)
a	8.0×10^{-8}	400
b	8.0×10^{-8}	RT
c	3.0×10^{-7}	RT
d	5.0×10^{-6}	RT

In the following, we will discuss the connection between spin orbit effect of V/CoFeB bilayer and V film structures based on the SOT measurement of these series samples and structural analysis.

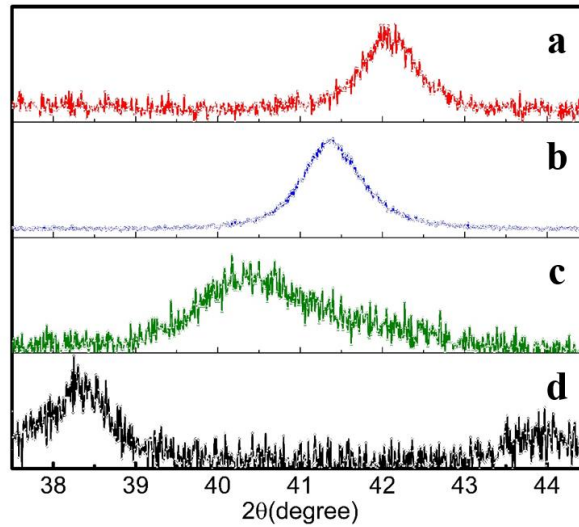


Figure 3.3 The XRD spectrums of V films with different sputtering conditions of samples (a) to (b).

3.2.2 High Frequency Measurements

The investigation of high frequency magnetic dynamics is a powerful method to characterize magnetic materials. The standard way to perform a ferromagnetic resonance (FMR) experiment is to utilize an extra oscillating field to drive the magnetic moment and induce the magnetic procession. In this study of V/CoFeB heterostructure, FMR measurement can be used to extract the effective magnetization $\mu_0 M_{\text{eff}}$, Gilbert damping factor σ , inhomogeneous broadening ΔH_0 et al. In addition, the V thickness dependent damping enhancement measurement can also be used to investigate the spin mixing conductance at V/CoFeB interface, which will be discussed in the following spin pumping measurement section.

3.2.2.1 FMR Measurement

The setup of FMR measurement is shown in Figure 3.4. A typical coplanar waveguide (CPW) was introduced to create the oscillation magnetic field. A standard 50Ω CPW is patterned on an alumina substrate with the geometry $s = 50 \mu\text{m}$ and $g = 33 \mu\text{m}$, which is consisted of 10 nm Ta/600 nm Cu/200 nm Au. The FMR samples are flip-chipped on CPW.

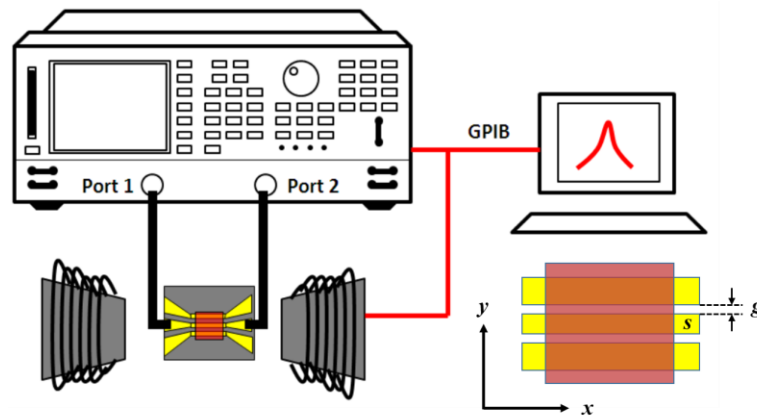


Figure 3.4 The schematic illustration of FMR measurement based on CPW configuration.

A vector network analyzer (VNA) is used as both microwave source and S -parameter analyzer. The microwave is sent out from port 1 and fed into CPW. The injected microwave current in CPW will induce a RF magnetic field h_{rf} which works as driving field. Both reflection S_{11} and transmission S_{21} parameters are measured based on power detected on port 1 and port 2. We perform external magnetic field H_0 scan at fixed microwave frequency. The relative magnetic susceptibility $\chi(H_0)$ could be retrieved from the measured $S_{21}(H_0)$ from the following equation [20]

$$\Delta\chi_{\text{eff}} = \chi[H_0] - \chi[H_{\text{ref}}] = \frac{-jc}{\omega d \delta} \log \frac{S_{21}[H_0]}{S_{21}[H_{\text{ref}}]} \quad (3.1)$$

where $S_{21}[H_{\text{ref}}]$ is chosen as the reference signal to exclude the background signal, H_{ref} is usually chosen at high field that saturates sample magnetization. In practical measurement, an extra phase parameter induced by the entire loss in the RF circuit should be added to Equation 3.1 to adjust the shape. The parameters of $c/\omega d \delta$ could be omitted since the absolute magnitude of $\Delta\chi_{\text{eff}}$ won't change the fitting result.

As shown in Figure 3.4, the magnetization is aligned in x -direction by the external direct current (DC) magnetic field generated by a water cooled electromagnet. (The maximum 1000 Oe has been used in the series samples of V/CoFeB). With the driving field h_{rf} along y -axis, the magnetization starts to precess. The resonance condition can be described by Kittel equation [21]

$$\omega_{\text{res}}^2 = \gamma^2 [H_0 + (N_y - N_x)M_s] [H_0 + (N_z - N_x)M_s] \quad (3.2)$$

where N_x, N_y, N_z are the demagnetization factors of magnetic materials, and $N_x + N_y + N_z = 1$. The related magnetic susceptibility can be written as

$$\chi = \frac{\omega_m(\omega_z + i\alpha\omega)}{(\omega_y + i\alpha\omega)(\omega_z + i\alpha\omega) - \omega^2} \quad (3.3)$$

where $\omega_m = \gamma M_s$, $\omega_0 = \gamma H_0$, $\omega_y = \omega_0 + (N_y - N_x)\omega_m$, $\omega_z = \omega_0 + (N_z - N_x)\omega_m$. For in-plane magnetization, such as V/CoFeB films studied here, $N_z = 1$ and $N_x = N_y = 0$. On the other hand, we should also consider both the in-plane uniaxial anisotropy field $\mathbf{H}_{\parallel} = (2K_{\parallel}/M_s) \cdot M_x \cdot \mathbf{e}_x$ and the out-of-plane anisotropy field $\mathbf{H}_{\perp} = (2K_{\perp}/M_s) \cdot M_z \cdot \mathbf{e}_z$, where M_x and M_y represent the x and y components of the magnetization \mathbf{M} .

Thereafter, we include two fields \mathbf{H}_{\parallel} (x -axis) and \mathbf{H}_{\perp} (z -axis) into the demagnetization factors, and we rewrite the factors as $N_x' = N_x - (2K_{\parallel}/M_s^2)$, $N_z' = N_z - (2K_{\perp}/M_s^2)$ and $N_y' = N_y$, the Kittel equation is simplified as

$$\omega_{\text{res}} = \gamma \sqrt{H_0 \left[H_0 - \frac{2K_{\perp}}{M_s} + M_s \right]} \quad (3.4)$$

The susceptibility χ is a complex magnetic value with both real and image parts

$$\chi = \frac{\gamma M_s (\gamma H_0 - \gamma \frac{2K_{\perp}}{M_s} + \gamma M_s + i\alpha\omega)}{(\gamma H_0 + i\alpha\omega)(\gamma H_0 - \gamma \frac{2K_{\perp}}{M_s} + \gamma M_s + i\alpha\omega) - \omega^2} \quad (3.5)$$

The susceptibility is used to fit measured susceptibility (Equation 3.1). The typical susceptibility result is shown in Figure 3.5.

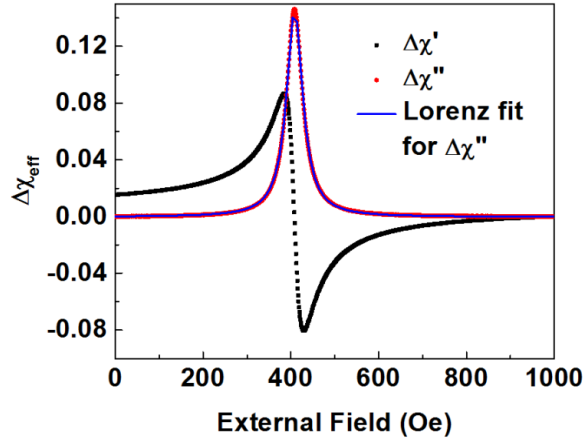


Figure 3.5 A typical FMR spectrum which is fitted based on Equation 3.5.

The image part of the magnetic susceptibility χ'' is fitted with Lorentzian function through the Levenberg-Marquardt method. The resonance field H_0 and the full width at half maximum (FWHM) ΔH could be extracted. Based on Kittel equation (Equation 3.4), the effective magnetization $\mu_0 M_{\text{eff}}$, and in-plane anisotropy field H_a can be determined. Since the linewidth response (Equation 3.6) is related with a combined inhomogeneous broadening ΔH_0 and Gilbert damping α [22-23]

$$\Delta H = \Delta H_0 + \frac{4\pi\alpha f}{|\gamma|} \quad (3.6)$$

we can extract both ΔH_0 and α from the frequency-dependence of the FMR linewidth.

3.2.2.2 Determination of Spin Diffusion Length

The FMR fitting results are shown in Figure 3.6. In Figure 3.6 (a), the effective magnetization $\mu_0 M_{\text{eff}} = \mu_0 M_s - 2K_{\perp}/\mu_0 M_s$ indicates $\mu_0 M_{\text{eff}}$ could vary if samples have different anisotropy constant. The perpendicular anisotropy arises from the interfacial surface anisotropy of CoFeB which could be affected by the V thickness. The Gilbert damping constant α as a function of V thickness d_V is plotted in Figure 3.6 (b), increases as the V thickness increasing, and gets saturated above $d_V = 30$ nm. The Gilbert damping enhancement $\alpha'(d_V) = \alpha(d_V) - \alpha(d_V = 0)$ can be described as [24-25]

$$\frac{\alpha'(d_V)}{\alpha'(d_V=\infty)} = \frac{1+\varepsilon^{-1/2}}{1+\varepsilon^{-1/2}\tanh(d_V/\lambda_{\text{sf}})^{-1}} \quad (3.7)$$

where $\varepsilon = \tau_{\text{el}}/\tau_{\text{sf}}$ denotes the spin flip probability in each spin dependent scattering even, τ_{el} is the elastic scattering time, $1/\tau_{\text{sf}}$ is the spin flip rate. Based on this equation, the fitting result is shown as the red curve in Figure 3.6 (b). The extracted spin diffusion length $\lambda_{\text{sf}} = 16.3 \pm 0.7$ nm, which is comparable to the published value of $\lambda_{\text{sf}} = 14.9 \pm 2.4$ nm [14].

The inhomogeneous broadening is defined as the zero-frequency intercept of FMR linewidth which is related with film quality. From Figure 3.6 (c), we could also confirm there is film quality fluctuations in these five samples with different V thickness.

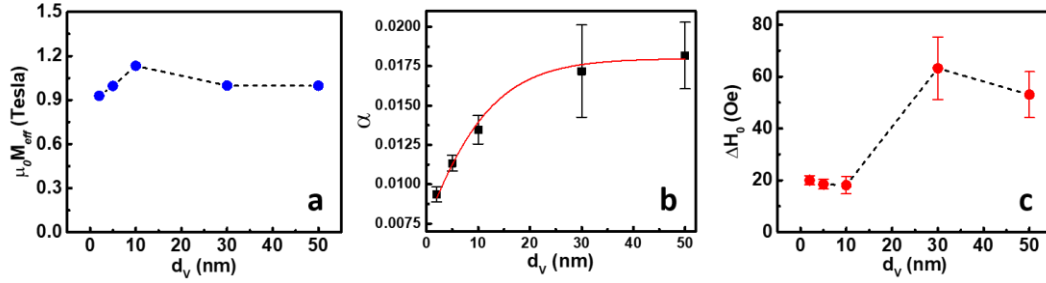


Figure 3.6 The FMR fitting results of V/CoFeB samples. (a) the effective demagnetization field $\mu_0 M_{\text{eff}}$, (b) the Gilbert damping factor α , and the inhomogeneous broadening ΔH_0 .

3.2.3 Spin Orbit Torques in V/CoFeB system

We investigated the SOTs in V/CoFeB systems. The SOTs are measured with optical methods which we discuss first. The light that is reflected off a magnetic surface would have its polarization direction modified which depends on the orientation of the surface magnetization. This optical response, which was discovered by John Kerr in 1877 [21] is known as magneto-optical Kerr effect (MOKE). MOKE has been widely used in the study of magnetism in thin films [26-28]. As shown in Figure 3.7, there are three configurations of MOKE: (a) polar, (b) transverse and (c) longitudinal. In this section, the polar MOKE SOT measurement technique is closely based on the work done by X. Fan et al. [16-17].

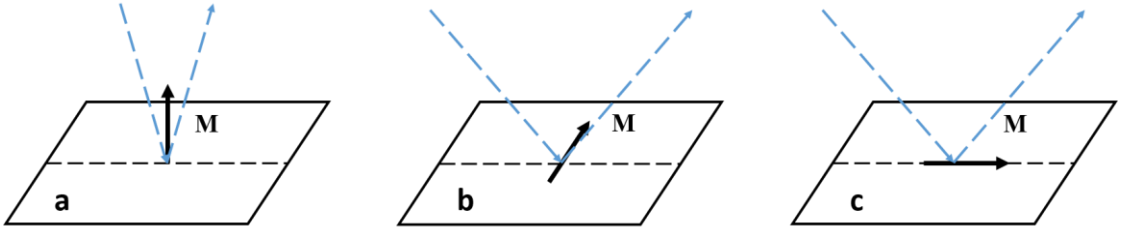


Figure 3.7 Three configurations in MOKE measurements: (a) polar, (b) transverse, (c) longitudinal.

3.2.3.1 Spin Orbit Torque Measurement with Polar MOKE

The current induced magnetization reorientation can be described by the Landau-Lifshitz-Gilbert-Slonczewski equation

$$\frac{d\mathbf{m}}{dt} = -\mu_0\gamma\mathbf{m} \times \mathbf{H}_{\text{eff}} + \alpha\mathbf{m} \times \frac{d\mathbf{m}}{dt} + \tau_{\text{SOT}}\mathbf{m} \times (\boldsymbol{\sigma} \times \mathbf{m}) - \tau_{\text{SOF}}\mathbf{m} \times \boldsymbol{\sigma} \quad (3.8)$$

where \mathbf{m} is the unit vector of magnetic moment, \mathbf{H}_{eff} is the total effective field: $\mathbf{H}_{\text{eff}} = \mathbf{H}_{\text{ext}} + \mathbf{H}_{\text{an}} + \mathbf{H}_{\text{Oe}}$, including the external field, anisotropy field and current induced Oersted field, respectively, α is the phenomenology Gilbert damping factor, $\boldsymbol{\sigma}$ is the spin polarization, μ_0 is the vacuum permeability, γ is the gyromagnetic ratio. Here we define the damping like torque $\tau_{\text{SOT}} = \mu_0\gamma \cdot h_{\text{SOT}}$ and the field like torque $\tau_{\text{SOF}} = \mu_0\gamma \cdot h_{\text{SOF}}$.

For a NM/FM bilayer with an in-plane magnetization along the x -axis as shown in Figure 3.8, the effective field of the damping-like torque \mathbf{h}_{SOT} is determined by $\boldsymbol{\sigma} \times \mathbf{m}$, which is along the z -axis. The magnetization will be tilted out-of-plane to introduce \mathbf{m}_z component that can be probed by polar MOKE. The effective field of the field-like torque \mathbf{h}_{SOF} has the same direction as the spin polarization direction $\boldsymbol{\sigma}$, which is along the y -axis and rotates the magnetization in the x - y sample plane.

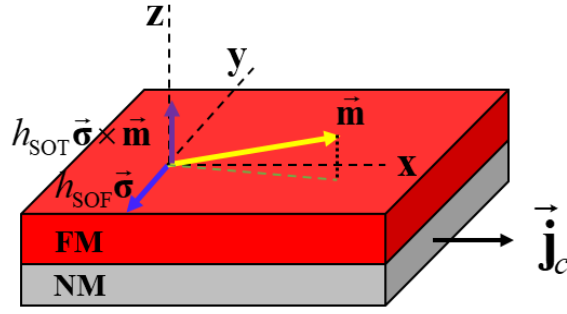


Figure 3.8 The schematic illustration of current induced SOTs in NM/FM bilayer with in-plane magnetization.

The entire setup is shown in Figure 3.10. All the V/CoFeB samples were patterned into $50 \mu\text{m} \times 50 \mu\text{m}$ strips through conventional photolithograph method. The laser beam has a $2 \mu\text{m}$ diameter. In order to further enhance the signal-to-noise ratio, the lock-in technique is used by measuring the MOKE response due to an AC current through the sample. In addition to the damping-like torque h_{SOT} that tilts the magnetization out-of-plane and creates m_z component, the vertical component of the Oersted field h_{Oe} generated by the charge current also induces m_z . Therefore, a signal of the change of magnetization Δm_z in the CoFeB layer probed by polar MOKE includes both contributions from h_{SOT} and h_{Oe} components.

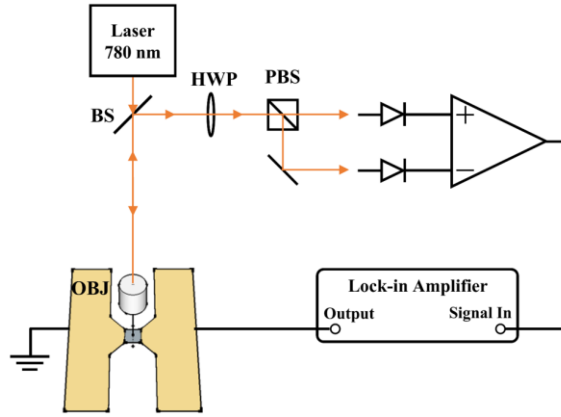


Figure 3.9 The schematic illustration of polar MOKE spin torque magnetometer setup (BS, beamsplitter; HWP, half-wave plate; OBJ, objective; PBS, polarizing beamsplitter).

Due to symmetry requirement, the charge current \mathbf{j}_c , spin current \mathbf{Q}_σ , and spin polarization σ are mutually orthogonal following $\mathbf{Q}_\sigma = (\hbar/2e)\theta_{SH}(\mathbf{j}_c \times \sigma)$, regardless the effect is from the spin Hall effect (SHE) or Rashba effect. Therefore, the charge current along the x -axis always generates the spin polarization σ in y direction. We applied an external magnetic field along x direction and perform field scan on CoFeB(2 nm)/V(5 nm) sample. The typical MOKE measurement result is shown in Figure 3.10. As discussed in the previous paragraph, Δm_z is proportional to $\mathbf{h}_{SOT} + \mathbf{h}_{Oe}$. More specifically $\Delta m_z \propto (h_{SOT} + h_{Oe}) / (H_{ex} + M_s)$, where M_s is the demagnetization field since the magnetization is tilted out of the plane. The typical value for M_s is larger than 1 T which is far greater than the applied magnetic field H_{ex} . Therefore, the polar MOKE signal is almost independent of H_{ex} but switches sign since \mathbf{h}_{SOT} is asymmetric with magnetization direction, i.e. $\mathbf{h}_{SOT} = h_{SOT}(\sigma \times \mathbf{m})$. The MOKE signal also contains the contribution from h_{Oe} , which however, does not change with magnetization since the current is always the same. Therefore, by subtracting and adding the signals

following $V[+H_{\text{ex}}] \pm V[-H_{\text{ex}}]$, we can determine the contribution from h_{SOT} or h_{Oe} , respectively.

It is difficult to determine the quantitative relationship between the MOKE signal and m_z . However, we can perform simple calibration procedure which we discuss next.

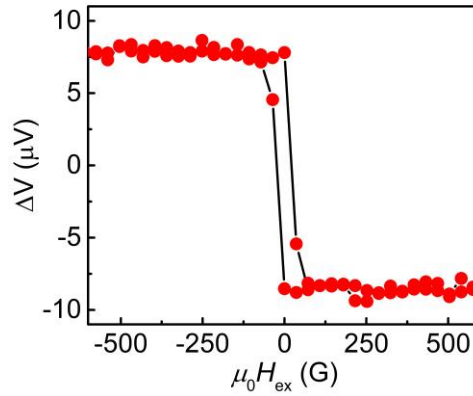


Figure 3.10 A typical polar MOKE measurement magnetic field scan result of V(5 nm)/CoFeB(2 nm) sample.

3.2.3.2 Determination of Damping-Like Torque

As discussed above, the MOKE voltage signal consists of SOT term and out-of-plane Oersted field term which have different symmetries with respect to the CoFeB magnetization m [16-17]. Therefore, these two terms can be separately extracted from

$$\begin{cases} \Delta V_{\text{SOT}} = \frac{V[+H_{\text{ex}}] - V[-H_{\text{ex}}]}{2} \\ \Delta V_{\text{Offset}} = \frac{V[+H_{\text{ex}}] + V[-H_{\text{ex}}]}{2} \end{cases} \quad (3.9)$$

where ΔV_{SOT} represents the damping-like torque, and ΔV_{Offset} indicates the out-of-plane Oersted field.

Except this m -dependent difference, there is also a spatial distribution difference between the two terms. SOT has a uniform distribution along sample transverse to the current direction. Along the same direction, the out-of-plane Oersted field is antisymmetric with respect to the center of the sample. In the experiment, a transverse direction line scan is used to probe the spatial distributions. ΔV_{SOT} and ΔV_{Offset} are extracted using Equation 3.9 at every single point. The final two terms are plotted in Figure 3.11 (a) and (b).

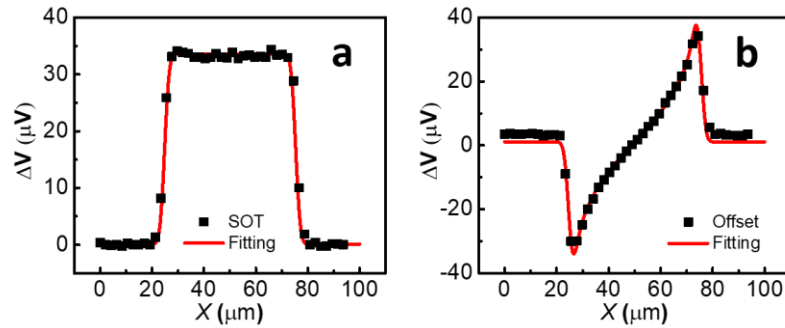


Figure 3.11 (a) The typical SOT result of V/CoFeB and (b) the effective Oersted field induced by the current.

Since the actual magnitude of Oersted field can be calculated through the equation

$$h_{\text{Oe}} = \frac{I_C}{2\pi w} \ln \frac{w-y}{y} \quad (3.10)$$

where I_C is the total charge current through the sample cross section, w is the sample width of $50 \mu\text{m}$. By comparing this calculated Oersted field with the measured data,

the MOKE signal can be calibrated and the effective SOT can be determined. The detailed analytical expressions of ΔV_{SOT} and ΔV_{Offset} have been derived as [16]

$$\Delta V_{\text{SOT}}(y, z) = \eta \frac{1}{2\pi r^2} \iint dy' dz' e^{-\frac{(y-y')^2 + (z-z')^2}{r^2}} \frac{h_{\text{SOT}}(y')}{H_{\text{ex}} + M_{\text{eff}}} \quad (3.11)$$

$$\Delta V_{\text{Offset}}(y, z) = \eta \frac{1}{2\pi r^2} \iint dy' dz' e^{-\frac{(y-y')^2 + (z-z')^2}{r^2}} \frac{h_{\text{Oe}}(y')}{H_{\text{ex}} + M_{\text{eff}}} \quad (3.12)$$

where the laser spot dimension and the Gaussian distribution of the laser beam have been taken into account.

In this study, we use spin Hall angle θ_{SH} to characterize the current conversion efficiency from charge current to spin current. The spin Hall angle is defined as [16]

$$\theta_{\text{SH}} = \frac{h_{\text{SOT}}}{I_{\text{C}}/w} \frac{2e}{\hbar} \frac{\mu_0 M_s t_{\text{NM}} t_{\text{FM}}}{\xi} \quad (3.13)$$

where h_{SOT} can be extracted from the self-calibrated MOKE measurement, $\mu_0 M_s = 1.6$ Tesla which was measured from a 40 nm CoFeB film, t_{NM} equals 2, 5, 10, 30, 50 nm, and $t_{\text{FM}} = 2$ nm. ξ represents the ratio of charge current distribution in V layer.

In order to determine ξ in V/CoFeB bilayer structure, we have performed additional resistivity measurement as the function of V thickness in samples of V(x nm)/CoFeB(2 nm). The results are shown in Figure 3.12. Based on parallel resistor model, we extract V film conductivity from the slope and the conductivity of 2 nm CoFeB film from the intercept. This linear fitting method has been used in the analysis of resistivity of thin films [8, 29]. The resistivity of 2 nm CoFeB film is one order larger than that of V, $\rho_{\text{V}} = 213 \mu\Omega \cdot \text{cm}$ and $\rho_{\text{CoFeB}} = 2862 \mu\Omega \cdot \text{cm}$. The resistivity of CoFeB thin film depends strongly on the underlayers and deposition conditions. By assuming all current passing through V ($\xi = 1$), we are at least able to set the lower bound of the effective spin Hall angle.

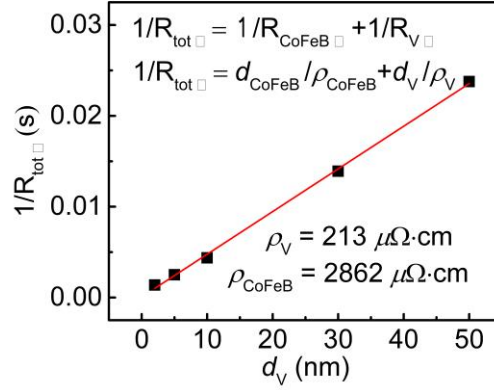


Figure 3.12 Conductivity of the entire V(x nm)/CoFeB(2 nm) stack as the function of V thickness.

The effective spin Hall angle has been summarized in Figure 3.13. The spin Hall angle θ_{SH} increases with the V layer thickness and approaches saturation as the V thickness goes above the spin diffusion length in V ($t_V > 16.3$ nm). In order to account for the spin transparency and interface coupling, we use the modified spin transport model to extract the spin Hall angle $\theta_{SH}(\infty)$ [25], the V thickness dependence of the measured spin Hall angle $\theta_m(d_V)$ becomes

$$\frac{\theta_m(d_V)}{\theta_{SH}(\infty)} = \frac{\cosh(d_V/\lambda_{sf}) - 1}{\cosh(d_V/\lambda_{sf}) + R} \quad (3.14)$$

and

$$R = \frac{G_V}{2G_{\uparrow\downarrow}} \sinh\left(\frac{d_V}{\lambda_{sf}}\right) \quad (3.15)$$

The extracted spin Hall angle is $\theta_{SH} = -0.071 \pm 0.003$, with the fitting parameter $R = -0.908 \pm 0.017$. On the other hand, the control sample whose V layer grown at 400°C, has a measured spin Hall angle of $\theta_{SH}(d_V = 30 \text{ nm}) = -0.012 \pm 0.002$, which is comparable to the reported value of V film [14]. The non-zero R indicates the complex

interfacial condition at the V/CoFeB interface, which could be caused by spin backflow (SBF) and/or enhanced spin scattering [30-33].

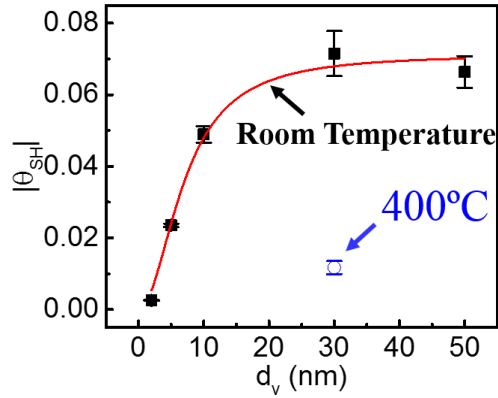


Figure 3.13 The spin Hall angle of V/CoFeB test samples (prepared at room temperature) and control sample (prepared at 400°C).

Based on the spin diffusion equation in NM, the spin current \mathbf{j}_{S_SOT} at NM/FM interface which can induce damping-like torque term [34]

$$\mathbf{j}_{S_SOT}(d_{NM}) = j_{SO}^{SH} \mathbf{m} \times (\mathbf{m} \times \mathbf{y}) \text{Re} \left(\frac{2\lambda G_{\uparrow\downarrow} \tanh \frac{d_{NM}}{2\lambda_{sf}}}{\sigma + 2\lambda G_{\uparrow\downarrow} \coth \frac{d_{NM}}{\lambda_{sf}}} \right) \quad (3.16)$$

where $G_{\uparrow\downarrow} = G_r + iG_i$ is the spin mixing conductance at NM/FM interface, j_{SO}^{SH} represents the spin current generated by the bulk spin Hall effect, d_{NM} is the thickness of nonmagnetic layer and λ_{sf} is the spin diffusion length in nonmagnetic material. If we assume $G_r \gg G_i$, then

$$j_{S_SOT}(d_{NM}) = j_{SO}^{SH} \left(1 - \text{sech} \frac{d_{NM}}{\lambda_{sf}} \right) \left(1 + \frac{G_{NM}}{2G_r} \tanh \frac{d_{NM}}{\lambda_{sf}} \right)^{-1} \quad (3.17)$$

where G_{NM} is the electrical conductance of nonmagnetic layer. Here we apply this relation to derive Equation

$$\frac{\theta_m(d_V)}{\theta_{SH}(\infty)} = \frac{j_{S,SOT}(d_{NM})}{j_{SO}^{SH}} = \frac{2\lambda G_r \tanh \frac{d_{NM}}{2\lambda_{sf}}}{\sigma + 2\lambda G_r \coth \frac{d_{NM}}{\lambda_{sf}}} = \frac{\cosh \frac{d_{NM}}{\lambda_{sf}} - 1}{\cosh \frac{d_{NM}}{\lambda_{sf}} + \frac{G_N}{2G_r} \sinh \frac{d_{NM}}{\lambda_{sf}}} = \frac{\cosh \frac{d_{NM}}{\lambda_{sf}} - 1}{\cosh \frac{d_{NM}}{\lambda_{sf}} + R} \quad (3.18)$$

where $d_{NM} = 2, 5, 10, 30, 50$ nm and $\lambda_{sf} = 16.3$ nm in V/CoFeB system. Please notice that when the spin mixing conductance $G_r \rightarrow \infty$, then Equation 3.18 reduces into

$$\frac{\theta_m(d_V)}{\theta_{SH}(\infty)} = \frac{\cosh \frac{d_{NM}}{\lambda_{sf}} - 1}{\cosh \frac{d_{NM}}{\lambda_{sf}}} = 1 - \operatorname{sech} \frac{d_{NM}}{\lambda_{sf}} \quad (3.19)$$

which has been widely used for a transparent interface condition.

3.2.3.3 Spin Mixing Conductance Analysis

It has been found that the spin transparency at the NM/FM interface plays a critical role in determining the spin torque efficiency [30-33]. The insertion of an atomically thin magnetic layer such as Co, Fe, Ni at a Pt/Py interface [30], or an Hf layer between Pt/CoFeB can significantly modulate the interfacial transparency and enhance the spin injection efficiency from Pt to the FM layer [31].

Based on the drift-diffusion approximation [34-35], in the presence of non-perfect transparent interface, the spin back flow can reduce the SOT efficiency. The damping-like torque and field-like torque efficiencies can be expressed as

$$\xi_{DL} = \theta_{SH}^0 \operatorname{Re} \left\{ \frac{2G_{\uparrow\downarrow} \tanh \frac{d_{NM}}{2\lambda_{sf}}}{G_{NM} + 2G_{\uparrow\downarrow} \coth \frac{d_{NM}}{\lambda_{sf}}} \right\} \quad (3.20)$$

$$\xi_{FL} = \theta_{SH}^0 \operatorname{Im} \left\{ \frac{2G_{\uparrow\downarrow} \tanh \frac{d_{NM}}{2\lambda_{sf}}}{G_{NM} + 2G_{\uparrow\downarrow} \coth \frac{d_{NM}}{\lambda_{sf}}} \right\} \quad (3.21)$$

where ζ_{DL} and ζ_{FL} are the measured effective spin Hall angle due to damping-like torque and field-like torque, respectively, or the so called “spin torque efficiencies” in Reference [32]. θ_{SH}^0 represents the bulk spin Hall angle. As shown in Equation 3.20 and 3.21, due to the interface condition (related with the real and imaginary components of spin mixing conductance), the effective spin Hall angle ζ_{DL} or ζ_{FL} is reduced and less than the bulk spin Hall angle θ_{SH}^0 .

The bare spin mixing conductance $G_{\uparrow\downarrow} = \frac{G_{eff}^{\uparrow\downarrow}}{1 - 2G_{eff}^{\uparrow\downarrow}/G_{NM}}$, where $G_{eff}^{\uparrow\downarrow} = \frac{e^2}{h} g_{eff}^{\uparrow\downarrow}$, and the effective spin mixing conductance $g_{eff}^{\uparrow\downarrow} = \frac{4\pi M_S d_{FM}}{\gamma \hbar} (\alpha - \alpha_0)$, e is the elementary charge, γ is the gyromagnetic ratio, h and \hbar are Planck and reduced Planck constants, respectively. The value of $g_{eff}^{\uparrow\downarrow}$ can be extracted from the previous Gilbert damping constant determined by FMR measurement. Based on this series of V/CoFeB samples with various V thickness, we calculate $G_{eff}^{\uparrow\downarrow} = (0.25 - 1.45) \times 10^{15} \Omega^{-1} m^{-2}$ for samples grown at room temperature. The electrical conductance of V layer is $G_V = (2.04 - 3.06) \times 10^{13} \Omega^{-1} m^{-2}$ which is two orders of magnitudes smaller than $G_{eff}^{\uparrow\downarrow}$. This condition leads to negative bare spin mixing conductance $G_{\uparrow\downarrow}$.

This negative $G_{\uparrow\downarrow}$ is unphysical, suggesting that there may be other additional magnetic damping enhancement mechanisms at the V/CoFeB interface, which could lead to the overestimation of $G_{eff}^{\uparrow\downarrow}$. Due to the complication at the V/CoFeB interface, it becomes difficult to extract the spin Hall angle for V layer. However, if we assume the V/CoFeB system has a transparent interface, we can still properly apply Equation 3.19 to define a lower bound of the effective spin Hall angle as $\theta_V = -0.069 \pm 0.002$. Because of the transparent interface assumption, the fitting spin diffusion length $\lambda = 5.2 \pm 0.3$ nm does not match with $\lambda_{sf} = 16.3 \pm 0.7$ nm, which has been extracted from spin pumping experiment by taking account of a non-transparent interface condition.

3.2.4 Conclusions

Previous research has related a large spin Hall angle with specific crystal structures [5, 6, 36]. For example, a giant spin Hall angle $\theta_{\text{SH}} = -0.12 \sim -0.15$ has been reported in β -Ta [5], which has a stretched tetragonal crystal structure with an enlarged lattice constant and a higher resistivity of $190 \mu\Omega \cdot \text{cm}$ compared with α -Ta. Similar behavior has also been observed in β -W [6]. As a group 5 element, V has a similar Fermi surface as those of Nb and Ta [37]. We therefore speculate the mechanism for the large spin Hall angle in V films is also due to the presence of a tetragonal phase, similar to β -Ta [19]. However, unlike β -Ta and β -W, these sputter-grown V films still have a long spin diffusion length.

In summary, a large spin Hall angle is observed in $3d$ light transition metal V films consisting of mixed bct and bcc phase with small grain size and enlarged interlayer spacing. The spin Hall angle is at least $\theta_{\text{V}} = -0.071 \pm 0.003$, comparable to that of Pt, and is much larger than that in bcc V film grown at 400°C . Similar to β -Ta and β -W, the V films with mixed bct and bcc phases also show high resistivity. However, the spin diffusion length is still as long as 16.3 nm. The surprisingly large spin Hall angle in V will not only be useful for potential applications in SOTs based magnetization switching, but also have ramifications on understanding the origin of the spin Hall angle. In particular, this research suggests that light metals should not be ruled out in the search for efficient spin Hall materials with large spin Hall angle.

REFERENCES

- [1] D. D. Sarma, Proc. Indian Acad. Sci. (Chem. Sci.) **90**, 19 (1981).
- [2] H. L. Wang, C. H. Du, Y. Pu, R. Adur, P. C. Hammel, and F. Y. Yang, Phys. Rev. Lett. **112**, 197201 (2014).
- [3] K. Ando, S. Takahashi, K. Harii, K. Sasage, J. Ieda, S. Maekawa, and E. Saitoh, Phys. Rev. Lett. **101**, 036601 (2008).
- [4] L. Liu, T. Moriyama, D. C. Ralph, and R. A. Buhrman, Phys. Rev. Lett. **106**, 036601 (2011).
- [5] L. Liu, C.-F. Pai, Y. Li, H. W. Tseng, D. C. Ralph, and R. A. Buhrman, Science **336**, 555 (2012).
- [6] C.-F. Pai, L. Liu, Y. Li, H. W. Tseng, D. C. Ralph, and R. A. Buhrman, Appl. Phys. Lett. **101**, 122404 (2012).
- [7] C. F. Pai, M. H. Nguyen, C. Belvin, L. H. Vilela-Leão, D. C. Ralph, and R. A. Buhrman, Appl. Phys. Lett. **104**, 082407 (2014).
- [8] J. Yu, X. Qiu, W. Legrand, and H. Yang, Appl. Phys. Lett. **109**, 042403 (2016).
- [9] M. Akyol, W. Jiang, G. Yu, Y. Fan, M. Gunes, A. Ekicibil, P. Khalili Amiri, and K. L. Wang, Appl. Phys. Lett. **109**, 022403 (2016).
- [10] Y. Niimi, Y. Kawanishi, D. H. Wei, C. Deranlot, H. X. Yang, M. Chshiev, T. Valet, A. Fert, and Y. Otani, Phys. Rev. Lett. **109**, 156602 (2012).
- [11] P. Laczkowski, J.-C. Rojas-Sánchez, W. Savero-Torres, H. Jaffrès, N. Reyren, C. Deranlot, L. Notin, C. Beigné, A. Marty, J.-P. Attané, L. Vila, J.-M. George, and A. Fert, Appl. Phys. Lett. **104**, 142403 (2014).
- [12] Y. Niimi, M. Morota, D. H. Wei, C. Deranlot, M. Basletic, A. Hamzic, A. Fert, and Y. Otani, Phys. Rev. Lett. **106**, 126601 (2011).
- [13] Y. Niimi, H. Suzuki, Y. Kawanishi, Y. Omori, T. Valet, A. Fert, and Y. Otani, Phys. Rev. B **89**, 054401 (2014).

- [14] C. Du, H. Wang, F. Yang, and P. C. Hammel, *Phys. Rev. B* **90**, 140407 (2014).
- [15] D. Qu, S. Y. Huang, and C. L. Chien, *Phys. Rev. B* **92**, 020418 (2015).
- [16] X. Fan, H. Celik, J. Wu, C. Ni, K. Lee, V. O. Lorenz, and J. Q. Xiao, *Nat. Commun.* **5**, 1 (2014).
- [17] X. Fan, A. R. Mellnik, W. Wang, N. Reynolds, T. Wang, H. Celik, V. O. Lorenz, D. C. Ralph, and J. Q. Xiao, *Appl. Phys. Lett.* **109**, 122406 (2016).
- [18] T. Wang, W. Wang, Y. Xie, M. A. Warsi, J. Wu, Y. Chen, V. O. Lorenz, X. Fan, and J. Q. Xiao, *Sci. Rep.* **7**, 1306 (2017).
- [19] E. Montoya, P. Omelchenko, C. Coutts, N. R. Lee-Hone, R. Hübner, D. Broun, B. Heinrich, and E. Girt, *Phys. Rev. B* **94**, 054416 (2016).
- [20] Y. Ding, T. J. Klemmer, and T. M. Crawford, *J. Appl. Phys.* **96**, 2969 (2004).
- [21] J. M. D. Coey, *Magnetism and Magnetic Materials* (Cambridge University Press, 2009).
- [22] B. Heinrich, J. F. Cochran, and R. Hasegawa, *J. Appl. Phys.* **57**, 3690 (1985).
- [23] X. Liu, J. O. Rantschler, C. Alexander, and G. Zangari, **39**, 2362 (2003).
- [24] Y. Tserkovnyak, A. Brataas, and G. Bauer, *Phys. Rev. B* **66**, 224403 (2002).
- [25] L. Liu, R. A. Buhrman, and D. C. Ralph, *ArXiv E-Prints* 1111.3702 (2011).
- [26] Y. K. Kato, *Science* **306**, 1910 (2004).
- [27] G. M. Choi and D. G. Cahill, *Phys. Rev. B.* **90**, 214432 (2014).
- [28] Z. Qiu and S. Bader, *J. Magn. Magn. Mater.* **200**, 664 (1999).
- [29] J. Torrejon, J. Kim, J. Sinha, S. Mitani, M. Hayashi, M. Yamanouchi, and H. Ohno, *Nat. Commun.* **5**, 4655 (2014).
- [30] W. Zhang, W. Han, X. Jiang, S.-H. Yang, and S. S. P. Parkin, *Nat. Phys.* **11**, 496 (2015).
- [31] M.-H. Nguyen, K. X. Nguyen, D. A. Muller, D. C. Ralph, and R. A. Buhrman, *Appl. Phys. Lett.* **106**, 222402 (2015).
- [32] C.-F. Pai, Y. Ou, L. H. Vilela-Leão, D. C. Ralph, and R. A. Buhrman, *Phys.*

- Rev. B **92**, 064426 (2015).
- [33] M.-H. Nguyen, D. C. Ralph, and R. A. Buhrman, Phys. Rev. Lett. **116**, 126601 (2016).
- [34] Y.-T. Chen, S. Takahashi, H. Nakayama, M. Althammer, S. Goennenwein, E. Saitoh, and G. Bauer, Phys. Rev. B **87**, 144411 (2013).
- [35] P. M. Haney, H.-W. Lee, K.-J. Lee, A. Manchon, and M. D. Stiles, Phys. Rev. B **87**, 174411 (2013).
- [36] J. Liu, T. Ohkubo, S. Mitani, K. Hono, and M. Hayashi, Appl. Phys. Lett. **107**, 232408 (2015).
- [37] R. D. Parker and M. H. Halloran, Phys. Rev. B **9**, 4130 (1974).

Chapter 4

SPIN ORBIT EFFECT IN TOPOLOGICAL INSULATOR-FERROMAGNET HETEROSTRUCTURE

4.1 Background and Motivation

As discussed in Chapter 1, topological insulator (TI) becomes a promising candidate as a high efficient source of current-induced spin orbit torques (SOTs). The non-trivial topological surface state features spin-momentum locking, i.e. as a current is flowing through the TI surface, the spin of electrons are pointing in the same direction, creating a large spin accumulation. This spin accumulation diffuses into neighboring FM and creates SOTs.

Bismuth selenide Bi_2Se_3 is a three-dimensional (3D) TI with a direct band gap at Γ point [1-2]. Its surface band structure consists of a single Dirac cone with the Dirac point (DP) close to the bulk valence band. The topological surface state (TSS) has been confirmed to exist in Bi_2Se_3 covered with Fe [3] and Co [4]. The charge current induced SOTs with giant spin torque efficiency have been demonstrated by spin torque ferromagnetic resonance technique (ST-FMR) at room temperature [5]. The temperature dependent SOTs study has also been performed in $\text{Bi}_2\text{Se}_3/\text{CoFeB}$ heterostructures, where the large contribution from TSS at low temperature region has been observed [6].

In this chapter, we discuss charge-current induced SOTs in Bi_2Se_3 /ferromagnet (FM) bilayers. We first demonstrate the giant charge to spin current conversion efficiency in $\text{Bi}_2\text{Se}_3/\text{Py}$ system at room temperature. Then we present our finding of

significant surface contribution in Bi₂Se₃/Co system with temperature dependent SOTs measurement. At the end, we will discuss the on-going work of topological insulator research.

4.2 Methods of Spin Orbit Torques Measurement

In this chapter, three SOTs measurement techniques have been applied to characterize the spin orbit effect (SOE) in FM/TI bilayer systems, including the second harmonic Hall voltage measurement, spin torque ferromagnetic resonance (ST-FMR done by A. R. Mellnik *et al.* in Cornell University) and our newly developed all-optical vector spin torques magnetometer.

4.2.1 Second Harmonic Hall Voltage Measurement

As the most widely used spin torque measurement technique, the second harmonic Hall voltage method is based on magnetoresistance (MR) which is induced by magnetization reorientation in response to current-induced SOTs. The MR response includes planar Hall effect (PHE), anisotropic magnetoresistance (AMR), anomalous Hall effect (AHE), and ordinary Hall effect (OHE).

As shown in Figure 4.1, the second harmonic Hall measurement uses Hall bar structure. The current is applied along the longitudinal x -direction and the Hall voltage is measured along the transverse y direction. As discussed in Chapter 3, SOT consists of field-like and damping-like torques with the effective fields of h_{FL} and h_{DL} in y - and z -directions, respectively. These fields reorient the magnetization and create M_y and M_z components. Consequently, the transverse Hall voltage V_{xy} contains both the PHE due to $m_x m_y$ and AHE due to m_z [7]

$$V_{xy} = V_{PHE} + V_{AHE} = \left(\frac{1}{2} \Delta R_{PHE} \frac{M_x M_y}{M_s^2} + \frac{1}{2} \Delta R_{AHE} \frac{M_z}{M_s} \right) \Delta I \quad (4.1)$$

where ΔR_{PHE} and ΔR_{AHE} are the change in the Hall resistance due to the AHE and PHE, respectively. ΔI is the charge current in the electrical measurement. Here we define φ as the azimuth angle between magnetization \mathbf{M} and x axis, and θ is the zenith angle. Therefore, Equation 4.1 is rewritten as

$$R_{xy} = \frac{1}{2}\Delta R_{\text{PHE}}\cos\theta + \frac{1}{2}\Delta R_{\text{AHE}}\sin^2\theta\sin 2\varphi \quad (4.2)$$

where the Hall voltage signal is expressed by the Hall resistances. We also define φ_0 and θ_0 as the static equilibration state without the current induced SOTs, and $\varphi = \varphi_0 + \Delta\varphi$, $\theta = \theta_0 + \Delta\theta$ as the final position of magnetization under the influence of SOTs.

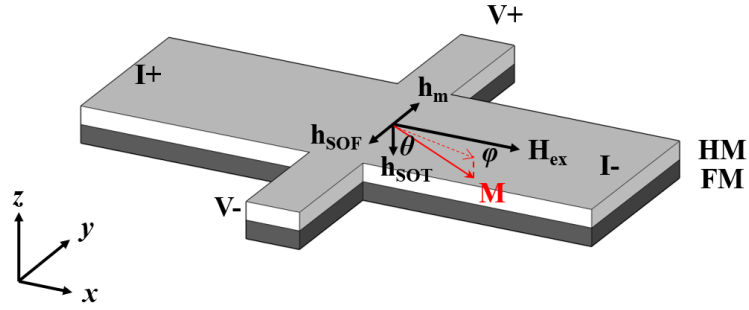


Figure 4.1 The schematic illustration of second harmonic Hall voltage measurement of the current induced SOTs.

An AC current $\Delta I = \Delta I_0 \sin \omega t$ is applied along the x -axis. ΔI , φ and θ are substituted into Equation 4.1 and 4.2, the Hall resistance R_{xy} is expanded as

$$R_{xy} \approx \frac{1}{2}\Delta R_{\text{AHE}}(\cos\theta_0 - \Delta\theta\sin\theta_0) + \frac{1}{2}\Delta R_{\text{PHE}}(\sin^2\theta_0 + \Delta\theta\sin 2\theta_0)(\sin 2\varphi_0 + 2\Delta\varphi\cos 2\varphi_0) \quad (4.3)$$

The corresponding Hall voltage is expressed as

$$V_{xy} = V_0 + V_\omega \sin \omega t + V_{2\omega} \cos \omega t \quad (4.4)$$

where V_0 is a DC term, V_ω and $V_{2\omega}$ are the first order and the second order signal which can be detected from a lock-in amplifier

$$V_0 = \frac{1}{2}(B_\theta + B_\varphi)\Delta I \quad (4.5)$$

$$V_\omega = A\Delta I \quad (4.6)$$

$$V_{2\omega} = -\frac{1}{2}(B_\theta + B_\varphi)\Delta I \quad (4.7)$$

where the coefficients A , B_φ and B_θ are expressed as

$$A = \frac{1}{2}\Delta R_{\text{AHE}}\cos\theta_0 + \frac{1}{2}\Delta R_{\text{PHE}}\sin^2\theta_0\sin 2\varphi_0 \quad (4.8)$$

$$B_\theta = \frac{1}{2}(-\Delta R_{\text{AHE}}\sin\theta_0 + \Delta R_{\text{PHE}}\sin 2\theta_0\sin 2\varphi_0)\Delta\theta \quad (4.9)$$

$$B_\varphi = \Delta R_{\text{PHE}}\sin^2\theta_0\cos 2\varphi_0\Delta\varphi \quad (4.10)$$

As shown in Equation 4.9 and Equation 4.10, B_θ and B_φ are proportional to the current induced angle changes of $\Delta\theta$ and $\Delta\varphi$, respectively, which are related to h_{DL} and h_{FL} caused by SOTs

$$\Delta\theta = \frac{\cos\theta_0(\Delta H_x\cos\varphi_H + \Delta H_y\sin\varphi_H) - \sin\theta_0\Delta H_z}{(H_K - H_A\sin^2\varphi_H)\cos 2\varphi_H + H\cos(\theta_H - \theta_0)} \quad (4.11)$$

$$\Delta\varphi = \frac{-\Delta H_x\sin\varphi_H + \Delta H_y\cos\varphi_H}{-H_A\sin\theta_0\cos 2\varphi_H + H\sin\theta_H} \quad (4.12)$$

Therefore, the effective current induced fields ΔH_x , ΔH_y and ΔH_z can be extracted by fitting these equations. For geometry illustrated in Fig. 4.1, we have $\theta_0 = 90^\circ$ and $\varphi_H = 0^\circ$. Substituting Equation 4.9 and 4.10 into Equation 4.7, the second order harmonic voltage can be written as

$$V_{2\omega} = \left(\frac{1}{2}\Delta R_{\text{AHE}} \frac{\Delta H_z}{H_K + H_{\text{ex}}} + \Delta R_{\text{PHE}} \frac{\Delta H_y}{H_{\text{ex}} - H_A} \right) \Delta I \quad (4.13)$$

Based on the coordinates defined in Figure 4.1, ΔH_z is the effective field h_{DL} of damping-like torque, ΔH_y represents the effective field h_{FL} of field-like torque. The

typical first order and second order Hall voltages are shown in Figure 4.2. The second order Hall voltage includes both AHE and PHE responses. The effective fields of SOTs can be extracted based on Equation 4.13. The AHE and PHE resistance $\Delta R_{\text{AHE}}(H_{\text{ex}})$ and $\Delta R_{\text{PHE}}(H_{\text{ex}})$ can be determined from the first order Hall signal V_{ω} , which does not contain any current-induced effects.

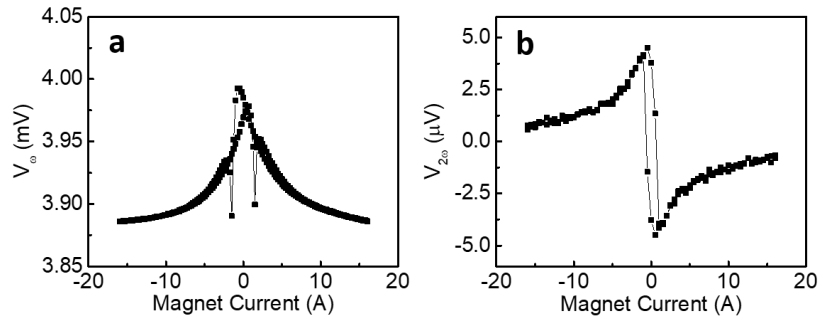


Figure 4.2 Typical second harmonic Hall voltage measurement results of (a) the first order signal V_{ω} and (b) the second order signal $V_{2\omega}$.

Further, a second order PHE method, which is based on this second harmonic technique, has been developed by our group [8-9]. The method use an external calibration magnetic field and greatly simplifies the analyses. As shown in Figure 4.3 (a), the experimental setup includes an extra calibration field h_{cal} generated by a small Helmholtz coil along y direction. Under this configuration, since the AHE voltage is much smaller compared with the PHE signal, we neglect the AHE contribution, and the detected transverse voltage is only related with the current induced in-plane field $h_{\text{I}} = h_{\text{FL}} + h_{\text{Oe}}$. The second order Hall voltage can be written as

$$\Delta V = V(+j, +h_{\text{cal}}, H_{\text{ex}}) - V(-j, -h_{\text{cal}}, H_{\text{ex}}) = 2j\Delta\rho w \cos 2\phi_0 \frac{h_{\text{FL}} + h_{\text{Oe}} - h_{\text{cal}}}{H_{\text{ex}} \cos \phi_0 \pm H_{\text{a}}} \quad (4.14)$$

The second order voltage with different calibration fields is shown in Figure 4.3 (b). In practical fitting process, we perform a linear regression analysis between the $\Delta V(h_{\text{cal}} = 0)$ and $\Delta V(h_{\text{cal}}) - \Delta V(-h_{\text{cal}})$, and the linear fitting result is shown in Figure 4.3 (c). Figure 4.3 (d) shows the linear dependence of field like torque h_{FL} with the applied current.

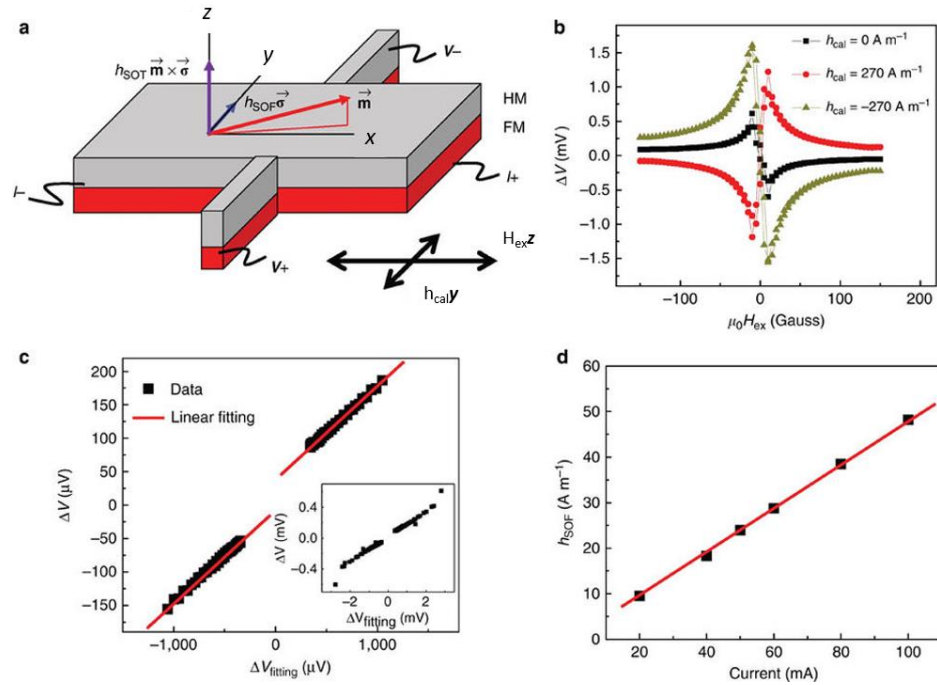


Figure 4.3 The second order PHE field like torque measurement. (a) The experimental setup which includes an external Helmholtz coil generating a calibration field. (b) The Hall voltage measurement results with different calibration fields. (c) The linear regression analysis based on the test result and calibration result. (d) The linear response indicates the measurement is in the linear response regime. (Reprinted by permission adapted from [9], copyright (2014))

4.2.2 All Optical Spin Torque Measurement

The second harmonic electrical measurement has its drawback since the signal is complicated by the PHE, AHE, and thermal effect, especially for in-plane anisotropy FMs system that make it difficult to separate the thermal-induced signal from the AHE signal [10-11]. Comparing to this indirect electrical techniques that based on MR response, the MOKE spin torque magnetometer directly probes the magnetization direction and avoids the influence from thermal effects.

In Chapter 3, we have already introduced the damping-like torque measurement technique based on polar MOKE. Here we focus on the field-like torque measurement based on quadratic MOKE response.

For the normal incident light, the MOKE response includes both the first order term and the second order term [12]

$$\psi(\mathbf{m}) = \alpha_{Polar} m_z + \beta_{Quad} m_x m_y \quad (4.15)$$

Measuring polar MOKE which arises from m_z components, we can determine h_{DL} as we discussed in Chapter 3. h_{FL} is in y-direction and thus induces m_y , which is contained in second order or quadratic MOKE signal. In order to probe the quadratic MOKE, a circular polarized incident light can be used since m_z component will not induce any changes in circular polarized light.

Comparing Equation 4.15 with Equation 4.1, we find the similar form between MOKE and electrical spin torque measurement methods. The first order signal in Equation 4.15 is similar to AHE induced MR in second harmonic Hall voltage measurement, which is proportional to the out-of-plane component of magnetization m_z . The second order quadratic term is also comparable to PHE voltage in Equation 4.1, which is related with the product of in-plane components m_x and m_y . As shown in Figure 4.4 (a), the linear incident light can be assumed as the superimposition of two

separate circular polarized lights with opposite polarizations. Due to the magnetic circular dichroism caused by out-of-plane component m_z , the right-handed and left-handed polarized lights have different absorption rates, and the reflected components combine into an elliptical polarization, which could be detected as AHE-like response; In Figure 4.4 (b), as a linear polarized light could be decomposed into two orthogonal linear components along x and y axis. Due to the magnetic linear dichroism, which means the linear polarized light has different absorption rates along two orthogonal axes. It is similar to PHE induced resistance in the electrical Hall measurement, electrons have different conductivities along two orthogonal directions, because of s - d scattering of electrons in the direction of magnetization. Furthermore, the circular polarized light can always be decomposed into two linear component, which could also induce this PHE-like response, but no AHE-like response.

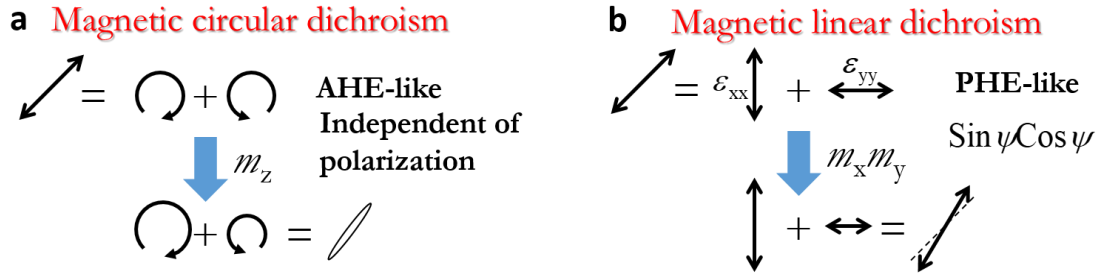


Figure 4.4 The illustration of (a) MOKE circular dichroism (first order) and (b) linear dichroism (second order) response.

The normal incident MOKE response can be rewritten as

$$\Delta\psi_{Kerr} \propto \eta_{Polar} m_z + \eta_{Quad} m_x m_y = \eta_{Polar} \frac{h_{DL}}{|H_{ex}| + M_{eff}} + \eta_{Quad} \frac{h_{FL}}{H_{ex}} \cos 2\phi_{laser} \quad (4.16)$$

where the angle ϕ_{laser} is the angle between the linear incident light polarization direction and the magnetization orientation. For a typical HM/FM heterostructure Pt/Py system, the normal incident MOKE measurement results are shown in Figure 4.5. The polar MOKE response is almost fifty times stronger than the quadratic MOKE coefficient, which is shown in Figure 4.5 (a). In Figure 4.5 (b), the 0° and 90° polarization signals include both polar and quadratic components, but the quadratic term will be eliminated at 45° polarization, which could be accurately described by Equation 4.16.

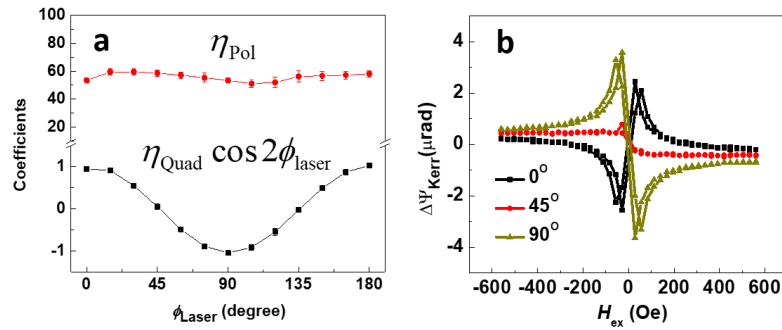


Figure 4.5 The normal incident MOKE measurement results of Pt/Py bilayer. (a) The polar and quadratic component response coefficients as function of the polarization of linear incident light; (b) The Kerr rotation signals with different linear polarization direction.

In practical measurement, an extra calibration wire is placed under the test MOKE samples, which generates a calibration magnetic field. As shown in Figure 4.6 (a), the quadratic response induced by the field-like torque h_{FL} and calibration field h_{cal} , respectively, show the $1/H_{\text{ex}}$ feature (Equation 4.16). The linear regression fitting is shown in Figure 4.6 (b).

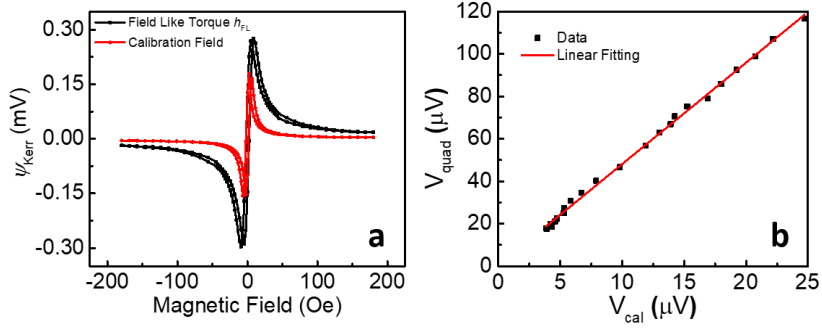


Figure 4.6 The quadratic MOKE field like torque measurement of Pt/Py bilayer structure. (a) The Kerr rotation response induced by spin orbit torques (black) and external calibration field (red) in FM layer, respectively.

4.2.3 Comparison between MOKE and Electrical Spin Torque Measurements

In this section, we compare the SOT measurement results between MOKE, second harmonics Hall and ST-FMR techniques, where ST-FMR results are based on our collaborators A. R. Mellnik *et al.* in Cornell University [13]. We demonstrate that all-optical MOKE technique is able to measure both the damping-like torque h_{DL} and the field-like torque h_{FL} , and it also has advantages comparing to other electrical methods. Especially, MOKE technique can simplify the extraction process of SOT measurements. In addition, this optical technique can be used to measure SOTs involving magnetic insulators where electrical measurement cannot and magnetic layers with perpendicular magnetic anisotropy.

In this study, we use a series of 6 nm Pt/Py(x nm) as the test samples, where $x = 2, 4, 6, 8$ and 10 nm. The summary of spin Hall angle induced by both damping-like torque and field-like torque are plotted in Figure 4.7 (a) and (b), respectively. All the ST-FMR measurement h has been performed at Cornell. The trend of h_{DL} and h_{FL} match between MOKE and electrical measurements, but the magnitude deviates. The second harmonic method works well with perpendicular magnetic anisotropy system but it has

difficult to separate the thermally induced effect in the system with in-plane anisotropy. For the ST-FMR, it works in both out-of-plane and in-plane anisotropy systems, but it is difficult to estimate the real radio frequency (RF) current going through samples which is a crucial fitting parameter. In addition there is other artifacts from spin pumping or inverse spin Hall effect (ISHE) which can contribute to the output voltage signal.

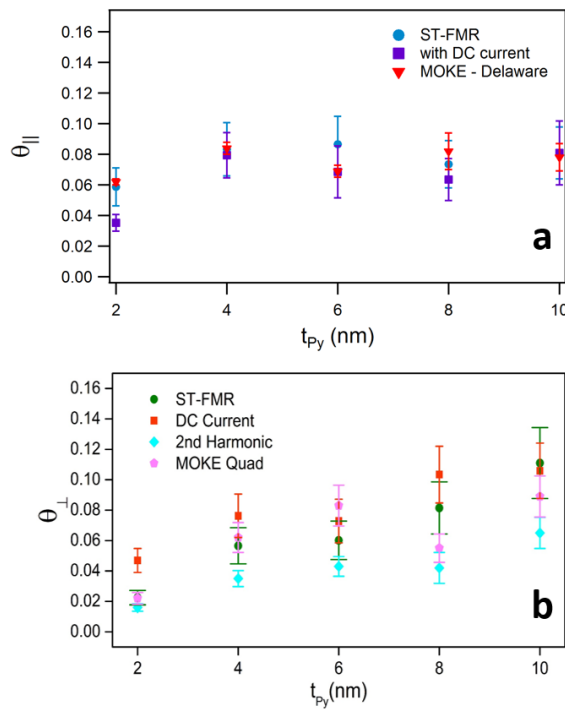


Figure 4.7 The damping-like and field-like torques spin Hall angle θ_{\parallel} and θ_{\perp} based on various spin torque measurement techniques.

The MOKE spin torque magnetometer can determine both damping-like and field-like SOTs. It probes the magnetization directly and does not have all the artifacts

mentioned above. Therefore, as will be discussed in the following section, the research of SOT in FM/TI system is mainly relied on the MOKE measurement.

4.3 Spin Orbit Torque in TI/FM Bilayer

4.3.1 Giant Spin Orbit Torque Efficiency in $\text{Bi}_2\text{Se}_3/\text{Ni}_{80}\text{Fe}_{20}$ Bilayer

The room temperature damping-like torque has been measured by the polar MOKE at Delaware and by the ST-FMR at Cornell. The results are shown in Figure 4.8 (a). Comparing with the damping-like torque in Pt/Py ($\text{Ni}_{80}\text{Fe}_{20}$) bilayers (Figure 4.7 (a)), the SOT efficiency in $\text{Bi}_2\text{Se}_3(8 \text{ nm})/\text{Py}(x \text{ nm})$ is almost one order higher than that in conventional HM/FM system like Pt/Py. Similarly, in Figure 4.8 (b), the field-like torque is also approximately 10 times larger than that of Pt/Py. The strength of spin torque per charge current density in Bi_2Se_3 is the greatest reported by so far.

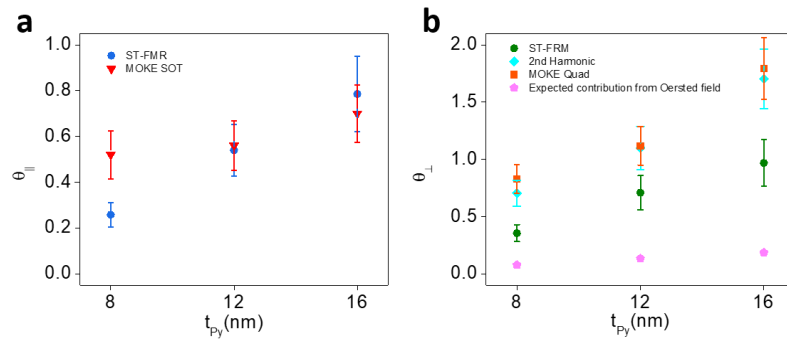


Figure 4.8 The effective (a) in-plane and (b) out-of-plane spin Hall angle in $\text{Bi}_2\text{Se}_3(8 \text{ nm})/\text{Py}(x \text{ nm})$ ($x = 8, 12, 16 \text{ nm}$) bilayers.

The room temperature giant spin orbit torque efficiency is contributed by the coexistence of topological surface state (TSS) and the bulk spin Hall effect (SHE),

since Bi_2Se_3 has a non-insulating bulk which has very high spin-orbit coupling. The temperature dependent sheet resistance for 20 nm Bi_2Se_3 is shown in Figure 4.9. The sheet resistance decreases monotonously as the temperature decreases. After the temperature is lower than 50 K, Bi_2Se_2 bulk becomes insulating, and the TSS has a temperature independent sheet resistance.

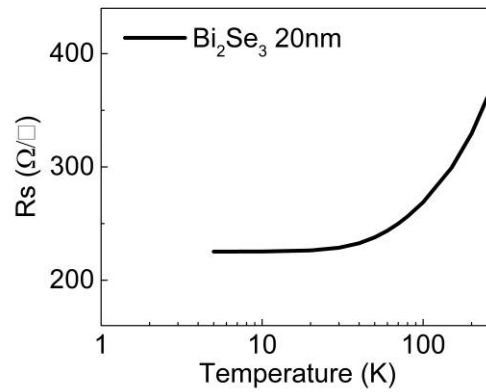


Figure 4.9 The temperature dependent sheet resistance of 20 nm Bi_2Se_3 film.

In the study of the origin of the observed SOTs, we have performed temperature dependent SOTs measurements on $\text{Bi}_2\text{Se}_3(10 \text{ nm})/\text{Py}(4 \text{ nm})$ bilayers. Since our MOKE setup equipped with cryostat is still under testing, therefore, we present the temperature dependent SOTs data here taken by second harmonic Hall voltage measurements.

Bi_2Se_3 thin films of 10 nm thick were grown with molecular beam epitaxy (MBE) on sapphire substrates using a selenium cracker [14] in Prof. Stephanie Law's group at University of Delaware. The samples were then transferred into a magnetron

sputtering system in our lab, where a 4 nm Py layer was grown at 3.0 mTorr on the Bi_2Se_3 film. Another 5 nm SiO_2 layer was capped on the top. The temperature dependent sheet resistance, carrier density and mobility are shown in Figure 4.10. The sheet resistance in Figure 4.10 (a) shows a rapid rising at $T < 50$ K, which indicates TSS dominates the conduction at low temperature region, and the bulk becomes insulating. The carrier density and mobility are comparable with the published values [14].

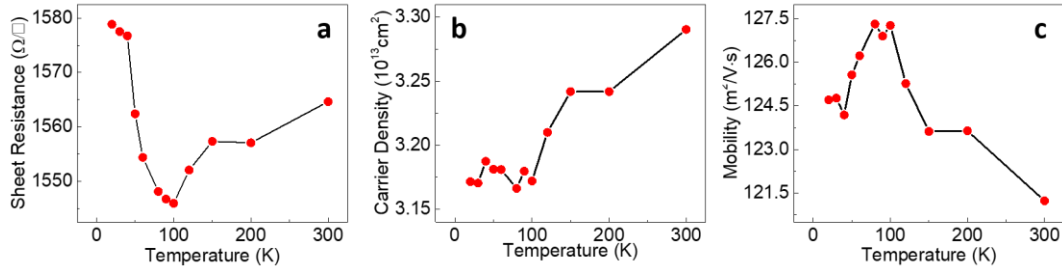


Figure 4.10 The temperature dependence of (a) sheet resistance, (b) carrier density and (c) mobility of 10 nm Bi_2Se_3 .

These samples were patterned into Hall bar structure using conventional photolithography procedure. The active regions of Hall bar devices range from 90 ~ 150 μm long and 15 ~ 100 μm wide. Except various sizes of Hall bars, there are also other devices for MOKE measurement on the same $10 \times 10 \text{ mm}^2$ chip. The typical Hall bar device is shown in Figure 4.11 (a).

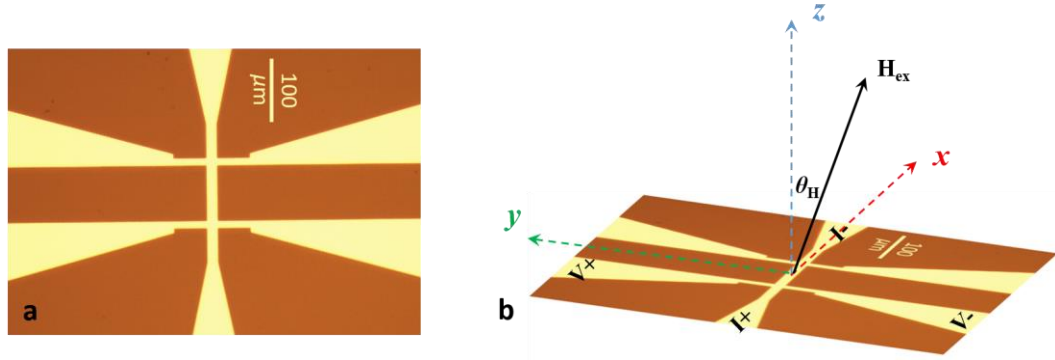


Figure 4.11 (a) Typical Hall bar device for the second harmonic Hall voltage measurement. This six terminals device is also used in electrical resistivity measurement. (b) The illustration of second harmonic Hall measurement configuration.

As shown in Figure 4.11 (b), the second harmonic measurement was performed under two configurations: (1) the in-plane field scan with the external field H_{ex} along x -axis ($\theta_H \approx \pi/2$), and (2) the out-of-plane field scan along z -axis ($\theta_H \approx 0$). The alternating current (AC) $\Delta I = \Delta I_0 \sin \omega t$ is applied in x direction, which is shown in Figure 4.11 (b). While the transverse Hall voltage is read out between “ V_+ ” and “ V_- ” along y direction.

For the in-plane field scan configuration ($\theta_0 = 90^\circ$, $\varphi_H = 0^\circ$), the output second order Hall voltage $V_{2\omega}$ is described by Equation 4.13. As shown in Figure 4.12, the second order Hall response at different temperatures can be fitted based on the Equation 4.13. Since Py has very small AHE magnetoresistance, only the in-plane current induced the effective field of field-like torque h_{FL} can be determined in this configuration.

In the out-of-plane field scan configuration, we apply an external magnetic field H_{ex} along $\theta_H \approx 5^\circ$, and $\varphi_0 = \varphi_H = 0^\circ$. The measurement results are shown in

Figure 4.13. Substituting Equation 4.9 and 4.10 into Equation 4.7 gives to the following expression

$$V_{2\omega} = -\frac{\Delta R_{\text{AHE}}}{2} \left[\frac{1}{2} \frac{\sin^2 \theta_0 \Delta H_z}{H_K \cos 2\theta_0 + H_{\text{ex}} \cos(\theta_H - \theta_0)} + \xi \frac{\sin^2 \theta_0 \Delta H_y}{H_{\text{ex}} \sin \theta_H - H_A \sin \theta_0} \right] \Delta I \quad (4.17)$$

where $\xi = \Delta R_{\text{AHE}} / \Delta R_{\text{PHE}}$, ΔH_z and ΔH_y represent h_{DL} and h_{FL} , respectively. The angle θ_0 can be extracted from the first order Hall voltage

$$V_{\omega} = \frac{1}{2} \Delta R_{\text{AHE}} \cos \theta_0 \Delta I \quad (4.18)$$

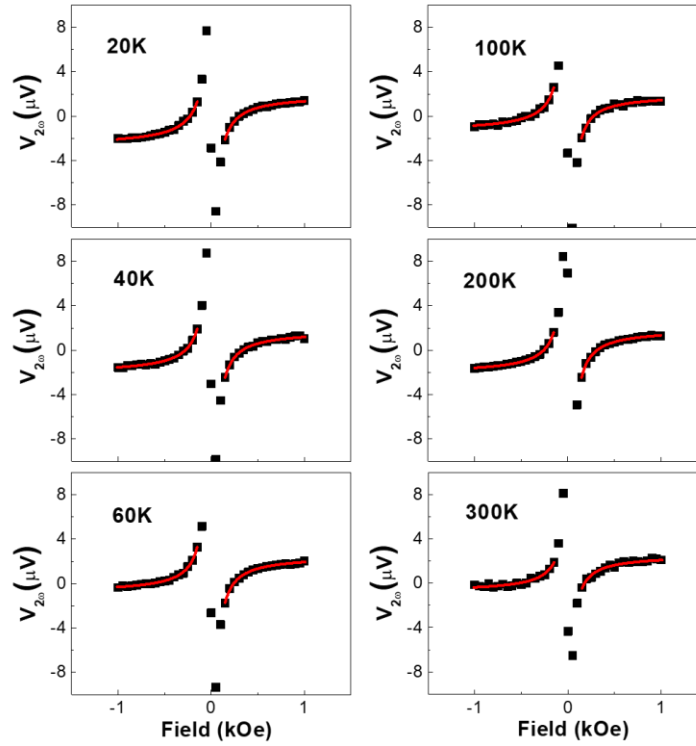


Figure 4.12 The second order Hall voltage $V_{2\omega}$ as a function of in-plane magnetic field at different temperatures for $\text{Bi}_2\text{Se}_3(10 \text{ nm})/\text{Py}(4 \text{ nm})$ bilayers.

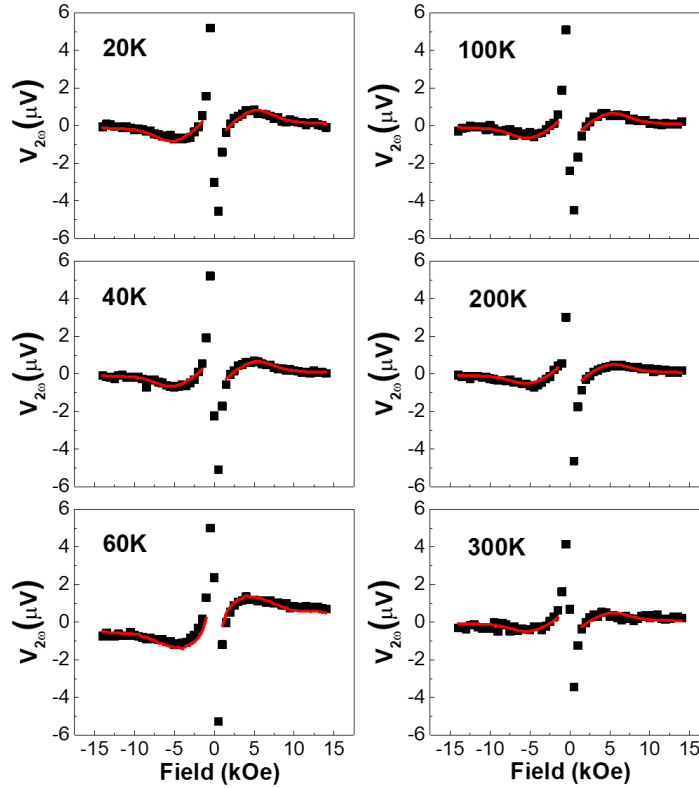


Figure 4.13 The second order Hall voltage $V_{2\omega}$ as a function of nearly out-of-plane magnetic field ($\theta_H \approx 5^\circ$) at different temperatures for $\text{Bi}_2\text{Se}_3(10 \text{ nm})/\text{Py}(4 \text{ nm})$ bilayers.

The results of h_{DL} and h_{FL} are shown in Figure 4.14. We find the damping-like torque is larger than the field-like torque and both effects decrease with decreasing temperatures. There are three potential contributions to h_{DL} and h_{FL} : (1) the TSS which in general gives rise to $h_{\text{FL}} > h_{\text{DL}}$. The surface state induced effect weakly depends on the temperature; (2) the Rashba effect which also leads to $h_{\text{FL}} > h_{\text{DL}}$ but the effect is decreasing with decreasing temperature; (3) the bulk SHE which usually has $h_{\text{FL}} < h_{\text{DL}}$ and decrease with decreasing temperature since the bulk conductivity in TI becomes insulating at low temperature region. In Figure 4.14, we have observed

significantly contributions from bulk SHE. The TSS effect has a weak contribution based on h_{FL} and h_{DL} temperature dependent measurement.

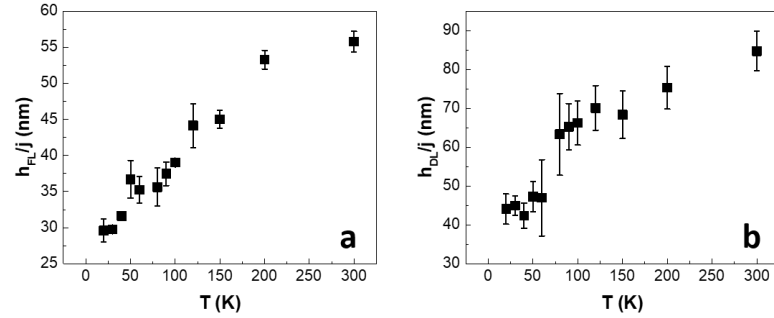


Figure 4.14 (a) The field-like torque efficiency and (b) damping-like torque efficiency as a function the temperature for $\text{Bi}_2\text{Se}_3(10 \text{ nm})/\text{Py}(4 \text{ nm})$ bilayers.

4.3.2 Topological Surface State Induced Spin Orbit Torques

As discussed in the last section, there is no solid evidence to support our expectation that the TSS would dominate the SOTs at low temperature region since the bulk of TI becomes insulating, leading to minimum contributions from SHE.

Very recently, Prof. Branislav Nikolic at University of Delaware has performed first-principles calculation on $\text{Bi}_2\text{Se}_3/\text{Co}$ heterostructures [15]. The most notable findings: (1) there is strong influence of metallic FM on TI where the Dirac point is significantly shifted into valence bands due to charge transfer, and (2) there is strong SOC proximity effect at the interface between TI and FM layers, resulting in different spin textures on both side of the interface, where the spin textures in TI is different from originally predicted spin-momentum locking and the spin textures in FM different from the bulk of FM layer. The study successfully explained the

experimental results of significant changes in charge-spin conversion in TI/Cu/FM. The study also indicate that the SOTs will be dominated by the interfacial electronic structures and spin textures which are modified from standalone TIs and FMs. The calculation of SOTs is currently underway.

Guided by this theory, we also investigated SOT behaviors in $\text{Bi}_2\text{Se}_3(20 \text{ nm})/\text{Co}(3 \text{ nm})$ bilayers. As shown in Figure 4.15, the in-plane field scans were performed on this sample. Unlike the negligible AHE signal in $\text{Bi}_2\text{Se}_3/\text{Py}$ system, Co has much larger AHE resistivity ρ_{AHE} than that of Py. Based on the expression of Equation 4.13, we can simultaneously extract both effective fields of h_{DL} and h_{FL} , which are represented by ΔH_z and ΔH_y , respectively.

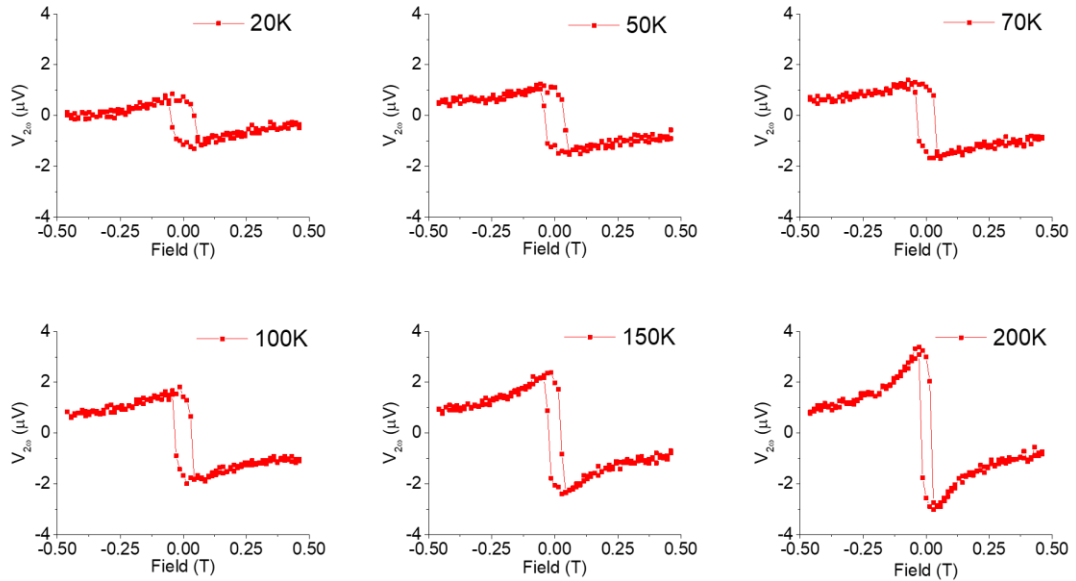


Figure 4.15 The second order Hall voltage as a function of in-plane magnetic field at different temperatures for $\text{Bi}_2\text{Se}_3(20 \text{ nm})/\text{Co}(3 \text{ nm})$ bilayer.

However, in order to determine ΔR_{AHE} and ΔR_{PHE} in Equation 4.13, both the in-plane and out-of-plane field scans have to be measured. The first order Hall voltage was used to extract the PHE and AHE resistances following the expression

$$V_{\omega} = \left(\frac{1}{2} \Delta R_{\text{AHE}} \cos \theta_0 + \frac{1}{2} \Delta R_{\text{PHE}} \sin^2 \theta_0 \sin 2\varphi_0 \right) \Delta I \quad (4.19)$$

The typical V_{ω} results of both in-plane and out-of-plane scan are shown in Figure 4.16 (a) and (b), respectively. According to Equation 4.19, for in-plane field scan, $\theta_0 = 90^\circ$, V_{ω} attains maximum when $\sin 2\varphi_0 = 1$, then $\Delta R_{\text{PHE}} = 2V_{\omega}(\text{max})/\Delta I$. For out-of-plane field scan, $\varphi_0 = 0^\circ$, V_{ω} attains maximum when $\cos \theta_0 = 1$, then $\Delta R_{\text{AHE}} = 2V_{\omega}(\text{max})/\Delta I$. Therefore, ΔR_{PHE} and ΔR_{AHE} could be determined in Figure 4.16 (a) and (b), respectively.

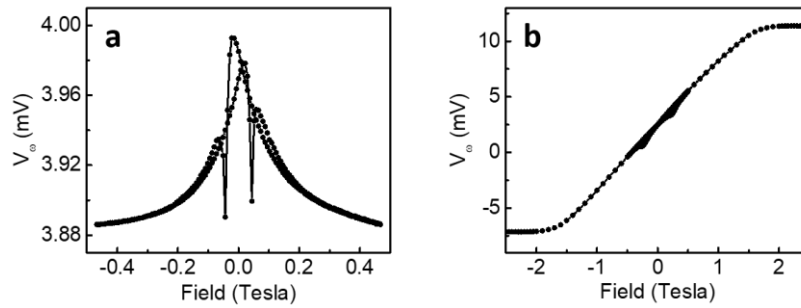


Figure 4.16 The first order Hall voltage as a function of (a) in-plane and (b) out-of-plane magnetic fields for $\text{Bi}_2\text{Se}_3(20 \text{ nm})/\text{Co}(3 \text{ nm})$ bilayer.

The temperature dependent ΔR_{PHE} and ΔR_{AHE} , extracted from the first order Hall voltage, are shown in Figure 4.17 (a) and (b), respectively.

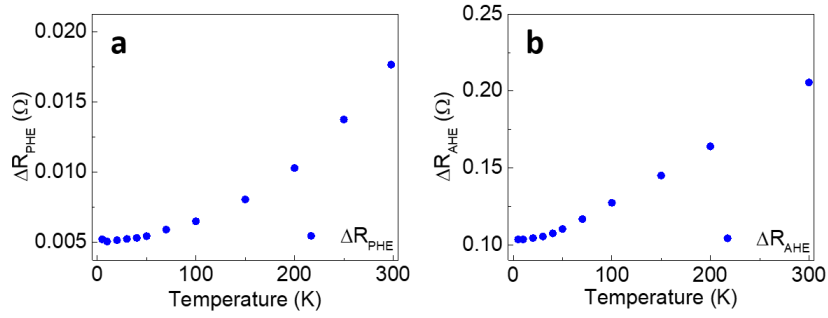


Figure 4.17 The ΔR_{PHE} and ΔR_{AHE} extracted from temperature dependent first order Hall voltage.

The out-of-plane anisotropy field H_K and in-plane anisotropy field H_{an} can also be extracted from data shown in Figure 4.16. The H_{ex} corresponding to the maximum of V_{ω} in Figure 4.16 (a) represents H_{an} . Figure 4.16 (b) is the out-of-plane magnetic hysteresis loop which can indicate H_K . With these parameters, we can fit the second harmonic results to extract ΔH_z (h_{DL}) and ΔH_y (h_{FL}) according to Equation 4.13. All fitting results (black curves) are shown in Figure 4.18. The high field of 0.2 T to 0.5 T is chosen to fit the data since the low field data involves magnetization switching and domain formation. The extracted h_{FL} and h_{DL} are shown in Figure 4.19. We find both the field-like torque and the damping-like torque decrease with decreasing temperature to 50 K, below which both SOTs rapidly increase with decreasing temperature.

The bulk SHE induced spin orbit torques in TI is decreasing with decreasing temperature since the bulk of TI is becoming insulating. The Rashba effect induced spin orbit torques decrease weakly with temperature [6]. As we expected, the rapid increase in SOTs at low temperature is due to the contribution from TSS. However, h_{DL} in Figure 4.19 (b) is very interesting. Firstly, the damping-like torque switches the

sign near 30 K; Secondly, h_{DL} at $T= 300$ K is small compared with the giant SOT in $\text{Bi}_2\text{Se}_3/\text{Py}$ system at room temperature [5].

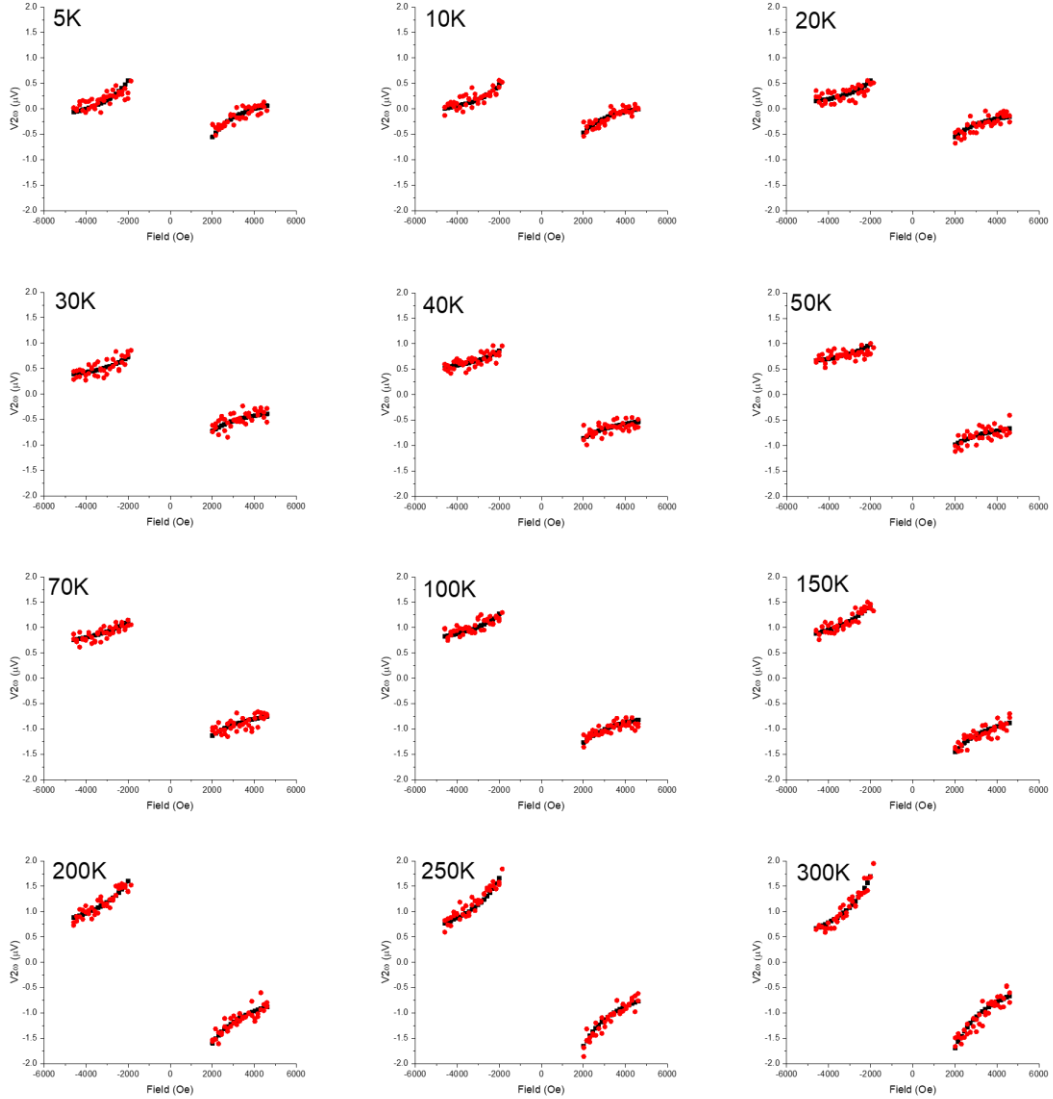


Figure 4.18 The second order Hall voltage fitting results under different temperatures. The fitting region is chosen at the range of 0.2 T to 0.5 T, in order to satisfy the small angle approximation in the fitting process that is based on Equation 4.13.

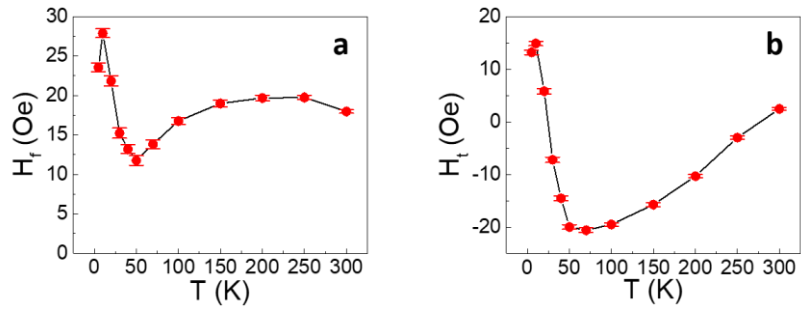


Figure 4.19 The summary of temperature dependent SOTs measurement in 20 nm Bi₂Se₃/3 nm Co heterostructure. (a) The field like torque efficiency and (b) damping like torque efficiency.

Similar results have been observed in other samples. The results of another Bi₂Se₃(10 nm)/Co(5 nm) sample are shown in Figure 4.20, and the damping like torque also reverses sign near $T = 40$ K (Figure 4.20 (e)).

The sign change could be due to two reasons: (1) the thermal effect which can also contribute to the Hall signal, its sign depends on the direction of the temperature gradient ΔT perpendicular to the sample plane [8]; (2) the opposite directions of spin polarization arising from TSS and bulk SHE of TI.

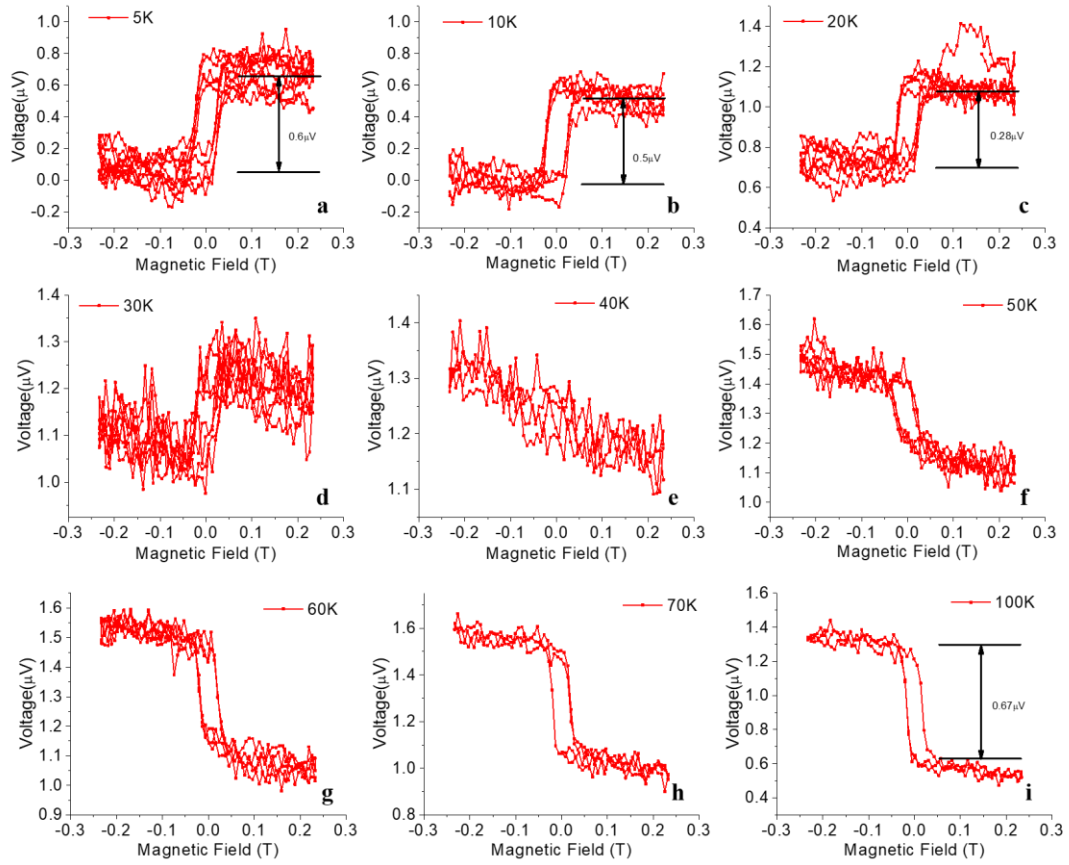


Figure 4.20 The temperature dependent of the second harmonic measurement of $\text{Bi}_2\text{Se}_3(10 \text{ nm})/\text{Co}(5 \text{ nm})$ samples.

To gauge the thermal effect, we performed a current dependent measurement since SOT is linearly proportional to the current and thermal effect is quadratic on the current. The results are shown in Figure 4.21. The extracted effective spin orbit field h_{FL} is linearly proportional to the current density. Unfortunately, the damping-like field h_{DL} is too noise to show definitely linear relation with the current density.

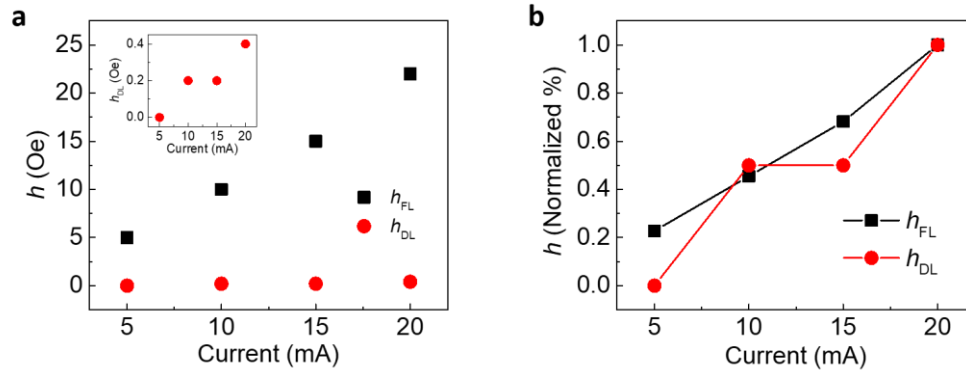


Figure 4.21 The current dependent measurements of h_{DL} and h_{FL} at room temperature

To further remove the thermal effect, we performed a separate polar MOKE measurement at room temperature of $\text{Bi}_2\text{Se}_3(20 \text{ nm})/\text{Co}(5 \text{ nm})$ sample. Since MOKE directly measures the magnetization direction not the Hall voltage, therefore it is free of thermal contribution. The MOKE measurement is shown in Figure 4.22. The extracted $h_{DL} = 0.57 (1 \pm 0.25)$ Oe is consistent with the second harmonic measurement result in Figure 4.19 (b). Therefore, we are confident that the sign change is not an artifact due to offset of the thermal contribution.

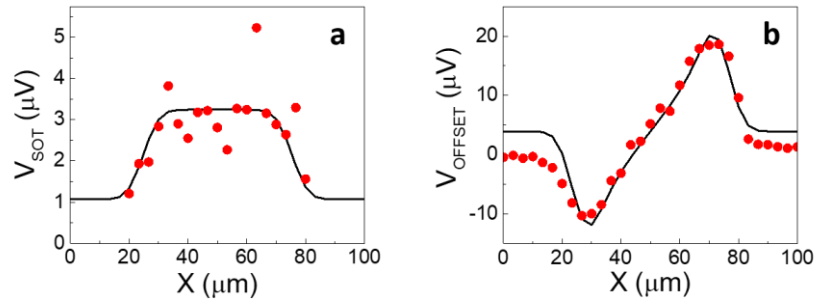


Figure 4.22 The polar MOKE SOT measurement of $\text{Bi}_2\text{Se}_3(20 \text{ nm})/\text{Co}(5 \text{ nm})$ sample at room temperature. (a) The damping like torque spatial line scan and (b) the out-of-plane current induced Oersted field distribution across the sample's transverse direction.

To fully interpret the results, our collaborator Prof. Nikolic is performing the first-principles calculations on the spin orbit torque $\text{Bi}_2\text{Se}_3/\text{Co}$ bilayers that are dominated by the interface electronic structures and spin textures, which are very different from the stand-alone Bi_2Se_3 and Co layers [15].

REFERENCES

- [1] H. Zhang, C.-X. Liu, X.-L. Qi, X. Dai, Z. Fang, and S.-C. Zhang, *Nat. Phys.* **5**, 438 (2009).
- [2] Y. Xia, D. Qian, D. Hsieh, L. Wray, A. Pal, H. Lin, A. Bansil, D. Grauer, Y. S. Hor, R. J. Cava, and M. Z. Hasan, *Nat. Phys.* **5**, 398 (2009).
- [3] M. R. Scholz, J. Sánchez-Barriga, D. Marchenko, A. Varykhalov, A. Volykhov, L. V. Yashina, and O. Rader, *Phys. Rev. Lett.* **108**, 256810 (2012).
- [4] M. Ye, S. V. Ereameev, K. Kuroda, E. E. Krasovskii, E. V. Chulkov, Y. Takeda, Y. Saitoh, K. Okamoto, S. Y. Zhu, K. Miyamoto, M. Arita, M. Nakatake, T. Okuda, Y. Ueda, K. Shimada, H. Namatame, M. Taniguchi, and A. Kimura, *Phys. Rev. B.* **85**, 205317 (2012).
- [5] A. R. Mellnik, J. S. Lee, A. Richardella, J. L. Grab, P. J. Mintun, M. H. Fischer, A. Vaezi, A. Manchon, E. -A. Kim, N. Samarth, and D. C. Ralph, *Nature* **511**, 449 (2014).
- [6] Y. Wang, P. Deorani, K. Banerjee, N. Koirala, M. Brahlek, S. Oh, and H. Yang, *Phys. Rev. Lett.* **114**, 257202 (2015).
- [7] M. Hayashi, J. Kim, M. Yamanouchi, and H. Ohno, *Phys. Rev. B* **89**, 144425 (2014).
- [8] X. Fan, J. Wu, Y. Chen, M. J. Jerry, H. Zhang, and J. Q. Xiao, *Nat. Commun.* **4**, 1799 (2013).
- [9] X. Fan, H. Celik, J. Wu, C. Ni, K. Lee, V. O. Lorenz, and J. Q. Xiao, *Nat. Commun.* **5**, 1 (2014).
- [10] K. Garello, I. M. Miron, C. O. Avci, F. Freimuth, Y. Mokrousov, S. Blügel, S. Auffret, O. Boulle, G. Gaudin, and P. Gambardella, *Nat. Nanotechnol.* **8**, 587 (2013).
- [11] C. O. Avci, K. Garello, M. Gabureac, A. Ghosh, A. Fuhrer, S. F. Alvarado, and P. Gambardella, *Phys. Rev. B* **90**, 224427 (2014).

- [12] R. Osgood III, S. Bader, B. Clemens, R. White, and H. Matsuyama, *J. Magn. Magn. Mater.* **182**, 297 (1998).
- [13] X. Fan, A. R. Mellnik, W. Wang, N. Reynolds, T. Wang, H. Celik, V. O. Lorenz, D. C. Ralph, and J. Q. Xiao, *Appl. Phys. Lett.* **109**, 122406 (2016).
- [14] T. P. Ginley and S. Law, *J. Vac. Sci. Technol. B* **34**, 02L105 (2016).
- [15] J. M. Marmolejo-Tejada, K. Dolui, P. Lazić, P.-H. Chang, S. Smidstrup, D. Stradi, K. Stokbro, and B. K. Nikolić, *Nano Lett.* **17**, 5626 (2017).

Chapter 5

SPIN ORBIT EFFECT WITH SPIN ROTATION IN FERROMAGNETIC MATERIALS

5.1 Introduction

5.1.1 Motivation

As discussed in previous chapters, in-plane charge current in NM/FM bilayers generates the spin orbit torques (SOTs) via the spin Hall effect (SHE) in the NM [1], or the Rashba-Edelstein effect (REE) due to the interfacial spin orbit coupling (SOC) [2-4]. The effect from the topological surface states (TSS) can be viewed as substantially enhanced version of the REE [5]. The SHE will convert a charge current \mathbf{j}_c into a transverse perpendicular spin current \mathbf{Q}_σ with transverse in-plane spin polarization σ . These three vectors are orthogonal to each other in the form:

$$\mathbf{Q}_\sigma = \frac{\hbar}{2e} \theta (\mathbf{j}_c \times \sigma) \quad (5.1)$$

where \hbar is the reduced Planck's constant, e is the electron charge, \mathbf{Q}_σ is the spin current density, \mathbf{j}_c is the charge current density, and θ represents the efficiency of the charge to spin conversion, or so-called spin Hall angle. Based on the symmetry of spin current described by Equation 5.1, the in-plane spin polarization is unable to switch a perpendicular magnetized film (We will discuss the details in the next section). The REE induced spin polarization is along the same y-axis but may be opposite to that from SHE. For the sake of discussion, we assume the spin polarization from both effects are all along y-axis as shown in Figure 5.1.

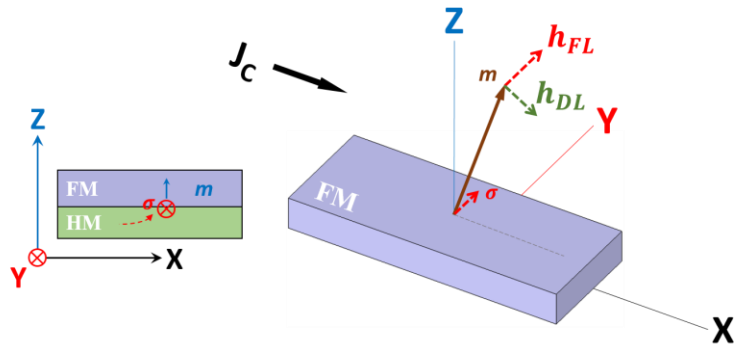


Figure 5.1 The schematic illustration of the SOTs assisted magnetization switching in FM/NM bilayer structure.

In order to switch the magnetization, additional sources to break the symmetry are required which include, for instance, the intrinsic gradient of magnetic anisotropy [6], extra bias magnetic field to tilt the magnetization away from the film normal [7-8], or an effective exchange bias field [9-10]. Even though, the efficiency of such a switching process is still not optimum, since the SOTs must overcome the torque due to anisotropy as well as the intrinsic damping.

A spin current with an out-of-plane spin polarization that is opposite to the perpendicular magnetization is most efficient to switching the magnetization without the need to tilt the magnetization. This has already been realized in the conventional STT-MRAM devices where current is perpendicular to film plane. The spin transfer torque (STT) assisted anti-damping switching process will be discussed in the next section. Devices utilize SOTs so far cannot generate perpendicular spin polarization unless the symmetry in the sample is broken. Recently, MacNeil *et al.* have reported that spin current with perpendicular spin polarization can be generated by a WTe₂/Py bilayer structure due to structural asymmetry in WTe₂ transition metal

dichalcogenide [11]. Other theoretical studies show that this kind of out-of-plane polarized spin current could also be generated via combination of the anomalous Hall effect (AHE) in a FM with tilted magnetization and the spin-filtering effect [12]. Amin and Stiles have predicted the spin-orbit scattering of an in-plane charge current at a FM/NM interface could give rise to a spin current with an arbitrary spin polarization, which is due to the interaction between spins and the magnetic order at the interface [13].

5.1.2 Our Hypothesis to Control Spin Polarization Direction

One possible microscopic mechanism consistent with the prediction from Amin and Stiles is the case where spin polarization of a spin current generated near the FM/NM interface precesses about the magnetization. Although transverse spins rapidly dephase in a FM [14-15], this is not necessarily the case at the FM/NM interface or when FM is very thin. Therefore, from a purely phenomenological point of view, we might expect a source of spin current described by

$$\mathbf{Q}_\sigma^R = \frac{\hbar}{2e} \theta^R \mathbf{j}_c \times (\mathbf{m} \times \boldsymbol{\sigma}) \quad (5.2)$$

where θ^R is the charge to spin conversion efficiency for the spin orbit effect (SOE) with the rotated spin symmetry. In this sense, the generation of a spin current described by Equation 5.2 is loosely analogous to the rotation of the polarization of light by the Faraday effect.

As shown in Figure 5.2 (a), when an in-plane charge current passes through a FM/NM interface, an out-of-plane propagating spin current can be generated with two components in accordance with both Equation 5.1 and 5.2. It should be emphasized that Equation 5.2 describes an effect that is inherently different from the spin filtering

proposed by Taniguchi *et al* [12]. The polarization of the spin current generated via spin filtering is always polarized collinear with the magnetization, whereas the spin current due to spin rotation is always polarized orthogonal to the magnetization.

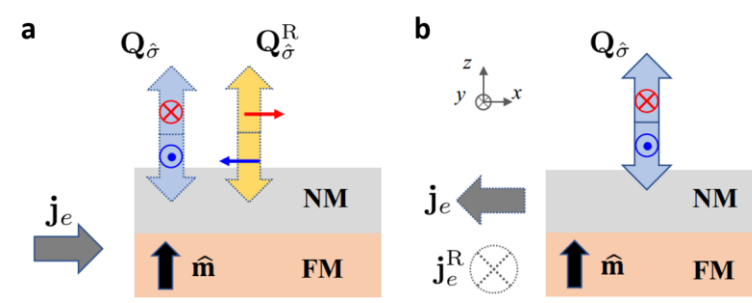


Figure 5.2 The illustration of spin orbit effects with (a) conventional and (b) rotation symmetry. Spin current generated from a charge current near the FM/NM interface. The red and blue arrows represent spins. The vertical blue wide arrows represent the spin current with conventional symmetry and spin rotation symmetry, respectively.

Similarly, as illustrated in Figure 5.2 (b), a spin current \mathbf{Q}_σ that flows out-of-plane in a FM/NM bilayer can generate two in-plane charge currents vis the spin galvanic effect (SGE), one with \mathbf{j}_c in the direction of $\mathbf{Q}_\sigma \times \boldsymbol{\sigma}$, and one with \mathbf{j}_c^R in the rotated direction $-\mathbf{Q}_\sigma \times (\mathbf{m} \times \boldsymbol{\sigma})$. This process could be mathematically described as

$$\mathbf{j}_c = \frac{2e}{\hbar} \theta \times \boldsymbol{\sigma} \quad (5.3)$$

$$\mathbf{j}_\sigma^R = -\frac{2e}{\hbar} \theta^R \mathbf{Q}_\sigma \times (\mathbf{m} \times \boldsymbol{\sigma}) \quad (5.4)$$

where the negative sign in Equation 5.4 is necessary to satisfy the Onsager relation as discussed in our recent work [16].

5.1.3 Magnetization Anti-damping Switching

We now discuss magnetization switching driven by SOTs, which include both the damping-like torque $\boldsymbol{\tau}_{\text{DL}}$ and the field-like torque $\boldsymbol{\tau}_{\text{FL}}$, is described by the Landau-Lifshitz-Gilber-Slonczewski equation [17]:

$$\frac{d\mathbf{m}}{dt} = -\gamma\mathbf{m} \times \mathbf{H}_{\text{eff}} + \alpha\mathbf{m} \times \frac{d\mathbf{m}}{dt} + \gamma h_{\text{DL}}\mathbf{m} \times (\boldsymbol{\sigma} \times \mathbf{m}) - \gamma h_{\text{FL}}\mathbf{m} \times \boldsymbol{\sigma} \quad (5.5)$$

where \mathbf{m} indicates the unit vector of magnetization \mathbf{M} , γ is the gyromagnetic ratio, α is the damping constant, $\boldsymbol{\sigma}$ is the spin polarization, $\boldsymbol{\tau}_{\text{DL}} = \gamma h_{\text{DL}}\mathbf{m} \times (\boldsymbol{\sigma} \times \mathbf{m})$ and $\boldsymbol{\tau}_{\text{FL}} = \gamma h_{\text{FL}}\boldsymbol{\sigma} \times \mathbf{m}$, h_{DL} and h_{FL} are the effective field of damping-like torque and field-like torque, respectively. \mathbf{H}_{eff} includes the perpendicular anisotropy field $\mathbf{H}_{\text{K}} = H_{\text{K}}(\mathbf{m} \cdot \mathbf{z})\mathbf{z}$ and in-plane bias field \mathbf{H}_{bias} , and \mathbf{z} is the film normal.

As shown in Figure 5.1, the charge current \mathbf{j}_{c} is along x direction, the spin current \mathbf{Q}_{σ} generated by the SHE flows through the FM/NM interface with the spin polarization $\boldsymbol{\sigma}$ along y direction. Then replacing $\boldsymbol{\sigma}$ with \mathbf{y} and iterating Equation 5.5, one finds

$$\begin{aligned} \frac{d\mathbf{m}}{dt} = & -\frac{\gamma}{1+\alpha^2}\mathbf{m} \times (\mathbf{H}_{\text{K}}(\mathbf{m} \cdot \mathbf{z})\mathbf{z} - (\alpha h_{\text{DL}} - h_{\text{FL}})\mathbf{y} + \mathbf{H}_{\text{bias}}) \\ & -\frac{\gamma}{1+\alpha^2}\mathbf{m} \times (\mathbf{m} \times (\alpha H_{\text{K}}(\mathbf{m} \cdot \mathbf{z})\mathbf{z} + (h_{\text{DL}} + \alpha h_{\text{FL}})\mathbf{y})) \end{aligned} \quad (5.6)$$

The damping term $\alpha H_{\text{K}}(\mathbf{m} \cdot \mathbf{z})\mathbf{z} + (h_{\text{DL}} + \alpha h_{\text{FL}})\mathbf{y}$ cannot be canceled at any current amplitude. This is the reason why it is impossible to switch a perpendicular magnetized film via so called anti-damping switching. In practice, an extra external field \mathbf{H}_{bias} is introduced to break the symmetry in order to switch the magnetization [6].

If we assume the existence of out-of-plane spin polarization induced by the spin rotation symmetry, and $\boldsymbol{\sigma}$ is along z axis, we can rearrange Equation 5.5

$$\begin{aligned} \frac{d\mathbf{m}}{dt} = & -\frac{\gamma}{1+\alpha^2} (\mathbf{H}_K(\mathbf{m} \cdot \mathbf{z}) - (\alpha h_{DL} - h_{FL})) \mathbf{m} \times \mathbf{z} \\ & - \frac{\gamma}{1+\alpha^2} (\alpha \mathbf{H}_K(\mathbf{m} \cdot \mathbf{z}) + (h_{DL} + \alpha h_{FL})) \mathbf{m} \times (\mathbf{m} \times \mathbf{z}) \end{aligned} \quad (5.7)$$

The first term on the right hand side of Equation 5.7 indicates the precession motion of the magnetization around the film plane normal z . The second term is the damping term and the effective field is $(\alpha \mathbf{H}_K(\mathbf{m} \cdot \mathbf{z}) + (h_{DL} + \alpha h_{FL}))$. The SOTs induced by the rotation symmetry can completely overcome the anisotropy field when the spin current exceeds a threshold satisfying $\alpha \mathbf{H}_K(\mathbf{m} \cdot \mathbf{z}) + (h_{DL} + \alpha h_{FL}) < 0$ with \mathbf{m} along z axis. In this case, anti-damping switching could be realized.

Therefore, if our hypothesis of spin rotation symmetry can be confirmed experimentally, namely, the spin polarization induced at the FM/NM interface is able to precess around \mathbf{m} , one can realize anti-damping switching. Further we postulate that such a rotation can be achieved in a FM. In another word, when a current is flowing through a FM, one would generate transverse spin current since FM has sizable SOC leading to SHE, just like the case for a heavy metal. The transverse spin polarization will be rotated by the magnetization in FM. If the spin dephasing does not fully suppress this spin rotation, the spin current with rotational spin polarization will flow into neighboring FM and create SOTs. Following this hypothesis, we confirm this spin rotation using FM₁/NM/FM₂ structure. FM₁ is the spin current source layer and FM₂ is the detection layer. The purpose of NM spacer layer to avoid direct coupling between FM₁ and FM₂ which tends to align the magnetizations in both FM layers.

5.1.4 Mirror Symmetry Based Analysis

As we mentioned above that the current-driven spin current can only have in-plane spin polarization. This can be easily seen from the symmetry. The symmetry

arguments also provide a tool for designing magnetic material structure to realize particular switching characteristics [6].

Figure 5.3 schematically illustrates how the mirror symmetry breaking in FM can give rise to the out-of-plane spin polarization along z axis. In Figure 5.3 (a), we are mainly focusing on the spin current flow \mathbf{Q}_σ ($+z$ direction) induced near the top surface of NM. The FM layer on top of the NM is not shown here. We assume there is spin polarization σ which is along $+z$ direction. Both the charge current \mathbf{j}_c and the spin current flow \mathbf{Q}_σ are polar vectors, but the spin polarization σ is a pseudovector [18]. Therefore, σ' , the mirror image of σ , is along the $-z$ direction, and the mirror image of \mathbf{j}_c is still aligned the x -direction. This violates the mirror symmetry of the sample. Therefore, the perpendicular spin polarization is not allowed. In Figure 5.3 (b), the top two layers of FM/NM are not shown. The pseudovector magnetization \mathbf{m} is defined along $-x$ direction. Take the mirror transition, the mirror images of σ and \mathbf{m} reverse their directions, σ' is along $-z$ direction, \mathbf{m}' is along $+x$ direction. Both the origin and the mirror images satisfy the relation in Equation 5.2. Thus, this spin rotation symmetry hypothesis is at least allowed under the mirror symmetry analysis. The FM layer plays a role to break the mirror symmetry about the x - z plane [19].

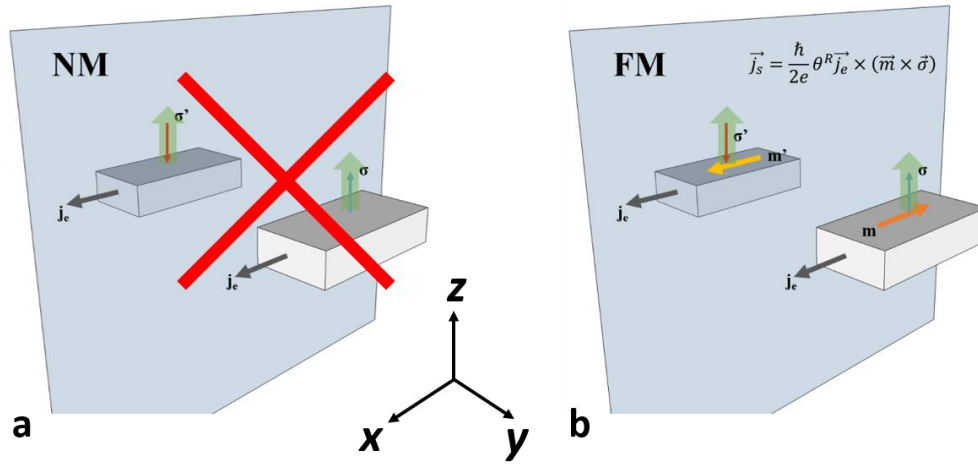


Figure 5.3 The schematics of mirror symmetry and SOEs induced spin polarizations. (a) The spin polarization induced by the conventional SHE in bulk NM layer or near the NM surface. The gray arrow indicates the charge current which is along x direction. The light green wide arrow represents the spin current flow direction, here we focus on the spin current flow on the top surface. The out-of-plane spin polarization couldn't exist in the NM, since it is unable to be uniquely determined by the charge current. (b) The spin rotation symmetry induced out-of-plane spin polarization could satisfy the relation described by Equation 5.2.

5.2 Experiment

In this study, we present the observations of spin current with spin rotation symmetry as described in Equation 5.2 and 5.4. In this section, we show experimental results that confirm our hypothesis of spin current with spin rotation symmetry by using current-induced SOTs and spin Seebeck effect (SSE) driven SGE measurements.

5.2.1 Sample Preparation

All samples were fabricated by magnetron sputtering. The test sample is a multilayer with the structure of seed layer/PML/Cu(3 nm)/Py(2 nm)/Pt(3 nm), and the control sample has the structure of seed layer/PML/Cu(3 nm)/TaO_x(3 nm)/Py(2

nm)/Pt(3 nm), where the seed layer is Ta(2 nm)/Cu(3 nm), PML represents $[\text{Co}_{90}\text{Fe}_{10}(0.16 \text{ nm})/\text{Ni}(0.6 \text{ nm})]_8/\text{Co}_{90}\text{Fe}_{10}(0.16 \text{ nm})$ which has perpendicular magnetization, Py has the concentration of $\text{Ni}_{80}\text{Fe}_{20}$. The TaO_x layers are made by depositing 1.5nm Ta film and subsequently exposing to the air. This process is repeated to fabricate a total of 3 nm of TaO_x . In the SOT experiments, the Py layer is the spin-current detector. The TaO_x insulating layer in the control sample blocks the flow of spin current between the PML and Py layers.

5.2.2 Electrical and Magnetic Properties

The sheet resistance of the test sample is about 8.8Ω and the conductivity of the PML is about $7.1 \times 10^6 \Omega^{-1}\text{m}^{-1}$. The magnetic hysteresis loops of the test sample and control sample were measured by using vibrating sampling magnetometry (VSM), as shown in Figure 5.4. For the out-of-plane measurement configuration (Figure 5.4 (a)), the sharp switching at lower fields corresponds to the PML magnetization while the slope that saturates gradually at higher fields correspond to the Py magnetization. In both test and control samples, the coercivity of PML are identical but the saturation fields of Py are not the same. The saturation field of Py in the control sample is much lower than that in the test sample, which may be due to the increased perpendicular anisotropy at the TaO_x/Py interface compared to that at the Cu/Py interface. In the in-plane measurement configuration, as shown in Figure 5.4 (b), the two hysteresis signals nearly overlap each other. Due to the thick and insulating spacer layers ($\text{Cu}(3 \text{ nm})/\text{TaO}_x(3 \text{ nm})$) in the control sample, the interlayer coupling in the control sample should be negligible. Since the PML magnetization hysteresis in the test sample behaves very closely to that in the control sample, we think the interlayer coupling in the test sample is not significant either.

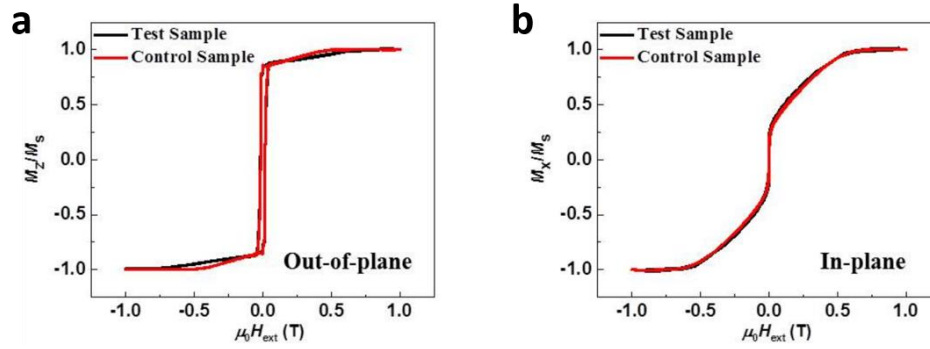


Figure 5.4 Magnetic hysteresis loops measured by VSM. (a) Hysteresis loops measured for the test sample and control sample in the out of plane direction and (b) the in-plane direction.

We further performed ferromagnetic resonance measurements, from which we determined the effective out-of-plane demagnetizing field of Py to be $\mu_0 M_{\text{eff}} = 0.74$ T and the effective out-of-plane anisotropy field of the PML to be $\mu_0 H_{\text{an}\perp} = 0.39$ T. These values are consistent with the magnetic hysteresis measurement. In our measurements, the largest in-plane field applied is 40 mT, which tilts the PML magnetization by approximately 6° .

5.2.3 Spin Orbit Torque Measurement

The measurement geometry is shown in Figure 5.5. The sample is patterned into a $50 \mu\text{m} \times 50 \mu\text{m}$ strip and connected by large gold contact pads. The sample is then placed onto a motion stage, which allows easy focusing and laser scanning over the sample. A laser is incident perpendicularly onto the sample through a $\times 20$ objective. In this measurement, an external field is swept along the x direction. The angle ϕ represents the angle between the current \mathbf{I} (or \mathbf{j}_c) and the external magnetic field \mathbf{H}_{ex} .

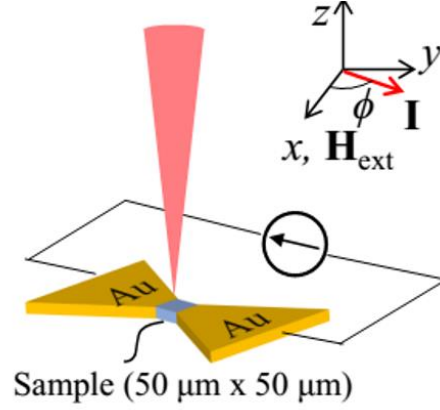


Figure 5.5 The experimental configuration for the SOTs measurement by MOKE magnetometry.

We manually rotated the sample together with the applied current in the film plane. The out-of-plane and in-plane magnetization rotation in Py due to current-induced torques were measured by the polar magneto-optic-Kerr-effect (MOKE) and quadratic MOKE magnetometry, in which the incident light has a linear polarization of 45° and 0° from the x direction, respectively.

According to Equation 5.2, an in-plane charge current \mathbf{j}_c generates spin currents with three components that exert torques on the Py magnetization, \mathbf{Q}_σ with σ along $\mathbf{j}_c \times \mathbf{z}$ due to the SOE with conventional symmetry near the Pt/Py and PML/Cu interfaces, \mathbf{Q}_σ^R with σ along $\mathbf{m}_{\text{PML}} \times (\mathbf{j}_c \times \mathbf{z})$ due to the SOE with spin rotation symmetry near the PML/Cu interface, and \mathbf{q}_σ^R with σ along $\mathbf{m}_{\text{Py}} \times (\mathbf{j}_c \times \mathbf{z})$ due to the SOE with spin rotation symmetry near the Cu/Py and Py/Pt interfaces. In general, a spin current with spin polarization σ can exert two types of SOTs on the Py magnetization \mathbf{m}_{Py} : a damping-like torque $\boldsymbol{\tau}_{\text{DL}}$ in the direction of $(\mathbf{m}_{\text{Py}} \times \sigma) \times \mathbf{m}_{\text{Py}}$, which has an equivalent field in the direction of $\mathbf{m}_{\text{Py}} \times \sigma$, and a field-like torque $\boldsymbol{\tau}_{\text{FL}}$ in the direction of $\sigma \times \mathbf{m}_{\text{Py}}$, which is equivalent to an effect field in the direction of σ .

Therefore, there are four effective fields due to the various SOEs that act on the Py magnetization: (1) $h_{\text{DL}} \cdot \mathbf{m}_{\text{Py}} \times (\mathbf{j}_{\text{c}} \times \mathbf{z})$ due to the $\boldsymbol{\tau}_{\text{DL}}$ from \mathbf{Q}_{σ} and the $\boldsymbol{\tau}_{\text{FL}}$ from $\mathbf{q}_{\sigma}^{\text{R}}$; (2) $h_{\text{FL}} \cdot (\mathbf{j}_{\text{c}} \times \mathbf{z})$ due to the $\boldsymbol{\tau}_{\text{FL}}$ from \mathbf{Q}_{σ} and the $\boldsymbol{\tau}_{\text{DL}}$ from $\mathbf{q}_{\sigma}^{\text{R}}$; (3) $h_{\text{DL}}^{\text{R}} \cdot \mathbf{m}_{\text{Py}} \times [\mathbf{m}_{\text{Py}} \times (\mathbf{j}_{\text{c}} \times \mathbf{z})]$ and $h_{\text{FL}}^{\text{R}} \cdot \mathbf{m}_{\text{Py}} \times (\mathbf{j}_{\text{c}} \times \mathbf{z})$ due to the $\boldsymbol{\tau}_{\text{DL}}$ and $\boldsymbol{\tau}_{\text{FL}}$ from $\mathbf{Q}_{\sigma}^{\text{R}}$, respectively.

It should be emphasized the possible effective fields due to the Rashba-Edelstein SOTs at the Cu/Py and Pt/Py interfaces will share the same symmetry, thus not discussed separately.

5.2.3.1 Damping-Like Torque Measurement

In the limit where the current-induced SOT is small relative to the torque due to the applied field and the demagnetizing field, the out-of-plane of the Py magnetization reorientation is given by

$$\mathbf{m}_{\text{Py}}^{\perp} = \frac{h_{\text{DL}}[\mathbf{m}_{\text{Py}} \times (\mathbf{j}_{\text{c}} \times \mathbf{z})] \cdot \mathbf{z} + h_{\text{DL}}^{\text{R}}[\mathbf{m}_{\text{Py}} \times (\mathbf{m}_{\text{PML}} \times (\mathbf{j}_{\text{c}} \times \mathbf{z}))] \cdot \mathbf{z} + h_{\text{Oe}}^{\perp}}{|\mathbf{H}_{\text{ex}}| + \mathbf{M}_{\text{eff}}} \quad (5.8)$$

where \mathbf{H}_{ex} is the applied external magnetic field, and \mathbf{M}_{eff} is the effective Py demagnetization field along z direction. We detect $\mathbf{m}_{\text{Py}}^{\perp}$ by using the polar MOKE magnetometry, which results in the polarization rotation of Ψ_{polar} of linearly polarized incident light. The three terms in Equation 5.8 can be distinguished by their dependence on \mathbf{m}_{Py} and \mathbf{m}_{PML} .

In the measurement geometry with $\mathbf{j}_{\text{c}} \parallel \mathbf{m}_{\text{Py}}$, the second term in Equation 5.8 is zero. As shown in Figure 5.6, signals of in both the test and control samples resemble the Py magnetization hysteresis, which can be understood from the first term in Equation 5.8. The signal is independent of \mathbf{m}_{PML} . In the third term of Equation 5.8, the Oersted field h_{Oe}^{\perp} , is independent \mathbf{m}_{PML} and \mathbf{m}_{Py} and spatially varies transverse to \mathbf{j}_{c} . We use h_{Oe}^{\perp} , calculated by using the Biot-Savart law, to calibrate the magnitude of

h_{DL} and h_{DL}^R , both of which depend on \mathbf{m}_{Py} and are uniform across the sample. This detailed calibration fitting process has already been discussed in Chapter 3. From the calibration, we estimate that h_{DL} is about $120 \pm 12 \text{ Am}^{-1}$ in the test sample, when the current density through Pt is about $1.2 \times 10^{10} \text{ Am}^{-2}$ and that through the PML is about $3.8 \times 10^{10} \text{ Am}^{-2}$.

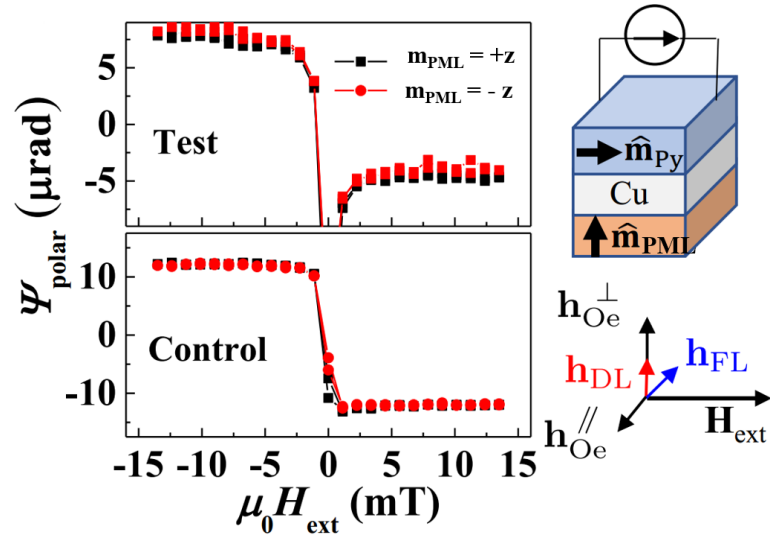


Figure 5.6 The polar MOKE response Ψ_{polar} measured in the test and control samples when current is applied parallel with H_{ex} ($\phi = 0^\circ$). No dependence of \mathbf{m}_{PML} is observed.

In the measurement geometry with $\mathbf{j}_c \perp \mathbf{m}_{Py}$, the first term in Equation 5.8 is zero. As shown in Figure 5.7, Ψ_{polar} for the test sample switches with the applied field direction, and also reverses polarity when \mathbf{m}_{PML} is switched, which is consistent with the behavior expected from the second term of Equation 5.8. The magnitude of h_{DL}^R is estimated to be 25% of the magnitude of h_{DL} , or $30 \pm 4 \text{ Am}^{-1}$. This result confirms the

generation of a spin current with rotated spin polarization by the PML layer. By use of Equation 5.2, we estimate

$$\theta^R = \frac{2e}{\hbar} \frac{|\mathbf{Q}_\sigma^R|}{|\mathbf{j}_c|} = \frac{2e}{\hbar} \frac{\mu_0 M_{\text{Py}} d_{\text{Py}} h_{\text{DL}}^R}{|\mathbf{j}_c|} = (4.8 \pm 0.6) \times 10^{-3} \quad (5.9)$$

Under the assumption of perfect spin absorption at the Py/Cu interface, where $\mu_0 M_{\text{Py}} = 1$ T and $d_{\text{Py}} = 2$ nm are the saturation magnetization and the thickness of Py, respectively. For the control sample, where \mathbf{Q}_σ^R is presumably suppressed by the TaO_x layer, Ψ_{polar} is independent of \mathbf{m}_{PML} . The slight dependence of Ψ_{polar} on the applied field is possible due to the misalignment of the applied field and the current flow direction, which is estimated to be about 1.5°.

We decomposed Ψ_{polar} into the component that is even in $\mathbf{m}(\Delta\Psi_{\text{polar}}^{\text{even}})$ and odd in $\mathbf{m}(\Delta\Psi_{\text{polar}}^{\text{odd}})$, by defining

$$\begin{aligned} \Delta\Psi_{\text{polar}}^{\text{even}} &= (\psi_{\text{polar}}^{++} - \psi_{\text{polar}}^{+-}) + (\psi_{\text{polar}}^{-+} - \psi_{\text{polar}}^{--}) \\ \Delta\Psi_{\text{polar}}^{\text{odd}} &= (\psi_{\text{polar}}^{++} - \psi_{\text{polar}}^{+-}) - (\psi_{\text{polar}}^{-+} - \psi_{\text{polar}}^{--}) \end{aligned} \quad (5.10)$$

where the first superscript in Ψ_{polar}^{++} denotes the sign of \mathbf{m}_{PML} and the second superscript denotes the sign of \mathbf{m}_{Py} during the measurement as illustrated in Figure 5.7. We then measured the dependence of $\Delta\Psi_{\text{polar}}^{\text{even}}$ and $\Delta\Psi_{\text{polar}}^{\text{odd}}$ on the applied field angle in the sample plane.

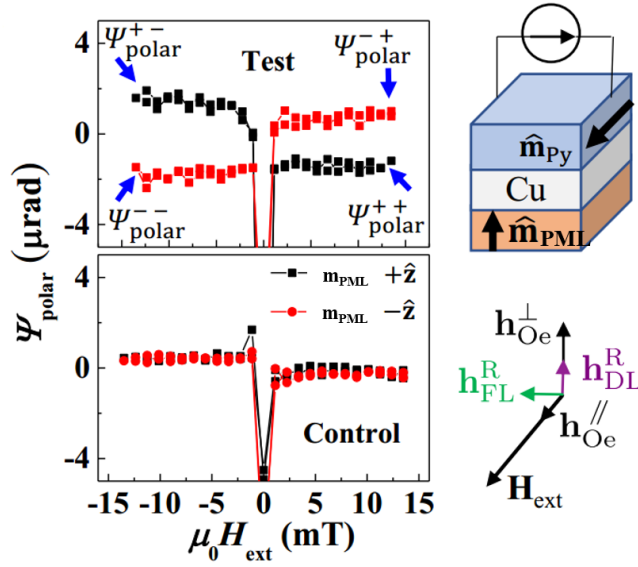


Figure 5.7 The polar MOKE response measured in the test and control samples when current is applied perpendicular to \mathbf{H}_{ex} ($\phi = 90^\circ$). In the test sample, the polar MOKE response is reversed when \mathbf{m}_{PML} is reversed. In the control sample, the polar MOKE response has little dependence on \mathbf{m}_{PML} .

As shown in Figure 5.8, $\Delta\Psi_{\text{polar}}^{\text{even}}$ is proportional to $\cos\phi$, whereas $\Delta\Psi_{\text{polar}}^{\text{odd}}$ is proportional to $\sin\phi$, consistent with the phenomenology expression in Equation 5.8.

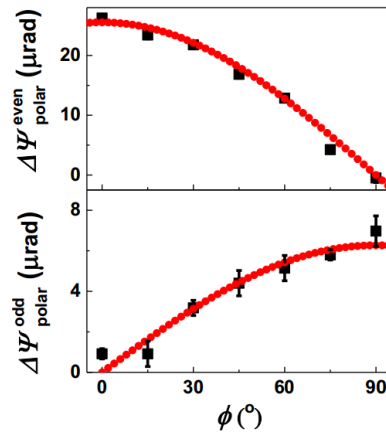


Figure 5.8 The angle dependence of $\Delta\Psi_{\text{polar}}^{\text{even}}$ and $\Delta\Psi_{\text{polar}}^{\text{odd}}$ of the test sample.

5.2.3.2 Field-Like Torque Measurement

As the in-plane current also generates a uniform in-plane Oersted Field h_{Oe}^{\parallel} and the field-like torque terms h_{FL} and h_{FL}^R , the in-plane component of the Py magnetization reorientation is given by

$$m_{Py}^{\parallel} = \frac{h_{FL}(\mathbf{j}_c \cdot \mathbf{x}) + h_{FL}^R[\mathbf{x} \cdot (\mathbf{m}_{PML} \times \mathbf{j}_c)] + h_{Oe}^{\parallel}(\mathbf{j}_c \cdot \mathbf{x})}{|H_{ex}|} \quad (5.11)$$

We measured m_{Py}^{\parallel} using the quadratic MOKE response, and observed the same dependencies on \mathbf{m}_{PML} as for the damping-like torque. The quadratic MOKE response, Ψ_{quad} , is proportional to $(\mathbf{m}_{Py} \cdot \mathbf{y})(\mathbf{m}_{Py} \cdot \mathbf{x})$. When the charge current is parallel to H_{ex} ($\phi = 0^\circ$), as depicted in Figure 5.5 and Figure 5.9 (a), shows that both the test and control samples exhibit quadratic MOKE responses that are proportional to $1/H_{ex}$ but independent of \mathbf{m}_{PML} , as expected from Equation 5.11. When the charge current is applied perpendicular to H_{ex} ($\phi = 90^\circ$), as shown in Figure 5.9 (b), a significant quadratic MOKE signal with a sign dependence on \mathbf{m}_{PML} is obtained with the test sample. This is consistent with the second term in Equation 5.11. On the other hand, the quadratic MOKE signal for the control sample is independent of \mathbf{m}_{PML} , as expected, since \mathbf{Q}_σ^R is blocked by the TaO_x layer. We measured $h_{FL}^R = 41 \pm 13 \text{ Am}^{-1}$ with the test sample, where we employed the same current (30 mA through a 50 μm strip) as was used in the polar MOKE measurement. As such, the field like torque is comparable in magnitude to the damping like torque due to \mathbf{Q}_σ^R .

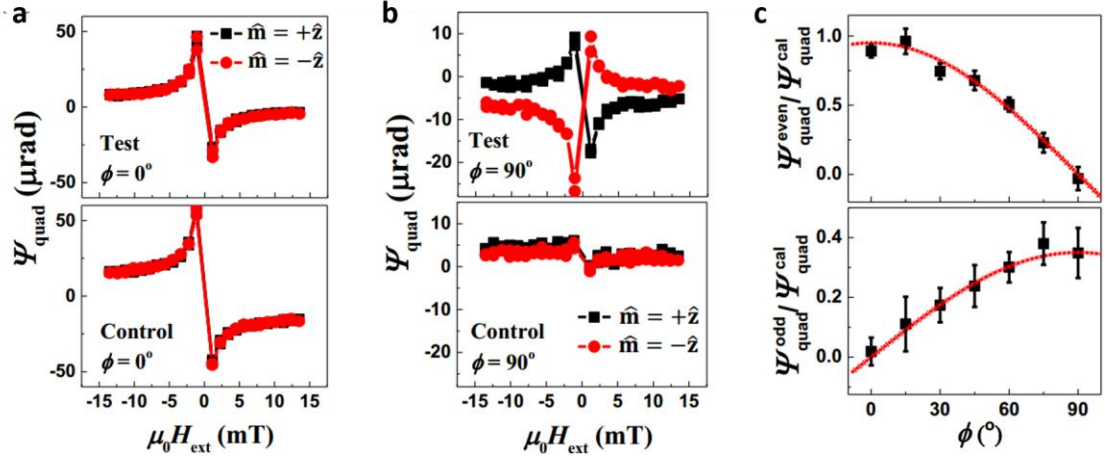


Figure 5.9 The current induced field like torque. Here we use quadratic MOKE magnetometry to measure current induced in-plane effective fields in the same configuration polar MOKE measurement. (a) The quadratic MOKE response measured in the test and control samples when current is applied parallel to H_{ex} . No dependence on \mathbf{m}_{PML} is observed. (b) The quadratic MOKE response measured in the test and control samples when current is applied perpendicular to H_{ex} . In the test sample, the quadratic MOKE response is reversed when \mathbf{m}_{PML} is reversed. In the control sample, the weak quadratic MOKE response is observed, which is likely due to a small misalignment. (c) The angle dependence of $\Psi_{\text{quad}}^{\text{even}}$ and $\Psi_{\text{quad}}^{\text{odd}}$ of the test sample.

We decompose Ψ_{quad} into components that are either even or odd in \mathbf{m}_{PML} by defining

$$\begin{aligned}\Psi_{\text{quad}}^{\text{even}} &= \frac{[\Psi_{\text{quad}}^+ + \Psi_{\text{quad}}^-]}{2} \\ \Psi_{\text{quad}}^{\text{odd}} &= \frac{[\Psi_{\text{quad}}^+ - \Psi_{\text{quad}}^-]}{2}\end{aligned}\quad (5.12)$$

where the superscripts + and – denote whether \mathbf{m}_{PML} is oriented along +z or -z, respectively. We further perform linear fittings of $\Psi_{\text{quad}}^{\text{even}}$ and $\Psi_{\text{quad}}^{\text{odd}}$ with a calibration signal $\Psi_{\text{quad}}^{\text{cal}}$ measured with an external calibration field, and plot the slopes as a function of ϕ in Figure 5.9 (c). As expected from Equation 5.11, $\Psi_{\text{quad}}^{\text{even}}$,

which presumably results from the sum of $h_{\text{Oe}}^{\parallel}$ and h_{FL} , is proportional to $\cos\phi$. While $\Psi_{\text{quad}}^{\text{odd}}$, which is ostensibly the result of h_{FL}^{R} generated by $\mathbf{Q}_{\sigma}^{\text{R}}$, is proportional to $\sin\phi$.

5.2.4 Spin Galvanic Effect Measurement

To further validate our findings, we also measured the spin-rotation symmetry of the SGE, described in Figure 5.2 (b), with a SSE driven SGE measurement of the same samples. As shown in Figure 5.10, when the samples are subjected to an out-of-plane temperature gradient, a spin current is generated due to the SSE [20-21], which then generates an in-plane voltage. The voltage may arise from the anomalous Nernst effect (ANE) in the magnetic layers, the SGE due to the spin currents injected into the adjacent layers, as well as the planar Nernst effect (PNE) [22] in the PML. Depending on whether it has an even or odd symmetry with \mathbf{m}_{PML} , the voltage can be described as

$$\begin{aligned} V^{\text{even}} &= \eta_{\text{Py}}(\nabla T \times \mathbf{m}_{\text{Py}}) \cdot \mathbf{y} + \eta_{\text{PML}}(\nabla T \times \mathbf{m}_{\text{PML}}) \cdot \mathbf{y} \\ V^{\text{odd}} &= \eta_{\text{R}} \nabla T \times (\mathbf{m}_{\text{Py}} \times \mathbf{m}_{\text{PML}}) + \eta_{\text{PML}}^{\text{PNE}}(\mathbf{m}_{\text{PML}} \cdot \mathbf{y})(\mathbf{m}_{\text{PML}} \cdot \nabla T) \end{aligned} \quad (5.13)$$

where ∇T is the temperature gradient in z direction, η_{Py} and η_{PML} with units of V mK^{-1} are the additive ANE and SGE coefficients associated with the Py and PML layers, respectively, $\eta_{\text{PML}}^{\text{PNE}}$ is the coefficient associated with the PNE of the PML, and η_{R} is the coefficient associated to the SGE voltage with spin rotation symmetry described by the second equation of Equation 5.4. Note that η_{R} potentially has two competing sources: the spin current generated in Py that diffuses towards the PML, and the spin current generated in PML that diffused towards the Py.

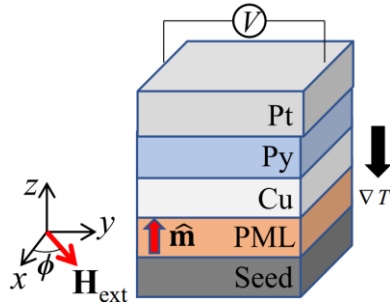


Figure 5.10 The experimental configuration of spin Seebeck effect driven spin galvanic effect measurement.

As shown in Figure 5.11 (a), V^{even} , measured when H_{ex} is along x direction consists of two components: one resembles the hysteretic switching of Py, and a linear slope related to the magnetization tilting of the PML under the influence of external field, as understood from Equation 5.9. When H_{ex} is applied along y direction, V^{even} vanishes. V^{odd} measured for the control sample yields a straight line, which is consistent with the PNE described in Equation 5.13. However, V^{odd} measured for the test sample has an additional component related to the Py magnetization switching, which is consistent with the third term in Equation 5.13 due to the SGE with spin rotation symmetry. Shown in Figure 5.11 (b), the angle dependences of the voltage signal further confirm the symmetry described by Equation 5.13.

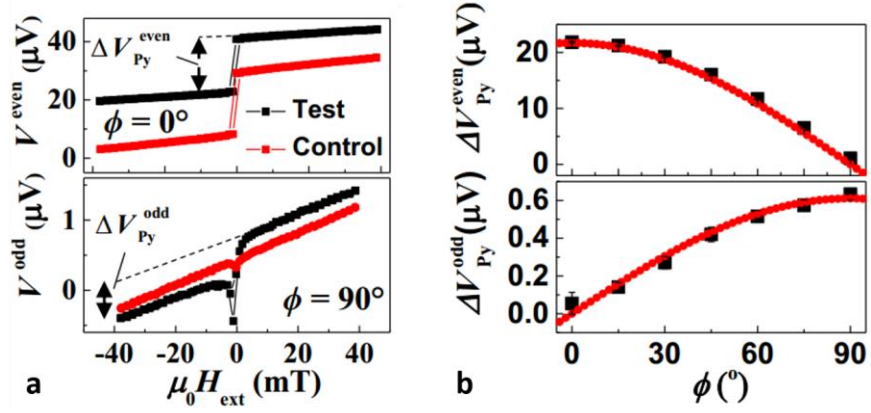


Figure 5.11 The spin Seebeck driven spin galvanic effect measurements. (a) Voltages measured in the two different configurations for the test sample and control sample. (b) Angle dependence of the voltage signals associated with Py switching.

5.3 Discussion

5.3.1 Current in Plane Spin Transfer Torque

The sample used in the spin orbit torque measurement is a spin valve. An in-plane charge current perturbs the electron distribution thus leading to interlayer spin dependent scattering as observed in the giant magnetoresistance effect (GMR) [23]. In this process, the spin dependent scattering may generate a spin transfer torque (STT) on the Py layer that is different from the spin orbit effects. However, this STT is independent of the in-plane current direction. The MOKE response to the charge current due to the STT is likely to be second order and therefore is not picked up in our detection.

5.3.2 Non-local Spin Rotation Process

In the discussion above, we imply the SOT with rotated symmetry originates from $\mathbf{Q}_\sigma^{\text{R}}$ that is generated near the PML/Cu interface. However, $\mathbf{Q}_\sigma^{\text{R}}$ may also be

generated through an alternative process: a spin current is generated from the bulk Py or the Cu/Py and Py/Pt interfaces with conventional symmetry, which diffuses and creates a spin accumulation near the Cu/PML interface. Under the influence of the imaginary part of spin mixing conductance near the Cu/PML interface, this spin accumulation can also generate a spin current with spin-rotation symmetry. In this case, \mathbf{Q}_σ^R is likely to depend on the Py thickness and the capping layer of Py, when Py is thinner than its spin diffusion length. We have measured the damping-like torques with spin rotation symmetry in samples with Ta capping and various Py thicknesses, which are shown in Figure 5.12, but we found \mathbf{Q}_σ^R to be nearly independent of Py thickness (Figure 5.12 (c)) and the capping layer material (Figure 5.12 (d)). Further analysis based on the magnetoelectronic circuit theory [24] also suggests that this process cannot account for the large signal observed experimentally.

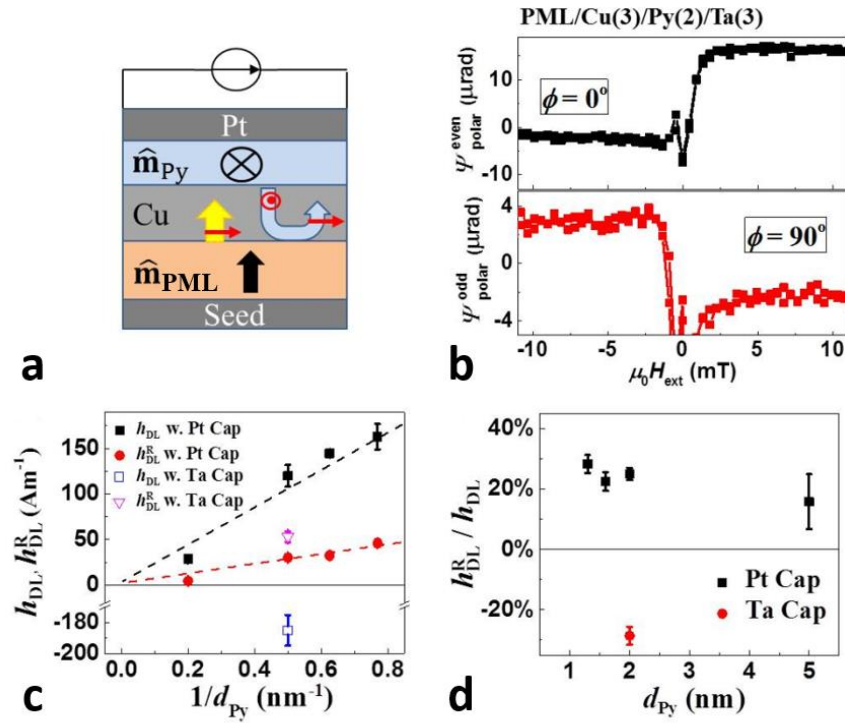


Figure 5.12 The alternative mechanisms for a spin current with rotated polarization. (a) The yellow arrow with the red color spin polarization represents the spin rotation mechanism in this study. The blue “U-turn” arrow with red spin polarization indicates the alternative mechanism that originates from the Pt/Py interface, which could also leads to the sample spin polarization. (b) The polar MOKE measurement of the damping like torque in the sample of PML/Cu(3 nm)/Py(2 nm)/Ta(3 nm). (c) The Py thickness dependent of the damping like torque measurement. (d) The ratio between h_{DL} and h_{DL}^R as a function of Py thickness.

5.3.3 Anomalous Hall Effect induced Spin Rotation Symmetry

The AHE in the PML layer can also generate a new in-plane charge current, which flows perpendicular to the applied charge current. This new charge current can then generate SOT and SGE from the conventional spin orbit effects, and appears to have spin rotation symmetry, as the direction of the new charge current depends on the PML magnetization. However, this contribution should scale with the anomalous Hall

angle of the sample ($\sim 0.02\%$), and is estimated to be much weaker than the observed signal.

5.3.4 Magnetization Tilted by Magnetostatic Coupling

If there is a magnetostatic coupling between the PML and Py layer, the magnetizations of the two will tilt away from the designated directions. In that case, a current induced in-plane effective field with conventional symmetry may cause polar MOKE responses that appear to be from the damping like torque with spin rotation symmetry. However, this effect is estimated to be much weaker than the experimental result.

5.3.5 Other Potential Mechanisms

It should be pointed out that the SOE with spin-rotation symmetry may not only arise from the interface between the very top layer of the PML and Cu. The PML consists of many interfaces of Ni/Co₉₀Fe₁₀, which are known to have a strong spin orbit interaction that gives rise to the perpendicular anisotropy. As each layer in the PML is very thin, the observed SOE may partially arise from the Ni/Co₉₀Fe₁₀ interfaces within the PML.

5.4 Conclusion

The SOE with spin-rotation symmetry can generate spin current with arbitrary polarization simply by adjusting the magnetization direction. An important implication of these findings is the ability to generate a perpendicular polarized spin current by use of a FM/NM interface, where the FM is magnetized collinear to the current flow direction. Such a spin-current polarization is required to switch a perpendicular magnetized layer by use of anti-damping STT alone. These findings can significantly

benefit the development of MRAM technology, where perpendicularly magnetized memory is more favorable as it allows for high stability and scalability [25]. Although the verification of the spin rotation phenomenology presented here does not permit us to predict the efficiency of the perpendicularly polarized spin current generation for the case of collinear current and FM magnetization, we think the key to high efficiency is through interface optimization, where spin orbit interaction, spin precession and dephasing should all be taken into account.

REFERENCES

- [1] L. Liu, C.-F. Pai, Y. Li, H. W. Tseng, D. C. Ralph, and R. A. Buhrman, *Science* **336**, 555 (2012).
- [2] I. M. Miron, G. Gaudin, S. Auffret, B. Rodmacq, A. Schuhl, S. Pizzini, J. Vogel, and P. Gambardella, *Nat. Mater.* **9**, 230 (2010).
- [3] P. M. Haney, H.-W. Lee, K.-J. Lee, A. Manchon, and M. D. Stiles, *Phys. Rev. B* **87**, 174411 (2013).
- [4] S. Emori, T. Nan, A. M. Belkessam, X. Wang, A. D. Matyushov, C. J. Babroski, Y. Gao, H. Lin, and N. X. Sun, *Phys. Rev. B* **93**, 180402 (2016).
- [5] V. M. Edelstein, *Solid State Commun.* **73**, 233 (1990).
- [6] G. Yu, P. Upadhyaya, Y. Fan, J. G. Alzate, W. Jiang, K. L. Wong, S. Takei, S. a Bender, L.-T. Chang, Y. Jiang, M. Lang, J. Tang, Y. Wang, Y. Tserkovnyak, P. K. Amiri, and K. L. Wang, *Nat. Nanotechnol.* **9**, 548 (2014).
- [7] I. M. Miron, K. Garello, G. Gaudin, P.-J. Zermatten, M. V Costache, S. Auffret, S. Bandiera, B. Rodmacq, A. Schuhl, and P. Gambardella, *Nature* **476**, 189 (2011).
- [8] S. Fukami, T. Anekawa, C. Zhang, and H. Ohno, *Nat. Nanotechnol.* **11**, 621 (2016).
- [9] Y. Lau, D. Betto, K. Rode, J. M. D. Coey, and P. Stamenov, *Nat. Nanotechnol.* **11**, 758 (2016).
- [10] S. Fukami, C. Zhang, S. DuttaGupta, A. Kurenkov, and H. Ohno, *Nat. Mater.* **15**, 535 (2016).
- [11] D. MacNeill, G. M. Stiehl, M. H. D. Guimaraes, R. A. Buhrman, J. Park, and D. C. Ralph, *Nat. Phys.* **13**, 300 (2016).
- [12] T. Taniguchi, J. Grollier, and M. D. Stiles, *Phys. Rev. Appl.* **3**, 044001 (2015).
- [13] V. P. Amin and M. D. Stiles, *Phys. Rev. B* **94**, 104419 (2016).

- [14] M. D. Stiles and A. Zangwill, *Phys. Rev. B* **66**, 014407 (2002).
- [15] A. Ghosh, S. Auffret, U. Ebels, and W. E. Bailey, *Phys. Rev. Lett.* **109**, 127202 (2012).
- [16] A. M. Humphries, T. Wang, E. R. J. Edwards, S. R. Allen, J. M. Shaw, H. T. Nembach, J. Q. Xiao, T. J. Silva, and X. Fan, *Nat. Commun.* **8**, 911 (2017).
- [17] X. Fan, H. Celik, J. Wu, C. Ni, K. Lee, V. O. Lorenz, and J. Q. Xiao, *Nat. Commun.* **5**, 1 (2014).
- [18] S. Fulling, M. Sinyakov, and S. Tishchenko, in *Linearity Math. Sev. Var.* (WORLD SCIENTIFIC, 2000), pp. 321–392.
- [19] J. Tang, Q. Shao, P. Upadhyaya, P. K. Amiri, and K. L. Wang, in edited by W. Zhao and G. Prenat (Springer International Publishing, Cham, 2015), pp. 53–112.
- [20] K. Uchida, S. Takahashi, K. Harii, J. Ieda, W. Koshibae, K. Ando, S. Maekawa, and E. Saitoh, *Nature* **455**, 778 (2008).
- [21] Y. Xu, B. Yang, C. Tang, Z. Jiang, M. Schneider, R. Whig, and J. Shi, *Appl. Phys. Lett.* **105**, 242404 (2014).
- [22] A. D. Avery, M. R. Pufall, and B. L. Zink, *Phys. Rev. Lett.* **109**, 196602 (2012).
- [23] R. E. Camley and J. Barnaś, *Phys. Rev. Lett.* **63**, 664 (1989).
- [24] A. Brataas, Y. V Nazarov, and G. E. W. Bauer, *Eur. Phys. J. B* **22**, 99 (2001).
- [25] N. Nishimura, T. Hirai, A. Koganei, T. Ikeda, K. Okano, Y. Sekiguchi, and Y. Osada, *J. Appl. Phys.* **91**, 5246 (2002).

Chapter 6

CONCLUSION AND FUTURE DIRECTION

This thesis summarizes my studies on the spin orbit coupling (SOC) induced phenomenon in three different material systems including *3d* light transition metal vanadium, topologic insulator and ferromagnetic material by probing the spin orbit torques (SOTs) that exert on an adjacent ferromagnetic layer. The SOTs play an important role in the next generation of magnetic random access memory (MRAM) featuring low energy dissipation and non-volatility. Our research objective is to find materials and/or heterostructures with much improved efficiency in SOTs. We found unusually large spin Hall angle in V films with distorted structure. We observed strong SOTs on TI/FM heterostructures arising from spin-momentum locking on topologic surface state (TSS). Moreover, the spin rotation symmetry we discovered in FM allows us to control the spin polarization direction in a spin current which will significantly benefit the MRAM development. Except the fundamental research, we have also meticulously developed shadow mask technique to fabricate two nanoscale devices: spin wave devices based on perpendicular magnetized Ta/CoFeB/MgO structure and magnetoelectric (ME) devices based on voltage-controlled interfacial exchange coupling in Cr₂O₃.

For fast nanoscale device fabrication, we have developed two shadow mask recipes based on PMMA/PMGI and CSAR/LOR bilayer E-beam resist. The former is used for [Co/Pd]_n multi-layer deposition in the ME device, and the latter is used for Ta/CoFeB/MgO/CoFeB/Ta magnetic tunnel junctions (MTJs) preparation in the spin

wave device. For the ME device fabrication, we have successfully prepared $[\text{Co/Pd}]_n$ films with perpendicular magnetic anisotropy (PMA) in the form of nanoscale Hall bar structure on top of the antiferromagnet Cr_2O_3 through the designed PMMA/PMGI shadow mask. The future efforts can be applied to: (1) modify E-beam lithography process to reduce/eliminate the E-beam resists and other chemical residues from sample fabrication, which can deteriorate the interfacial exchange coupling dramatically, and (2) further improve Cr_2O_3 sample quality. The current Cr_2O_3 still has a leakage current issue that is closely related to the sample quality, which are being investigated by our collaborators at the University of Nebraska. For the spin wave device, the shadow mask deposition method has also been demonstrated which is capable to fabricate MgO-based MTJs. The newly developed CSAR/LOR recipe has been proved to achieve the chemical/mechanical stability requirement under magnetron sputtering environment. More tuning of sputtering parameters is needed to attain the optimized thickness for each layer, so as to prepare the MgO based MTJs with PMA feature which is a crucial component in spin wave devices.

The efficient generation of pure current is a key enabling technology to develop future memory and logic devices with low energy consumption. We have found a large charge to spin conversion efficiency in 3d light metal vanadium. The sputtering grown V films have a mixed body centered tetragonal (*bct*) and body centered cubic (*bcc*) structure, and its spin Hall angle is as large as $\theta_V = -0.071 \pm 0.003$, comparable to that of the 5d heavy metal Pt. Our finding indicates that specific crystalline structure can lead to a large SHE and 3d light metals should not be ruled out in the search for materials with large spin Hall angle.

In addition to conventional NMs such as Pt, Ta, W *et al.*, topological insulator becomes a promising candidate as a highly efficient source to generate spin current due to its topologically protected surface/edge state. On the topological interface, the backscattering is forbidden by the surface band structure which induces the spin-momentum locking feature. We have investigated the temperature dependent SOTs in Bi₂Se₃/Co heterostructure by second harmonic SOTs measurement technique. As the temperature decreases, the effective fields of the field-like torque and damping-like torque decrease down to 50K, followed by a rapid increase at lower temperature region. The detailed analysis indicates that the origin of the observed SOTs is due to the topological surface state at the interface of Bi₂Se₃/Co. In comparison, the bulk SHE dominates the generation of SOTs in Bi₂Se₃/Ni₈₀Fe₂₀, leading to the observation of both the field-like and damping-like torques decrease monotonously with decreasing temperature. For the future direction, one should vary the thickness of Co layer down to a few atomic layer in Bi₂Se₃/Co system to probe how interfacial electronic structures and spin textures affect the SOTs. One should also find method to characterize the interfacial electronic structures and spin textures affect. Furthermore, there will be many interesting TSS involving phenomenon to study in magnetic insulator/topological insulator systems, for example, the perpendicular magnetized TmIG/Bi₂Se₃. It will be much more convenient to realize the voltage controlled Fermi level tuning in this structure. Finally, there will be a potential magnetic proximity effect at the TmIG/Bi₂Se₃ interface which may induce relevant quantum state effects that have already been attracting great attentions in spintronics community these days.

The strength of SOTs induced by topological insulator is greater than any other materials so far, which will boost the development of spintronics applications. On the

other hand, we have discovered that the efficiency of SOTs assisted magnetic switching can be further improved by creating spin current with spin polarization perpendicular to film plane. We demonstrated the control of spin polarization direction in a spin current by introducing symmetry breaking by using FM layer instead of NM layer as the spin current source. The use of FM breaks the mirror symmetry, permitting spin current with spin polarization perpendicular to film plane. Such a spin current leads to highly efficient anti-damping switching in a neighboring FM layer. We proved the spin rotation symmetry by measuring SOTs and magnetothermal effect in $[\text{CoFe/Ni}]_n/\text{Cu}/\text{Ni}_{80}\text{Fe}_{20}$ spin valve structure. For future work one can focus on the spin rotation symmetry at magnetic insulator/FM bilayers in which magnetic insulator and FM have a perpendicular and parallel magnetization, respectively. The spin current in FM will rotate around the in-plane magnetization, leading to spin current with perpendicular spin polarization. Such a spin current can switch the perpendicular magnetization in magnetic insulator.

Appendix A

REPRINT PERMISSIONS

Reprint Permissions for Figures 1.3, 1.4 and 4.3.

**NATURE PUBLISHING GROUP LICENSE
TERMS AND CONDITIONS**

Nov 07, 2017

This Agreement between Mr. Tao Wang ("You") and Nature Publishing Group ("Nature Publishing Group") consists of your license details and the terms and conditions provided by Nature Publishing Group and Copyright Clearance Center.

License Number	4223960206469
License date	Nov 07, 2017
Licensed Content Publisher	Nature Publishing Group
Licensed Content Publication	Nature Materials
Licensed Content Title	Robust isothermal electric control of exchange bias at room temperature
Licensed Content Author	Xi He, Yi Wang, Ning Wu, Anthony N. Caruso, Elio Vescovo, Kirill D. Belashchenko
Licensed Content Date	Jun 20, 2010
Licensed Content Volume	9
Licensed Content Issue	7
Type of Use	reuse in a dissertation / thesis
Requestor type	academic/educational
Format	print and electronic
Portion	figures/tables/illustrations
Number of figures/tables/illustrations	1
High-res required	no
Figures	Figure 1
Author of this NPG article	no
Your reference number	
Title of your thesis / dissertation	SPIN ORBIT COUPLING INDUCED PHENOMENA IN SPINTRONIC DEVICES
Expected completion date	Dec 2017
Estimated size (number of pages)	155
Requestor Location	Mr. Tao Wang 104 the Green RM217 NEWARK, DE 19716 United States Attn: Mr. Tao Wang
Billing Type	Invoice
Billing Address	Mr. Tao Wang 104 the Green RM217 NEWARK, DE 19716

United States
Attn: Mr. Tao Wang

Total 0.00 USD

Terms and Conditions

Terms and Conditions for Permissions

Nature Publishing Group hereby grants you a non-exclusive license to reproduce this material for this purpose, and for no other use, subject to the conditions below:

1. NPG warrants that it has, to the best of its knowledge, the rights to license reuse of this material. However, you should ensure that the material you are requesting is original to Nature Publishing Group and does not carry the copyright of another entity (as credited in the published version). If the credit line on any part of the material you have requested indicates that it was reprinted or adapted by NPG with permission from another source, then you should also seek permission from that source to reuse the material.
2. Permission granted free of charge for material in print is also usually granted for any electronic version of that work, provided that the material is incidental to the work as a whole and that the electronic version is essentially equivalent to, or substitutes for, the print version. Where print permission has been granted for a fee, separate permission must be obtained for any additional, electronic re-use (unless, as in the case of a full paper, this has already been accounted for during your initial request in the calculation of a print run). NB: In all cases, web-based use of full-text articles must be authorized separately through the 'Use on a Web Site' option when requesting permission.
3. Permission granted for a first edition does not apply to second and subsequent editions and for editions in other languages (except for signatories to the STM Permissions Guidelines, or where the first edition permission was granted for free).
4. Nature Publishing Group's permission must be acknowledged next to the figure, table or abstract in print. In electronic form, this acknowledgement must be visible at the same time as the figure/table/abstract, and must be hyperlinked to the journal's homepage.
5. The credit line should read:
Reprinted by permission from Macmillan Publishers Ltd: [JOURNAL NAME] (reference citation), copyright (year of publication)
For AOP papers, the credit line should read:
Reprinted by permission from Macmillan Publishers Ltd: [JOURNAL NAME], advance online publication, day month year (doi: 10.1038/sj.[JOURNAL ACRONYM].XXXXX)

Note: For republication from the *British Journal of Cancer*, the following credit lines apply.

Reprinted by permission from Macmillan Publishers Ltd on behalf of Cancer Research UK: [JOURNAL NAME] (reference citation), copyright (year of publication) For AOP papers, the credit line should read:
Reprinted by permission from Macmillan Publishers Ltd on behalf of Cancer Research UK: [JOURNAL NAME], advance online publication, day month year (doi: 10.1038/sj.[JOURNAL ACRONYM].XXXXX)

6. Adaptations of single figures do not require NPG approval. However, the adaptation should be credited as follows:

Adapted by permission from Macmillan Publishers Ltd: [JOURNAL NAME] (reference citation), copyright (year of publication)

Note: For adaptation from the *British Journal of Cancer*, the following credit line applies.

Adapted by permission from Macmillan Publishers Ltd on behalf of Cancer Research UK: [JOURNAL NAME] (reference citation), copyright (year of publication)

7. Translations of 401 words up to a whole article require NPG approval. Please visit <http://www.macmillanmedicalcommunications.com> for more information. Translations of up

to a 400 words do not require NPG approval. The translation should be credited as follows:

Translated by permission from Macmillan Publishers Ltd: [JOURNAL NAME] (reference citation), copyright (year of publication).

Note: For translation from the *British Journal of Cancer*, the following credit line applies.

Translated by permission from Macmillan Publishers Ltd on behalf of Cancer Research UK: [JOURNAL NAME] (reference citation), copyright (year of publication)

We are certain that all parties will benefit from this agreement and wish you the best in the use of this material. Thank you.

Special Terms:

v1.1

Questions? customercare@copyright.com or +1-855-239-3415 (toll free in the US) or +1-978-646-2777.

**AMERICAN PHYSICAL SOCIETY LICENSE
TERMS AND CONDITIONS**

Nov 07, 2017

This Agreement between Mr. Tao Wang ("You") and American Physical Society ("American Physical Society") consists of your license details and the terms and conditions provided by American Physical Society and Copyright Clearance Center.

License Number	4223961254759
License date	Nov 07, 2017
Licensed Content Publisher	American Physical Society
Licensed Content Publication	Physical Review Letters
Licensed Content Title	Electric Control of Exchange Bias Training
Licensed Content Author	W. Echtenkamp and Ch. Biniek
Licensed Content Date	Oct 31, 2013
Licensed Content Volume	111
Type of Use	Thesis/Dissertation
Requestor type	Student
Format	Print, Electronic
Portion	image/photo
Number of images/photos requested	1
Portion description	Figure 1
Rights for	Main product
Duration of use	Life of Current Edition
Creation of copies for the disabled	no
With minor editing privileges	no
For distribution to	Worldwide
In the following language(s)	Original language of publication
With incidental promotional use	no
The lifetime unit quantity of new product	0 to 499
The requesting person/organization is:	Tao Wang/Univ of Delaware
Order reference number	
Title of your thesis / dissertation	SPIN ORBIT COUPLING INDUCED PHENOMENA IN SPINTRONIC DEVICES
Expected completion date	Dec 2017
Expected size (number of pages)	155
Requestor Location	Mr. Tao Wang 104 the Green RM217

	NEWARK, DE 19716 United States Attn: Mr. Tao Wang
Billing Type	Invoice
Billing Address	Mr. Tao Wang 104 the Green RM217
	NEWARK, DE 19716 United States Attn: Mr. Tao Wang
Total	0.00 USD
Terms and Conditions	

Terms and Conditions

The American Physical Society (APS) is pleased to grant the Requestor of this license a non-exclusive, non-transferable permission, limited to **print** and/or **electronic** format, depending on what they chose], provided all criteria outlined below are followed.

1. You must also obtain permission from at least one of the lead authors for each separate work, if you haven't done so already. The author's name and affiliation can be found on the first page of the published Article.
2. For electronic format permissions, Requestor agrees to provide a hyperlink from the reprinted APS material using the source material's DOI on the web page where the work appears. The hyperlink should use the standard DOI resolution URL, <http://dx.doi.org/{DOI}>. The hyperlink may be embedded in the copyright credit line.
3. For print format permissions, Requestor agrees to print the required copyright credit line on the first page where the material appears: "Reprinted (abstract/excerpt/figure) with permission from [(FULL REFERENCE CITATION) as follows: Author's Names, APS Journal Title, Volume Number, Page Number and Year of Publication.] Copyright (YEAR) by the American Physical Society."
4. Permission granted in this license is for a one-time use and does not include permission for any future editions, updates, databases, formats or other matters. Permission must be sought for any additional use.
5. Use of the material does not and must not imply any endorsement by APS.
6. Under no circumstance does APS purport or intend to grant permission to reuse materials to which it does not hold copyright. It is the requestors sole responsibility to ensure the licensed material is original to APS and does not contain the copyright of another entity, and that the copyright notice of the figure, photograph, cover or table does not indicate that it was reprinted by APS, with permission from another source.
7. The permission granted herein is personal to the Requestor for the use specified and is not transferable or assignable without express written permission of APS. This license may not be amended except in writing by APS.
8. You may not alter, edit or modify the material in any manner.
9. You may translate the materials only when translation rights have been granted.
10. You may not use the material for promotional, sales, advertising or marketing purposes.
11. The foregoing license shall not take effect unless and until APS or its agent, Copyright Clearance Center (CCC), receives payment in full in accordance with CCC Billing and Payment Terms and Conditions, which are incorporated herein by reference.
12. Should the terms of this license be violated at any time, APS or CCC may revoke the license with no refund to you and seek relief to the fullest extent of the laws of the USA. Official written notice will be made using the contact information provided with the permission request. Failure to receive such notice will not nullify revocation of the permission.

13. APS reserves all rights not specifically granted herein.

14. This document, including the CCC Billing and Payment Terms and Conditions, shall be the entire agreement between the parties relating to the subject matter hereof.

Other Terms and Conditions

Version 1.1

Questions? customer@copyright.com or +1-855-239-3415 (toll free in the US) or +1-978-646-2777.

**NATURE PUBLISHING GROUP LICENSE
TERMS AND CONDITIONS**

Nov 07, 2017

This Agreement between Mr. Tao Wang ("You") and Nature Publishing Group ("Nature Publishing Group") consists of your license details and the terms and conditions provided by Nature Publishing Group and Copyright Clearance Center.

License Number	4224010542869
License date	Nov 07, 2017
Licensed Content Publisher	Nature Publishing Group
Licensed Content Publication	Nature Communications
Licensed Content Title	Quantifying interface and bulk contributions to spin-orbit torque in magnetic bilayers
Licensed Content Author	Xin Fan, Halise Celik, Jun Wu, Chaoying Ni, Kyung-Jin Lee et al.
Licensed Content Date	Jan 9, 2014
Licensed Content Volume	5
Type of Use	reuse in a dissertation / thesis
Requestor type	academic/educational
Format	print and electronic
Portion	figures/tables/illustrations
Number of figures/tables/illustrations	1
High-res required	no
Figures	Figure 2
Author of this NPG article	no
Your reference number	
Title of your thesis / dissertation	SPIN ORBIT COUPLING INDUCED PHENOMENA IN SPINTRONIC DEVICES
Expected completion date	Dec 2017
Estimated size (number of pages)	155
Requestor Location	Mr. Tao Wang 104 the Green RM217 NEWARK, DE 19716 United States Attn: Mr. Tao Wang
Billing Type	Invoice
Billing Address	Mr. Tao Wang 104 the Green RM217 NEWARK, DE 19716 United States Attn: Mr. Tao Wang

Total 0.00 USD

[Terms and Conditions](#)

Terms and Conditions for Permissions

Nature Publishing Group hereby grants you a non-exclusive license to reproduce this material for this purpose, and for no other use, subject to the conditions below:

1. NPG warrants that it has, to the best of its knowledge, the rights to license reuse of this material. However, you should ensure that the material you are requesting is original to Nature Publishing Group and does not carry the copyright of another entity (as credited in the published version). If the credit line on any part of the material you have requested indicates that it was reprinted or adapted by NPG with permission from another source, then you should also seek permission from that source to reuse the material.
2. Permission granted free of charge for material in print is also usually granted for any electronic version of that work, provided that the material is incidental to the work as a whole and that the electronic version is essentially equivalent to, or substitutes for, the print version. Where print permission has been granted for a fee, separate permission must be obtained for any additional, electronic re-use (unless, as in the case of a full paper, this has already been accounted for during your initial request in the calculation of a print run). NB: In all cases, web-based use of full-text articles must be authorized separately through the 'Use on a Web Site' option when requesting permission.
3. Permission granted for a first edition does not apply to second and subsequent editions and for editions in other languages (except for signatories to the STM Permissions Guidelines, or where the first edition permission was granted for free).
4. Nature Publishing Group's permission must be acknowledged next to the figure, table or abstract in print. In electronic form, this acknowledgement must be visible at the same time as the figure/table/abstract, and must be hyperlinked to the journal's homepage.
5. The credit line should read:
Reprinted by permission from Macmillan Publishers Ltd: [JOURNAL NAME] (reference citation), copyright (year of publication)
For AOP papers, the credit line should read:
Reprinted by permission from Macmillan Publishers Ltd: [JOURNAL NAME], advance online publication, day month year (doi: 10.1038/sj.[JOURNAL ACRONYM].XXXXX)

Note: For republication from the *British Journal of Cancer*, the following credit lines apply.

Reprinted by permission from Macmillan Publishers Ltd on behalf of Cancer Research UK: [JOURNAL NAME] (reference citation), copyright (year of publication) For AOP papers, the credit line should read:
Reprinted by permission from Macmillan Publishers Ltd on behalf of Cancer Research UK: [JOURNAL NAME], advance online publication, day month year (doi: 10.1038/sj.[JOURNAL ACRONYM].XXXXX)

6. Adaptations of single figures do not require NPG approval. However, the adaptation should be credited as follows:

Adapted by permission from Macmillan Publishers Ltd: [JOURNAL NAME] (reference citation), copyright (year of publication)

Note: For adaptation from the *British Journal of Cancer*, the following credit line applies.

Adapted by permission from Macmillan Publishers Ltd on behalf of Cancer Research UK: [JOURNAL NAME] (reference citation), copyright (year of publication)

7. Translations of 401 words up to a whole article require NPG approval. Please visit <http://www.macmillanmedicalcommunications.com> for more information. Translations of up to a 400 words do not require NPG approval. The translation should be credited as follows:

Translated by permission from Macmillan Publishers Ltd: [JOURNAL NAME] (reference citation), copyright (year of publication).

Note: For translation from the *British Journal of Cancer*, the following credit line applies.

Translated by permission from Macmillan Publishers Ltd on behalf of Cancer Research UK: [JOURNAL NAME] (reference citation), copyright (year of publication)

We are certain that all parties will benefit from this agreement and wish you the best in the use of this material. Thank you.

Special Terms:

v1.1

Questions? customercare@copyright.com or +1-855-239-3415 (toll free in the US) or +1-978-646-2777.
